Molecular simulations of new ammonium-based ionic liquids as environmentally acceptable lubricant oils

Ana Catarina Fernandes Mendonça

N° d'ordre: D.U. 2341

UNIVERSITE BLAISE PASCAL

U.F.R. Sciences et Technologies

ECOLE DOCTORALE DES SCIENCES FONDAMENTALES

N° 743

THESE

présentée pour obtenir le grade de

DOCTEUR D'UNIVERSITE

(Spécialité : Chimie Physique)

Par **MENDONÇA Ana Catarina**

Master en Chimie

Molecular Simulations of New Ammonium-based Ionic Liquids as Environmentally Acceptable Lubricant Oils

Simulations moléculaires d'une nouvelle classe de liquides ioniques basés sur la fonction ammonium pour l'utilisation potentielle en tant qu'huiles lubrifiantes respectueuses de l'environnement

Soutenue publiquement le 21 Février 2013, devant la commission d'examen:

Président du Jury:	Dominic TILDESLEY (Pr-CECAM)
Rapporteur:	Guillaume GALLIERO (Pr-UPPA)
Rapporteur:	Mathieu SALANNE (M.C.-UPMC)
Directeur:	Agílio PÁDUA (Pr-UBP)
Co-Directeur:	Patrice MALFREYT (Pr-UBP)
Examinateur:	Susan PERKIN (Dr.-U.Oxford)

Acknowledgments

This thesis is the work of three years. Three fast years, for someone that had never seriously touched a computer simulation code or a C program before starting the thesis. And this is it, and I did it. And of course, nothing could have happened without the guidance, teachings, support and intelligent advices of my thesis supervisors, Prof. Agílio Pádua and Prof. Patrice Malfreyt. To them, I would like to express my deep gratitude.

At the beginning everything was new: the work, the country, the city, the lab, the language and the colleagues. These, were crucial in my integration and and I'm very grateful to all of them. In particular to Margarida Costa Gomes, a great woman and scientist that never refused to give me an advice and with whom I will certainly miss to talk.

I would also like to extend my thanks to other colleagues that also became my friends. They are Gaëlle Filippini, Yohann Coulier, Olivia Fandiño, João França, Ajda Podgorsek, Moisés Curras, Alfonso Pensado and Marina Macchiagodena. Between them, my special thanks goes to Gaëlle, the person who shared the office with me during most of the time. Thank you for your patience, I know I can be annoying, specially when I speak by myself or get nervous. You are the best!

Another very important person in all this period is Leila Moura. I was very lucky to have her here with me, she has been my best friend and I hope our friendship lasts forever. You can always count on me to support you when the time comes, just as you have been there to supported me.

I wish to thank Yury Fomin for the work collaboration, and the technical support of: Florent Goujon, his teachings and of course, his marvelous homemade chocolates were very useful; Stefan Eder, for his help with Lammps; Lucia Pisarova and Aline Walter for density, viscosity and surface tension measurements in the chemicals simulated in this work.

I would like to thank the Marie Curie Actions and the MINILUBES project, for the financial support and for the professional and human experiences. The project allowed me to meet great people from different countries and among them I wish to thank Lucia Pisarova, Adina Neacsu, Francesco Pagano, Parvin Zare and Stephanie Steudte. A special thanks goes to Mr. Janotka and Dr. Dörr for the project coordination and management. Thanks to this project and its numerous meetings I was able to visit 12 countries and attend more than 50 flights in the last three years! But besides the social aspect, there is an important professional experience coming out from this European project, in the form of interesting trainings and the participation to four international conferences.

When I left my country (Portugal) I also left a part of my heart with my family. In particular my parents, my brother, my sister-in-law, my nephews, my grand-mothers, my godfathers and my cousins. Thank you for your support and encouragement through all my years of study, including these last three, despite the distance. I will always love you.

I would also like to thank all the friends I left in Portugal. Most of them came to visit me, giving me the strength to continue.

Finally, but not less important, I wish to thank Bruno. I never could have made it without you, without your love and support.

A computer is like a horse, it will sense weakness.

Greg Wettstein

Abstract

The aim of the present work is to understand at the molecular level the structure and interactions of ionic liquids at metallic surfaces, using molecular dynamics simulations, and to investigate the impact that these microscopic features can have in the tribological properties of the system. The chosen ionic liquids as potential lubricant oils present suitable ecotoxic and biodegradable properties and appropriate tribological characteristics. They are based in alkylammonium cations combined with alkylsulfonate and bistriflamide anions. Our study is divided in four parts, starting from the analyses of pure ionic liquids solutions and evolving to systems of ionic liquids confined between surfaces of iron, at the equilibrium, under shear and also in the presence of water.

Structural and dynamic properties of ionic liquids are investigated in terms of the site-site radial distribution functions and the self-diffusion coefficients. The presence of charge-ordering and the formation of micro-domains in solution are discussed, as well as the diffusive behavior of the ionic species.

An atomistic force field for ionic liquids interacting with a metal surface was built based on quantum methods. Density functional calculations of alkylammonium cations, alkylsulfonate and bistriflamide anions interacting with a cluster of iron atoms are performed, at a series of distances and orientations. A site-site potential function was then adjusted to the DFT interactions energies, to obtain the force field parameters. Finally, the polarization of the metal by the ions was taken into account using in-

duced dipoles to reproduce the interaction energy between charges and a conductor surface. Using this interaction model, molecular dynamics simulations were performed to study the structure of the interfacial layer of several ionic liquids at a flat iron surface, including analyses of the positional and orientational ordering of the ions near the surface, and charge density profiles.

Non-equilibrium molecular dynamics simulations of ionic liquids interacting with iron surfaces were carried out using the specific set of interaction parameters developed previously. A procedure was developed for a quantitative prediction of the friction coefficient at different loads and shear rates, based in a definition of pressure measured locally. The dependence of friction on the load, shear velocity, surface topology and length of alkyl side chains in the ionic liquid was investigated. The changes in the frictional forces were explained in terms of the specific arrangements and orientations of groups forming the ionic liquid at the vicinity of the surface.

Finally, the effect of the presence of water in a small quantity in an ionic liquid solution is also studied at equilibrium and non-equilibrium. An interaction potential was build that describes the interaction between water and an iron surface, using the same approach described previously. Preliminary results are presented on the structure at the metal–liquid interface and friction coefficient, and compared with the pure ionic liquids.

Keywords: Ionic liquids, metallic surfaces, interaction model, molecular dynamics simulations, friction, non-equilibrium molecular dynamics, pressure tensor

Résumé

L'objectif de ce travail est de comprendre la structure et les interactions des liquides ioniques au contact de surfaces métalliques à l'échelle moléculaire en ayant recours aux méthodes de dynamique moléculaire. Il s'agit également d'étudier l'impact de ces caractéristiques microscopiques sur les propriétés tribologiques du système. Les liquides ioniques choisis en tant qu'huiles lubrifiantes potentielles présentent des propriétés biodégradables et des caractéristiques tribologiques appropriées. Ils reposent sur des cations alkylammonium combinés avec des anions alkylsulfonate et bistriflamide. Notre étude est structurée en quatre parties. Elle commence par l'analyse des liquides ioniques purs puis, des liquides ioniques confinés entre deux surfaces de fer à l'équilibre et sous cisaillement, et enfin, en présence d'eau.

Les propriétés structurales et dynamiques des liquides ioniques sont étudiées à travers la fonction de distribution radiale et les coefficients d'auto-diffusion. L'organisation des charges ainsi que la formation de micro-domaines en solution sont étudiées conjointement au comportement diffusif des espèces ioniques.

Un champ de forces atomique, basé sur des méthodes quantiques, a été développé pour modéliser les interactions entre les liquides ioniques et la surface métallique. Des calculs DFT ont été réalisés sur des fragments de liquides ioniques en interaction avec un cluster de fer en fonction de la distance et de

leur orientation. Une fonction modélisant des interactions site-site a été ajustée aux valeurs d'énergies fragment–cluster calculées par DFT afin d'obtenir les paramètres du champ de forces. Finalement, la polarisation du métal par les ions a été prise en compte en utilisant un modèle de dipôles induits afin de reproduire l'énergie d'interaction entre les charges et la surface conductrice. Avec ce modèle d'interaction, les simulations de dynamique moléculaire ont permis d'étudier la structure de l'interface entre une surface de fer plane et différents liquides ioniques. Cette analyse s'est concentrée sur l'étude du positionnement des différentes espèces au niveau de la surface, sur l'orientation des chaines alkyles et sur les profils de densité de charge.

Des simulations de dynamique moléculaire hors-équilibre de liquides ioniques en interaction avec des surfaces de fer ont été réalisées en utilisant le champ de forces développé précédemment. Un protocole de simulation, basé sur une définition locale de la pression, a été développé pour prédire de manière quantitative le coefficient de friction en fonction de la valeur de la charge et du taux de cisaillement. La dépendance de la friction avec la charge, la vitesse de cisaillement, la topologie de la surface et la taille de la chaine alkyle du liquide ionique a été étudiée. La variation des forces de friction s'explique par l'arrangement spécifique des ions et l'orientation des groupements du liquide ionique à proximité de la surface.

Finalement, l'effet de la présence d'eau en petite quantité dans une solution de liquide ionique a aussi été étudié à l'équilibre et hors-équilibre. Un potentiel a été construit pour décrire les interactions entre l'eau et une surface de fer en utilisant la même approche que celle décrite précédemment. Des résultats préliminaires concernant la structure de l'interface liquide-métal et la valeur du coefficient de friction ont été présentés et comparés avec ceux obtenus pour les liquides ioniques purs.

Mots clef: Liquides ioniques, surfaces métalliques, modèle d'interaction, simulations de dynamique moléculaire, friction, dynamique moléculaire hors-équilibre, tensor de pression

Contents

List of Acronyms and Symbols

Acronyms	**Signification**
AFM	atomic force microscope
BSSE	basis set superposition error
DFT	density functional theory
ECP	effective core potential
IL	ionic liquid
IK	Irving-Kirkwood
LJ	Lennard-Jones
MD	molecular dynamics
MINILUBES	mechanisms of interactions in nano-scale of novel ionic lubricants with functional surfaces
MSD	mean square displacement
NEMD	non-equilibrium molecular dynamics
RDF	radial distribution function
SDF	spatial distribution function
SFA	surface force apparatus
VACF	velocity auto-correlation function

Symbols	Signification
Latin	
A	contact area
$\mathscr{A}$	general dynamic variable
D	diffusion coefficient
E_{int}	total interaction energy
E	total internal energy
e	elementary charge
F	friction force
F_z	force applied in the z direction
f_{ij}	force on molecule i due to j
$g(r)$	pair distribution function
$\mathscr{H}$	Hamiltonian
i, j	molecule index
$\mathscr{K}$	kinetic energy
k_1,k_2,k_3	reciprocal space vectors
k_B	Boltzmann's constat
L	load
N_a	Avogadro's number
m	molecular mass
P	pressure
$P_2(\theta)$	Legendre polynomial function
$P_{\alpha\beta}$	components of the pressure tensor
q	elementary charge
r	molecular position
r_{ij}	position of molecule i relative to j
r_{iajb}	position of atom a in molecule i relative to atom b in molecule j
T	temperature
$T_{\alpha\beta}$	components of the temperature tensor

t	time
U	potential energy function
u_{ij}	potential energy of particle i relative to j
V	volume
$\mathscr{V}$	total potential energy
v_i	molecular velocity
v_x	shear velocity

Greek

α	convergence factor from the EWALD summation technique
ε	energy parameter of the interaction
ε_r	dielectric constant
ε_0	vacuum permittivity
η	viscosity
γ	a general transport coefficient
μ	friction coefficient
ψ	wave-function
ρ	number density
σ	LJ core diameter

CHAPTER 1

Introduction

1.1 Friction as a Scientific and Technical Problem

Five hundred years years have passed since Leonardo da Vinci distinguished between sliding and rolling friction and formulated the two basic experimental "laws" governing friction between rubbing solids. This was 200 years before Newton even define what a force was. Da Vinci stated that friction is load-dependent and independent of the area of contact. Since then, an interfacial science is born — *tribology* — the science of friction, lubrication and wear.

The practice of applying a lubricant between sliding pairs is called lubrication. Great importance is given to this phenomena since it can prevent friction and wear by avoiding the direct contact between the materials asperities and by lowering the contact temperature. It is estimated that around 6% of the total energy loss in a developing country is due to friction[1], therefore the solution to many tribological problems represents a significant challenge in the fields of aerospace, electronics and mechanics.

It is important to distinguish between two types of friction: static and kinetic. The static friction force represents the necessary force to initiate sliding, and thanks to it we are able to walk and cars are able

to move. The kinetic friction force is the force needed to maintain a smooth sliding with a certain velocity. Consequently, the energy necessary to fight friction is converted into heat and this heat is released to the surroundings as energy losses. Therefore, even a small reduction of friction can represent an immense economical outcome. In addition to this primary savings of energy, the reduction of the costs involving manufacture and replacement of prematurely worn components can also have a significant economic impact.

Together with the economical aspect, environmental aspects are strong driving forces behind the development of new materials, which are non-toxic and biodegradable. In the last decades, the massive production and release of man-made chemicals has created serious environmental problems such as climate change, water pollution and acidification, air pollution, ozone depletion, global warming and loss of biodiversity. In 1998, Paul Anastas and John C. Warner defined the 12 Principles of Green Chemistry, encouraging people for the design of "environmentally friendly" compounds[2].

The need to develop new, environmentally acceptable lubricants was one of the basis for establishing the *Minilubes* (mechanisms of interactions in nano-scale of novel ionic lubricants with functional surfaces) network, a Marie Curie Initial Training Network financed within the 7th Framework Program of the European Commission. Its focus is on ionic liquids as lubricants for metals, ceramics and coatings. This consortium brings together a community of designers and manufacturers of lubricants and a community of scientists specialized in the synthesis and characterization of chemical structures and investigation of the physical and chemical properties relevant for lubrication.
The key activities of the network are the following:

- Design of "environmentally friendly" lubricants based on ionic liquids.
- Preparation of new types of tribosystems with advanced materials and surfaces for low friction/wear interaction with ionic lubricants.
- Tribological behavior of ionic liquids as lubricants; physical-chemical and thermodynamical properties of the target ionic structures.
- Build predictive tools for the ionic liquids properties and lubricant performance.

- Design strategies towards economically friendly synthesis of ionic liquids.

The present doctoral project is included in this network. Our task is to build accurate models that describe the molecular interactions between ionic liquids and metallic surfaces. Then, to use those models to predict rheological properties and to evaluate lubricant performance based on the structure and interactions occurring at the solid-liquid interface, the nature of which will control the friction, wear and lubrication behavior. During friction, forces are transmitted, mechanical energy is converted and the surface topography of the interacting materials can be altered. Understanding the nature of these interactions constitutes the essence of this thesis.

1.2 Introduction to Tribology

The word tribology comes from the Greek word $\tau\rho\iota\beta o\sigma$ (TRIBOS) meaning rubbing. It is defined as the "*science and technology of interacting surfaces in relative motion and of related subjects and practices*"[3]. Therefore the subject of *tribology* includes more than just the study of rubbing surfaces; it deals with every aspect of friction, lubrication and wear. This term exists for only approximately twenty years, although engineers and scientists deal with the same topics as tribologists since the existence of mechanical devices.

Sliding and rolling surfaces represent the key to much of the technologic devices of today. It is important to understand the tribological principles before designing machine elements because, as already mentioned in the previous section, friction is a source of energy loss and can have an impact in the economy by the early replacement or reparation of worn machine components.

Friction is the resistance to motion that is experienced whenever a solid body moves over another. Wear is the surface damage or removal of material from one, or both of two solid surfaces, in a moving contact. Many techniques are used to control friction and wear including the application of special materials, coatings and surface treatments. One of the most efficient means to control friction is through lubrication. Lubricants can be solid, liquid or gas and their primary role is to avoid direct contact between the sliding or rolling materials.

Attempts to reduce friction dates from the paleolithic period, but it was just in the renaissance period that the engineer and artist Leonardo da Vinci (1452-1519) postulated the rules governing the motion of a rectangular block sliding over a flat surface[4] (Figure 1.1). He introduced, for the first time, the concept of friction coefficient as the ratio between the friction force and the normal load. However, his notebooks remained unpublished for hundreds of years and his work had no historical influence.

It was only in 1699, that the french physicist Guillaume Amontons is credited with the first published study of the classic friction laws[5]. Amontons observed that the friction force (F) is proportional to the normal load (L) and independent of the contact area, as long as the rolling materials and their

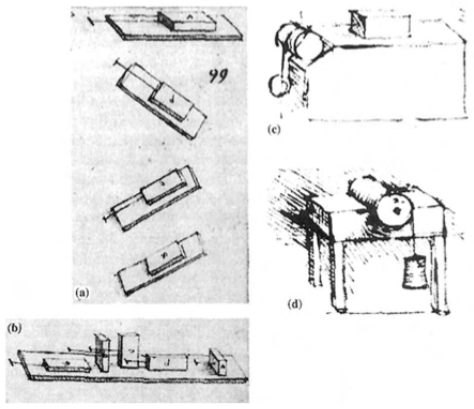

Figure 1.1: Leonardo da Vinci's studies of friction. Sketches representing his experiments to determine: (a) the force of friction between horizontal and inclined planes; (b) the influence of the contact area in the friction force; (c) the friction force by means of a pulley and (d) the friction torque on a roller and half bearing. Picture taken from Dowson, 1979[4].

weights are equal. After, a third law was added to these two by Coulomb, another french physicist. He introduced that the friction force is independent of the sliding velocity[4]. These three laws can be summarized as follows:

1. $\mu = F/L =$ constant (Amontons' 1st Law)
2. μ is independent of the contact area (Amontons' 2nd Law)
3. μ is independent of the sliding velocity (Coulomb's Law)

The observations of Amontons and Coulomb remained empirical up to the middle of the last century when Bowder and Tabor finally gave an explanation[6] based on the roughness of the contacting surfaces. They realized that the real contact happens only on the asperities (where atom-atom interaction takes place) and that the actual area of contact is only of the order of the 10^{-5} of the visible area[1]. These points of contact will be themselves under extreme pressure condition and with the increase of load, the real contact area grows due to an increase of the number of contacts between the asperities.

In consequence, the necessary friction force to maintain a certain sliding will also increase. As a result, the ratio $\mu = F/L$ remains approximately constant, explaining the Amontons' 1st Law.

Later, advances in nanotechnology with the build-up of "tip-based technologies" like the atomic force microscope or the friction force microscope, together with the development of reliable molecular simulations of many-body dynamics demonstrated that the classical friction laws are only valid approximately. Friction does depend on the sliding velocity and these laws are not valid over large ranges of loads[7]. Also, the presence of adhering surfaces is not taken into account. Despite this, Amontons' and Coulomb's laws are remarkably well obeyed for a wide range of materials (rough or smooth) such as wood, ceramics and metals, as long as they are non adhesive.

Who first introduced the concept of adhesion between two surfaces and its relation to friction was Desaguliers (1734), a French-born British philosopher. He considered the argument of Amontons 2nd Law about surface roughness and made the remark that "as surfaces are made smoother they ought to slide more easily, yet it is found by experience that the flat surfaces of metals or other bodies may be so far polished as to increase friction". However, because this was a contradiction to the independence of friction on the contact area, his ideas were rejected. Later, Bowder and Tabor and their definition of *real contact area* solved the origin of this conflict by considering that the classical friction law of Amontons is in fact based in the *apparent area of contact*.

Adhesion is an important phenomenon to take into account when measuring friction. The next section contains some notions about the nature of adhesion and its influence in the frictional properties.

1.2.1 Adhering Surfaces

It is important to understand the mechanisms of adhesion when dealing with metallic surfaces and organic lubricants, the objects of this study. This section intends to give some notions about adhesion, its mechanisms and how it can influence interfacial phenomena.

Adhesion is a term related to the force required to separate two bodies in contact with each other.

There are several mechanisms of adhesion: mechanical, chemical, dispersive, electrostatic and diffusive, which will be briefly explained. Mechanical adhesion happens when adhesive materials fill the voids or pores of the surfaces and hold surfaces together by interlocking (Ex.: velcro); chemical adhesion occurs when two materials share electrons and form ionic, covalent or hydrogen bonds; dispersive adhesion, also called physisorption, exists when two materials are held together by van der Waals forces; electrostatic adhesion happens if the two materials are charged, creating an electrostatic interaction at the point of contact; and diffuse adhesion occurs when the materials are soluble in each other and merge at the joint (Ex.: when ceramic powders are pressed together and heated, atoms diffuse and all particles are joined into one, in a mechanism called sintering).

The correlation between friction and adhesion — that the stronger the adhesion, the more significant becomes the friction force — is supported by several authors. Early in 1999, Robbins and co-workers[8] verified by molecular dynamics simulations that static friction, i.e., the force needed to initiate sliding, is non-zero between two clean crystalline surfaces, although all experiments in ultrahigh vacuum conditions had shown the opposite. They introduced the concept of *third body*, which means that any surface exposed to ambient air will acquire adsorbed layers of hydrocarbons and small molecules, the origin of static friction. This same behavior is found in the origins of the kinetic friction[9].
Derjaguin[10] proposed the following modified version of Amontons' equation for adhering surfaces:

$$F = L_0 + \mu L \tag{1.1}$$

where L_0 is the term added to the external applied load L, to account for the intermolecular adhesive forces. The meaning of this term it is that even at zero load, there will be a non-zero friction associated to the adhesion of lubricant particles at the surface[11;12]. As a consequence of this modification, the friction coefficient will be no longer independent of the load, in disagreement with the Amontons' 1st Law, and becomes instead:

$$\mu = \frac{F - L_0}{L} \tag{1.2}$$

where $\mu = \infty$ at zero applied load. Also, this "internal" adhesion-dependent contribution to the load (L_0) will be proportional to the number of interatomic or intermolecular bonds that are broken and reformed when the adhering surfaces are rolling against each other. Plus, the number of bonds is directly proportional to the contact area. In the case of non-adhering surfaces, the friction force is given by Amontons' 1st Law and independent of the contact area.

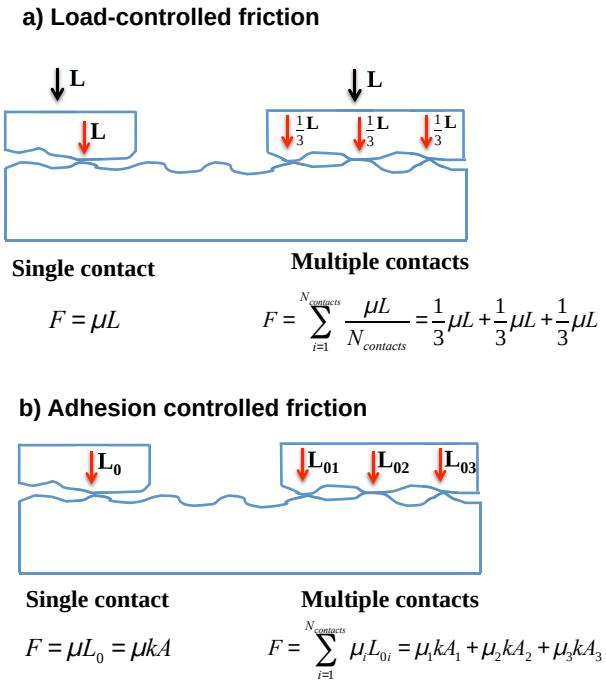

Figure 1.2: Total friction force F in (a) non-adhering and (b) adhering surface.

Figure 1.2 presents an example: in a non-adhering surface (case a), when a certain load is applied, the total friction force follows the Amontons' Law for both single and multiple contact points. In this case we have a load-controlled friction which is always proportional to the applied load, independent of the number of contacts ($N_{contacts}$) and their geometry. In the case of adhering surfaces (case b),

even when zero load is applied there will be an effective L_0, proportional to kA, where A is the real local contact area, which is proportional to the number of intermolecular bonds forming and breaking across each single contact point. Thus, for adhesion controlled friction, the friction will be proportional to the intermolecular interactions.

The roughness of the surfaces can also lead to significant differences in the adhesion and friction forces when comparing with molecularly smooth surfaces. In fact, if the surfaces are perfectly smooth one can say that the real contact area is the same as the apparent one. However, this is not the case if the surfaces are rough and in that case the real area of contact can be smaller than the apparent one if the surfaces are hard. Or in contrary, well above, if the surfaces are soft.

Another important aspect linked to the adhesion of particles at the surface is the phenomenon of adhesive wear. In contrast to the abrasive wear which arises when hard, rough surfaces slide against a softer material, in adhesive wear asperity junctions plastically deform causing wear debris and material transfer from one surface to another.

1.2.2 Lubrication Mechanisms

Sliding surfaces are separated by lubricant materials to prevent direct contact between the asperities, to promote film formation and prevent friction and wear. Lubricants can be solid (self-lubricating materials), greases or oils (liquid lubricants), being the last category of lubricants the most commonly used in machinery. When a liquid is introduced between two sliding surfaces a film will be formed in each surface depending on the viscosity of the fluid, one of the major properties of lubricating oils. Furthermore, the surface chemistry of the substrate, the surface tension of the liquid and its ability to wet the solid surface are also important factors in the formation of a lubricating film.

The way friction depends on the viscosity of the lubricant, the sliding velocity and the normal load is illustrated in a Stribeck diagram (Figure 1.3). According to the separation distance between the sliding surfaces, the lubrication regime can be: boundary, mixed or hydrodynamic[13]. Thus, under extreme operating conditions, the lubricating system can transit from a hydrodynamic regime, with

full-film formation between the surfaces, to a boundary regime where the load is fully carried out by the contacting asperities. A brief description of the different regimes will now take place.

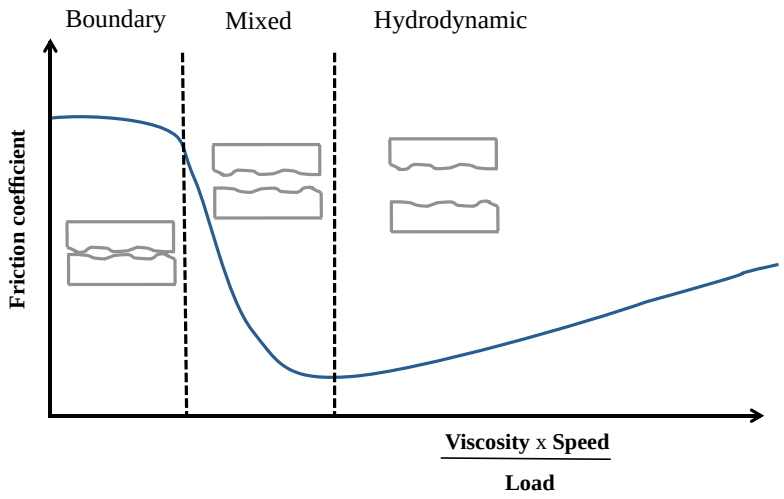

Figure 1.3: Fluid lubrication regimes depending on the separation distance between the sliding pairs: boundary lubrication, mixed lubrication and hydrodynamic lubrication.

The boundary lubrication regime refers to very thin lubricating films, i.e., when the surface separation approaches the molecular dimensions. The load is carried out by the surface asperities and the contacting areas are protected by physically adsorbed molecules of the lubricant. Furthermore, the high temperatures experienced in the asperity-asperity contact points will induce chemical reaction between the fluid and the surface, forming a tenacious film (boundary film). These reactions usually cause degradation of the lubricant, however under certain conditions they can prevent severe wear of the sliding pairs. In other words, tribochemical reactions can be beneficial or damaging for lubrication and until present these phenomena have not been clearly understood.

In the mixed lubrication regime, a hydrodynamic pressure is build up in the lubricant with the increase of the sliding velocity. The load is carried by the combination of the pressure between the asperities of both surfaces and the hydrodynamic pressure in the fluid. The tribological performance of a lubricant in this regime depends essentially on its ability to form tribo-layers at the surface, which are capable

of supporting high loads and prevent serious breakdown of the asperities.

Finally, in the hydrodynamic lubrication, the surface asperities are completely separated by a lubricant film. The applied load is fully supported by the viscosity of the lubricant and wear hardly occurs. In this regime, the viscosity of the lubricant, the applied load and the sliding velocity are the major factors that influence lubricant performance. If the liquid is Newtonian, meaning that its viscosity does not change with shear, then the friction will increase linearly with the shear rate.

An intermediate state can occur between the mixed and the hydrodynamic regimes, which is the elasto-hydrodynamic lubrication. It is characterized by the elastic deformation of the surfaces when although separated, some contact still occurs between the asperities. In this regime, as in the mixed lubrication case, load is supported in part by the contacting areas and another part, by the viscous resistance of the lubricant.

Despite the numerous tribosystems designed to work in the full-film lubrication regime (ex.: hydrodynamic journal bearings), the interest in employing thinner films between the rubbing surfaces has increased. Therefore, it is essential to explore the lubrication mechanisms in the boundary lubrication regimes, where the lubricant is confined to thinner films of only few molecular layers. In confinement, diverse factors including the physical or chemical adsorption of lubricant molecules at the surface, charge, polarizability and layering tendenciy can play an important tribological role. In fact, experiments and simulations reveal significant changes in the static and dynamic properties of fluid films as their thickness is reduced to few layers. Particularly for viscosity, it was proved that it can be some orders of magnitude higher than in the bulk, in fluids under confinement[14]. These changes have important implications for the function of boundary lubricants.

Advances in nanotechnology, with the arrival of more and more sophisticated micro- and nano-mechanical devices, prompt the development of new experimental and simulation techniques that can access the molecular scale. The atomic force microscope (AFM) and the surface force apparatus (SFA) are examples of such experimental techniques. AFM and SFA have proven to be ideal tools for measuring at the molecular level both normal and lateral forces between a radius tip and a surface and

between two molecularly smooth surfaces that confine a lubricant film of measurable thickness[12].

Israelachvili, one of the pioneers in this field, used SFA measurements to study the friction forces between molecularly smooth mica surfaces confining thin films of branched hydrocarbons[15]. The author found that when the systems are subjected to shear, two very distinct dynamic regimes are observed: at higher shear velocities (sliding is rather smooth), the friction force is relatively constant and there is no stick-slip behavior. However, when the velocity of sliding is slower than a given critical velocity, the friction force oscillates between "static" and "kinetic" friction forces, with the condition of "stick" being followed by the condition of "slip", in a continuous way. The same authors also point to the fact that molecules tend to align in the direction of shear, which boosts the formation of organized solid-like structures.

In the same line but several years before, Gee and co-authors[16] had already investigated the transition between liquid-like to solid-like behavior in confined fluids under shear. They verified that the liquid-like behavior at a smaller film thickness persists, as the chain length of the hydrocarbons increases. In the case of a spherical molecule, the solid-like behavior was instantly seen after the surfaces were sheared. In the first case, only after some sliding distance, with the alignment of the lubricant chains, the solid-like behavior was observed.

The tendency of fluids to form layers in confinement conditions was investigated using ionic liquids between silica surfaces[17] and between molecularly smooth mica surfaces[18], using SFA. Both studies revealed that ionic liquids are arranged in layers at the surface when this last one is negatively charged. Moreover, the viscosity increases as the surfaces approach towards one another and the liquid film is composed of only few layers. The viscosities of the confined ionic liquids are found to be 1–3 orders of magnitude higher than in the bulk ionic liquids[17]. This is caused by a highly structured film at the surfaces and due to the intermolecular interactions happening between the ion layers adjacent to the walls[19].

In conclusion, the nature and strength of the interactions occurring between the fluid molecules and the surface clearly affect the lubrication mechanisms and the frictional properties of the system. This high-

lights the importance of investigating and understanding the interfacial phenomena at the nanoscale.

In the next section, general properties of ionic liquids and their application as fluid lubricants for metallic surfaces will be discussed.

1.3 Ionic Liquids

1.3.1 General Properties and Applications

Ionic liquids are complex salts composed of a large organic cation and an organic or inorganic anion, which are liquid below 100° C. Typical structures of ionic liquids are presented in Figure 1.4.

In the last decade the number of research studies and applications of ionic liquids increased drastically. This is related to their remarkable properties which include an extremely low vapor pressure, reasonable viscosity-temperature behavior, high thermal stability at high temperatures, non-flammability, among others[20].

There are thousands of possible combinations of anions and cations, allowing the synthesis of task-specific compounds by adjusting key intermolecular forces. As such, the properties of ionic liquids can be fine-tuned for a specific application, by selecting different functional groups in the cation or the anion or, for example, by having different lengths in the alkyl side chains.

The major difference between ionic liquids and other common molten salts like NaCl or KCl is the low melting point. For example, NaCl and KCl have melting points of 801° C and 770° C, respectively, whereas the ionic liquid 1-butyl-3-methyl-imidazolium chloride is liquid at 70° C. The explanation lies in the large and asymmetric cation of the ionic liquid, which leads to a difficult packing of the ions and to a weak ionic bond between cation and anion. With the decrease of the lattice energy of the crystalline form of the salt, the melting point also decreases[21].

The low vapor pressure, in the order of 10^{-10} Pa at 25° C, is the most important property responsi-

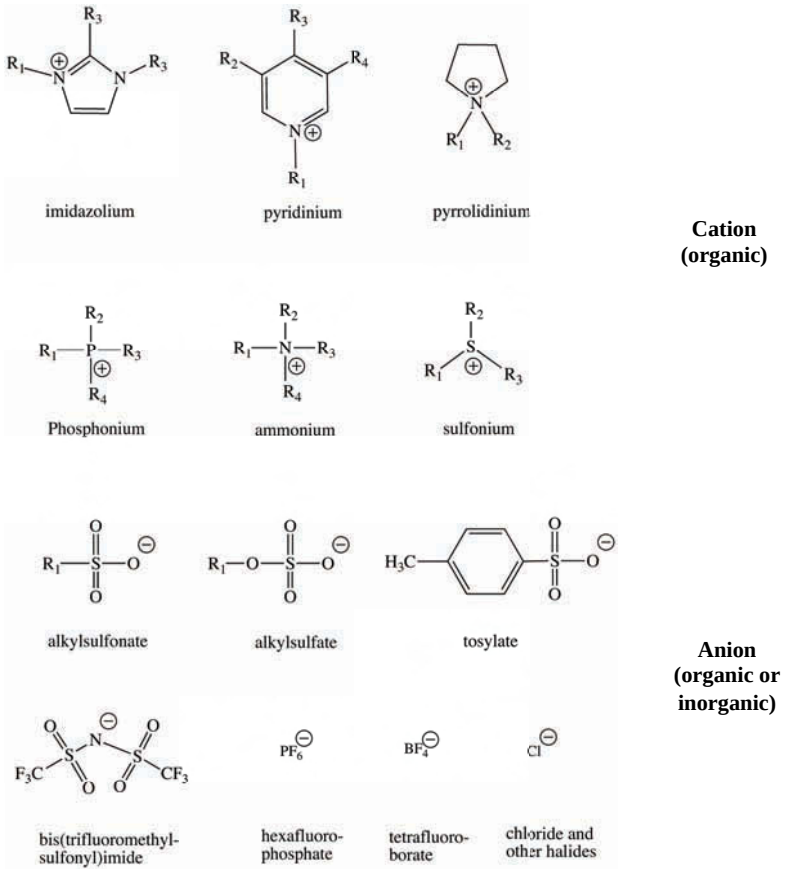

Figure 1.4: Typical ions in the ionic liquids structure. Ionic liquids are composed of an organic cation and organic or inorganic anion.

ble for the high level of interest in these compounds. Each ion in solution will be surrounded by a symmetric shell of ions of opposite charge, promoting ion-ion interactions. Among the interactions taking place in ionic liquids, the Coulombic interactions are predominant. They increase the cohesive energy, which is consistent with the low vapor pressure of ionic liquids.

One of the most explored applications of ionic liquids is in organic synthesis. Their negligible vapor pressure makes them ”green” solvents for reaction media in substitution to the volatile organic solvents[22]. Furthermore, the different functional groups present in their molecular structure allows to taylor the miscibility of ionic liquids and aqueous or organic phases. Additionally, their polar structure can also induce to the formation of microdomains in mixtures, separating polar and nonpo-

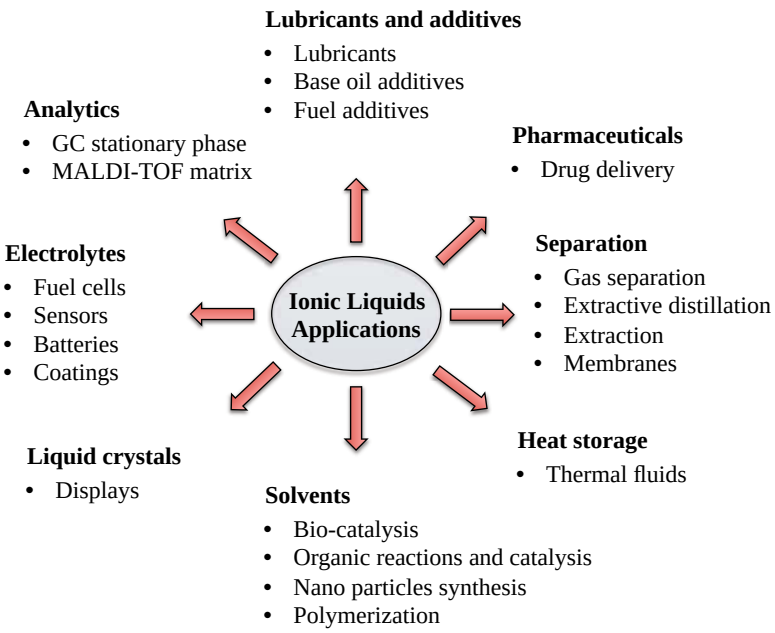

Figure 1.5: Possible applications of ionic liquids, which are already described and patented.

lar phases[23;24]. Besides synthesis, ionic liquids are involved in many other applications[25], summarized in Figure 1.5.

Regarding their composition, ionic liquids come in different classes that basically include protic, aprotic and zwitterionic types, each one suitable for a specific application[26] (Figure 1.6). The protic ionic liquids are formed through an acid-base reaction where a Brönsted acid (AH) transfers a proton to a Brönsted base (B) yielding the species $[BH^+][A^-]$:

$$AH + B \rightarrow [BH^+][A^-] \tag{1.3}$$

The main application of this class of ionic liquids is as electrolytes for fuel cell applications, due to their high thermal and electrochemical stability[27]. Aprotic ionic liquids don't involve proton transfer and typically there is an alkyl side chain at the place of the labile proton present in the correspondent

protic species. They are formed by synthesis and are the most commonly used class of ionic liquids with applications in the fields presented in Figure 1.5. Finally, the zwitterionic ionic liquids have both the negative and the positive species in the same structure and they can have applications in lithium-metal batteries[28] and also membranes for separations[29].

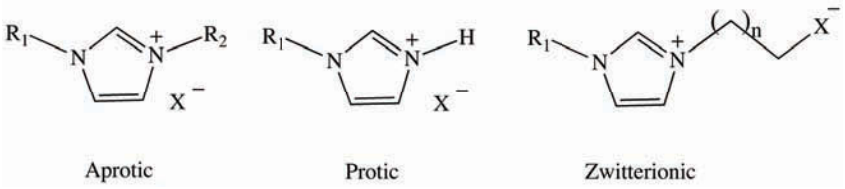

Figure 1.6: Different types of ionic liquids: protic, aprotic and zwitterionic.

The present study will be focused on aprotic ionic liquids for applications as lubricants. The next section, contains a discussion concerning the properties important for such application.

1.3.2 Ionic liquids as Environmentally Acceptable Lubricants

Ionic liquids have been considered in the last decade as promising candidates for tribological applications[30–32]. Their remarkable properties suitable for lubrication include negligible vapor pressure, non-flammability, high thermal-oxidative stability and reasonable viscosity-temperature behavior. The reason why these properties are so important for lubrication is that at the surfaces contact points the temperature will increase due to friction, therefore the thermo-oxidative stability of the lubricant is essential to minimize its degradation during sliding. For the same reason and also for storage purposes, the non-volatility and non-flamibility are very important properties when choosing a lubricant oil. The viscosity behavior of the ionic liquid is also an important property, as already explained in section 1.2.2, since it determines the load-carrying capacity of the fluid and the film formation at the sliding surfaces. In addition, the polar structure of ionic liquids will contribute to the formation of an adsorbed layer at the sliding surfaces, which can potentially reduce friction and wear[33].

Designing a lubricant oil with suitable physical and chemical properties and appropriate tribological

behavior is a complicated task, hence ionic liquids are highly promising candidates.

Generally ionic liquids can be used as net lubricants or additives for common lubricant oils. This last possibility has been largely explored in the last few years since the presence of ionic liquids as additives can enhance the anti-wear behavior of the lubricant oil by preventing some tribochemical reactions at the surface like corrosion and oxidation[34;35]. Among the possible cationic moieties, imidazoliums are by far the most studied structures, followed by ammoniums, aromatic amines and phosphoniums. The works of Liu and co-workers showed the excellent tribological performance of several imidazolium-based ionic liquids[36;37] and their antiwear/anticorrosion properties when used as additives for poly(ethylene glycol)[38;39] and polyurea grease[40].

Because of the tuneability of their properties, ionic liquids are considered designer fluids. As such, task-specific compounds can be obtained by adjusting molecular structures and key intermolecular forces between the ions. Some combinations of anions and cations may not be liquid at room temperature and certain properties of ionic liquids, such as melting point and viscosity, are strongly dependent on the molecular structures such as the nature of the charged head groups, the nature and length of alkyl side-chains[23] and the presence of functional groups such as hydroxyl, cyano, etc. Therefore, by changing these groups it is possible to fine-tune relevant properties of ionic liquids, for their application in the lubricating industry.

Due to the large number of possible ionic structures suitable for lubrication, structure-property relations need to be established in order to obtain insights about lubricant performance. Generally, friction and wear volume decreases with an increase of the chain length of the alkyl group in the cation, as a consequence of the increased viscosity[41] (Figure1.7).

The anions can have an equally important influence in the tribological performance of the ionic liquids. Anions can change the viscosity of the ionic liquid and affect the formation of a boundary film, either by physisorption or chemical reaction. For example, it is known that BF_4^- and PF_6^- can corrode steel under humid condition due to the formation of the species HF, by hydrolysis. Furthermore, for the same contacting surface, the ionic liquid with the anion bis(trifluoromethylsulfonyl)imide (or sim-

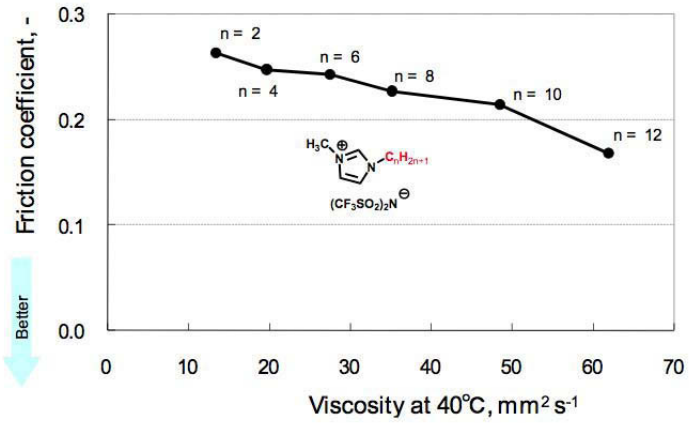

Figure 1.7: Effect of alkyl chain length in the imidazolium cation on the friction coefficient. Plot taken from reference[30].

ply bistriflamide) — NTf_2^- — presents better anti-wear properties than BF_4^- or PF_6^-. The reason for this is a tribochemical reaction which takes place between NTf_2^- and steel with the formation of a surface-protective film composed of organic fluoride, inorganic fluoride and FeS, that helps to prevent friction and wear[42]. In fact, compounds that are formed by chemical reaction between the anion and the material's contact points (where temperatures are high) are of crucial importance in preventing seizure in freshly generated metal surfaces. This is probably one of the basic reasons why ionic liquids have superior tribological performance than conventional lubricant oils.

In the present study, ionic liquids with suitable ecotoxic and biodegradable properties and appropriate tribological features were chosen as potential lubricant oils. Their chemical structures are based on tetraalkyl-ammonium cations ($N^+_{1R_1R_2R_3}$) combined with different families of anions including alkyl-sulfonate ($R_1SO_3^-$), alkylsulfate ($R_1OSO_3^-$) and NTf_2^-. These structures can be seen in Figure 1.8.

The main idea behind the choice of these particular structures as potential lubricant oils is to have the best possible "environmentally friendly" combination of ions, without losing lubricant performance. Taking this into account, the choice for the ammonium cations was linked to their good performance as lubricants or additives when associated with the anion NTf_2^- [43]. Sulfonate and sulfate anions where

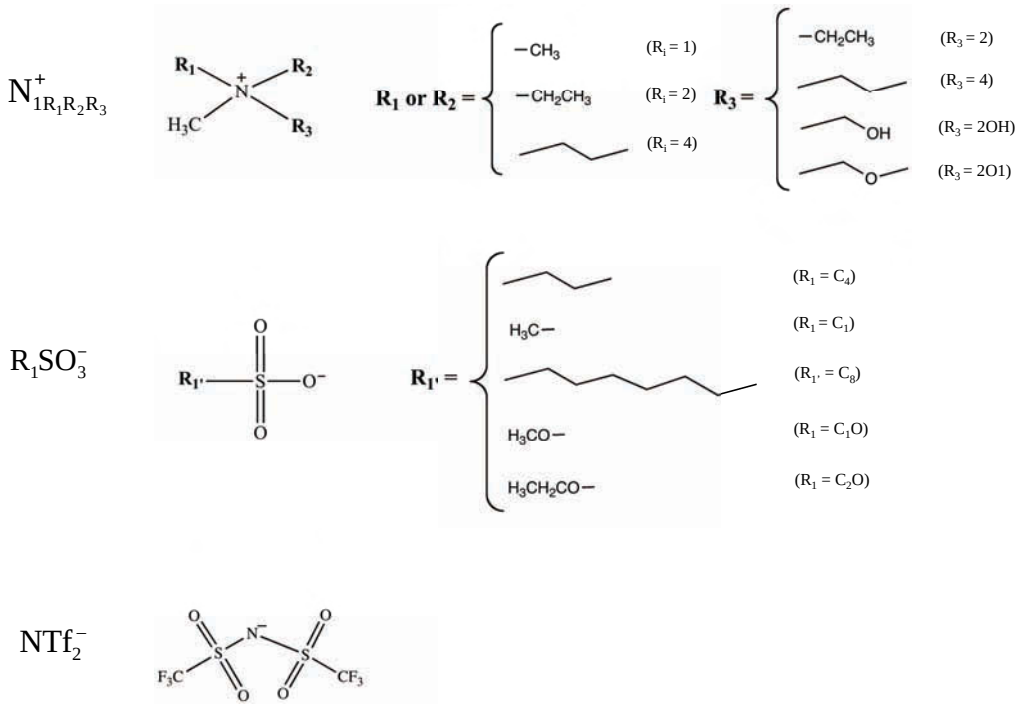

Figure 1.8: Molecular structures of the potential ionic lubricants studied in the present work.

preferred due to their low environmental impact when compared to fluorinated anions[44;45], which are very common in ionic liquids.

Ecotoxicity and biodegradability testes were performed based on these structures[45]. One of the main results was that cholinium cations with methylsulfonate $[N_{1112OH}][C_1SO_3]$ and methylsulfate $[N_{1112OH}][C_1OSO_3]$ exhibit low toxicity and an excellent biodegradability. For the tetra-alkyl-ammonium cations N^+_{1112O1} and N^+_{1222}, a poor biodegradability was found. The anion NTf_2^- shows some resistance to biodegradation, which combined with its pronounced hydrophobicity (high probability of bioaccumulation) should not recommend this ionic liquid to be considered for applications with a potentially high environmental exposure. In general, the more polar is the investigated compound, the lower is its bioaccumulation potential, this last criterion being very important when choosing "environmentally friendly" chemicals.

The thermo-oxidative stability and corrosion behavior of these ammonium based ionic liquids struc-

tures was evaluated using aging mechanisms, which consist in the application of harsh conditions to the lubricant sample during a short period (some days), in order to accelerate the degradation process[46]. The tests showed that the ionic liquid composed of the NTf_2^- anion with butyl-trimethyl-ammonium N_{1114}^+ was highly stable under the artificial aging procedures applied, in oxidative or well-defined humid conditions. The same was observed for the NTf_2^- anion with the cholinium cation N_{1112OH}^+. Contrary to what was expected, this last ionic liquid showed resistance towards decomposition, although under the conditions of long-term thermo-oxidative stress this may not be the case.

In summary, the ionic liquid structure that presented the best compromise between thermo-oxidative stability, low corrosiveness and low environmental impact was $[N_{1112OH}][NTf_2]$, despite some drawbacks concerning the usage of this anion due to its less easy biodegradation.

The tribological performance of ionic liquids based in alkylammonium cations with methylsulfonate and methylsulfate anions was investigated, as additives for glycerol and as neat ionic liquids[47]. The tests were performed in a ball-on-disc configuration by lubricating steel-steel couples. When used as additives, the ionic liquids with the sulfate and sulfonate anions induced a strong reduction of friction and wear when compared to the base oil, and sulfates were in all cases found to have a better performance than sulfonates. Concerning friction, in general these ionic liquids presented better results than the NTf_2^- anion-based ionic liquids, however, sulfates and particularly sulfonates could not achieve the same efficiency for the anti-wear behavior of fluorine-containing compounds. Nevertheless, XPS measurements showed the formation of a tribo-active film under lubrication with the sulfate anion-based ionic liquids, indicating the formation of a wear-stable film of iron sulfide.

1.4 The Organization of Ionic Liquids at Metallic Surfaces

The structure and interactions occurring at the solid–liquid interface can have great influence in the performance of a lubricant. All electrochemical reactions (such as corrosion) and catalytic reactions take place at the interface, therefore it is important to understand the distribution of the various particles in this region. Also, the interface is the locus of particular hydrodynamic behavior, such as stick-slip regimes. The structure and dynamics of the ionic liquids at the interfacial layer are certainly different from the bulk properties.

The first model of an interface between a surface (electrode) and an electrolyte solution was given by Helmholtz, in 1881. He pointed out that the difference in the electric potential between a metal and a solution implies charge separation at the interface. In this simple model, the electrode–solution interface is treated as two rigid plans of charge. One plane, the outer Helmholtz plan (OHP), is due to the ionic charge and the other plan is that of the electrode itself (Figure 1.9a). Such structure resembles a parallel plate capacitor, for which the differential capacitance C_d is given by:

$$C_d = \frac{\varepsilon_r \, \varepsilon_0}{d} \tag{1.4}$$

where ε_r is the dielectric constant of the medium, ε_0 is the vacuum permittivity and d is the space between the plates. The Helmholtz layer model ignores the disrupting effect of thermal motion, which tends to break up and disperse the OHP. Also, this model predicts that C_d is constant, while in real systems it is a function of voltage and concentration[48]. The concept of *electric double layer* is based in the Helmholtz model.

Later, in 1910, Gouy and Chapman presented the *diffuse layer theory*, where the ions of opposite charge are spread through the solution adjacent to the charged electrode, up to a few nanometers (Figure 1.9b). The definition of capacitance in this model is the following:

$$C_d = \left(\frac{z\varepsilon_r\varepsilon_0 e^2 n^0}{k_B T}\right)^{1/2} \cosh\left(\frac{ze\varphi_0}{k_B T}\right) \tag{1.5}$$

where z is the charge magnitude of each ion in an electrolyte solution with an equal number of ions ($z:z$), n^0 is the ion number density, φ_0 is the potential at the OHP with respect to the bulk solution and the rest of the symbols have their usual meaning (see list of symbols). Nevertheless, this theory has a limitation. Since it is derived from a from a Debye-H*ü*ckel approximation, it is only valid for very diluted electrolyte solutions.

In the Debye-H*ü*ckel theory, the departure from ideality of an electrolyte solution is explained in terms of the chemical potential of the ions. Opposite charges attract one another. As a result, anions are more likely to be close to cations and *vice-versa*. Although the overall solution is neutral, near any given ion there is an excess of counter ions. If we think of a sphere of radius r_d around a central atom, r_d will be screening distance, after which the charge density is zero. This radius is defined as the Debye length and it is given by the following equation:

$$r_d = \left(\frac{N_a e^2}{\varepsilon_r\varepsilon_0 k_B T}\sum_i z_i^2 c_i\right)^{-\frac{1}{2}} \tag{1.6}$$

where z_i is the charge of ion i and c_i is the concentration of ion i in mol·m^3. Inside that sphere, the energy and therefore the chemical potential of any given central atom is lowered, as a result of the electrostatic interactions that the ion establishes with its counter ions. The model leads to a prediction of the activity coefficients of electrolyte solutions, however, it is limited to very low concentrations of electrolyte, predicting only accurate results when the molality of the solution is close to zero. As it can be seen through equation 1.6, the Debye length decreases with the concentration of ions in solution. For example, the Debye length of an aqueous solution of NaCl 0.01 M is of 5 nm, therefore in a molten salt (or in an ionic liquid) were the concentration of charges is enormous, the Debye length will be very

small. To have an idea, for a concentration of 5 mol/L of the ionic liquid 1-butyl-3-methylimidazolium bis(trifluoromethylsulfonyl)imide ($\varepsilon_r = 14.0$[49]), the Debye length is of 0.06 nm. Therefore, a *diffuse layer theory* is unlikely to describe the structure of ionic liquids at the interface.

Finally, in 1924, the Helmholtz and the Gouy and Chapman theories are combined in the *Stern model*, in which the ions closest to the electrode are constrained into a rigid Helmholtz plane while outside that plane the ions are dispersed as in the Gouy and Chapman model (Figure 1.9c).

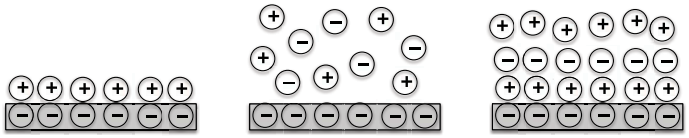

Figure 1.9: The three common models to describe the charge distribution of an ion near an interface are the a) Helmholtz; b) Gouy–Chapman and c) Stern models.

All of the three models, or combinations of them, have already been proposed in the description of the ionic liquid–metal interface organization[50–52]. The different models lead to different values of capacitance, which is usually used to evaluate the charge transfer or potential distribution at the surface. Such information is essential in the design of ionic liquids for many applications such as supercapacitors, batteries, solar cells, etc.

The nano-scale organization of ionic liquids at conducting surfaces was already studied experimentally. Spectroscopic studies with imidazolium based ionic liquids at a platinum surface evidenced the formation of a very strong first solvation layer of approximately 5 Å, which corresponds to the cation–anion pair thickness[52]. Furthermore, it was observed that the ionic liquids form essentially a Helmholtz like layer at the interface and that charge ordering does not extend far into the liquid due to the strong screening effects of that ionic medium. The same author also found that the orientation of the imidazolium ring of the cations and the orientation of the alkyl side chains depends on the surface charge. The explanation is given in terms of electrostatic interactions. Thus, as the surface charge is

made negative, the imidazolium ring, where the positive charge is centered, will lie more parallel to the surface to maximize the attractive interaction. Likewise, when the surface is positively charged the imidazolium ring will tilt along the surface normal, making room for the anion to interact with the surface and to screen the positive charge.

Additional AFM measurements at a golden surface showed that the organization at the interface is only extended for three of four layers[53;54], since the interfacial layers of ions will screen the excess charge of the metal. Accordingly, the surface charge on the metal will also reflect the number of ordered layers present at the interface.

Several authors also confirmed such behavior by molecular dynamics (MD) simulation[55–57]. For exemple, Fedorov[57] studied the neutral graphene–ionic liquid interface by MD and concluded that there is the formation of several distinct solvation layers at the surface, with the cations (imidazolium) occupying the 1st layer. The same author also found interesting results by performing Monte-Carlo simulations on the interfacial structure between an ionic liquid and a charged electrode. He found that if the ions have charged heads and neutral "tails", then they can play the role of "latent voids" that can be replaced by charged groups via rotations and translations of ions[58].

The organization of the atoms at the solid-liquid interface plays an important role in the tribological performance of the liquid. Experimental studies with molecularly thin films of ionic liquid between mica surfaces as a function of the surface separation revealed very low friction coefficients for surface separations that correspond to favorable ion packing. Furthermore, the charge of the ions contributes to the formation of a robust film of fluid between the surfaces, that withstands higher values of load, than similar films of uncharged molecules[18]. This strong film of liquid can prevent serious breakdown of the asperities if the surface is rough. Besides, in the asperity-asperity contact points, the resulting high temperatures can induce chemical reaction between the fluid and the surface, promoting the formation of a persistent film (boundary film) which can help to prevent severe wear of the sliding pairs[30]. These properties together with the green character of ionic liquids, makes them good candidates to lubrication.

1.5 Research Strategy

The approach followed in the present work is to study the behavior of ionic liquids at metallic surfaces using molecular dynamics simulations. This class of methods have proved to be an important tool in describing and predicting macroscopic thermodynamic properties, by mimicking the physical movement of atoms and molecules at the nano-scale. MD is widely used in the fields of chemistry, biology and materials science to study small chemical systems or even large biological molecules or material assemblies. The description of the MD principles is given in Chapter 2.

Molecular simulations have revealed to be important in providing molecular insights about the tribological properties of a system at the nanoscale[9;59]. The next section will present a quick review on the simulation studies which involve the prediction of tribological properties.

1.5.1 Molecular Simulation of Tribological Properties

Remarkable advances in computational hardware, coupled with the development of accurate methodologies to study chemically complex lubricants and surfaces, led to an increase in the number of simulation studies in the field of tribology over the last decade. For example, atomistic computer simulations revealed to be a powerful tool in understanding the microscopic origins of static and kinetic friction, the behavior of boundary lubricants, and the link between molecular structure and tribological properties. These results can provide valuable information in the development and design of new materials and act as input to more traditional macroscopic calculations of tribological properties.

The measurement of friction through molecular simulations is normally associated to non-equilibrium molecular dynamics, characterized by the imposition of a certain shear velocity to one of the surfaces. Commonly, load is also applied in the normal direction. When the system is in mechanical and thermal steady-state, properties like the friction coefficient, friction force and normal force can be extracted, as well as microscopic structure, energetics and dynamic quantities.

Robbins and co-workers analyzed the effect of adsorbed layers of hydrocarbons between crystalline

surfaces, on the static and kinetic friction. Their results showed that such layers lead to non-zero friction coefficients, which is consistent with many macroscopic measurements[8;60;61]. Also, the authors find a logarithmic relation between friction and shear velocity supposed to be associated to thermal activation at the interface, when the shear rate increases. This last result is also confirmed by other authors that studied the kinetic friction in thin layers of oil confined between parallel walls[62]. They support that the kinetic friction coefficient increases first linearly and then logarithmically with increasing sliding velocity.

In the fields of nanotechnology, molecular simulations have been applied to understand nanotribology in general as well as single asperity contacts in particular. As an example, a great number of studies concerns the modeling of realistic AFM tips in contact with alkylsilane self-assembled monolayers[63;64]. Simulation results point for the possibility of the removal of material from the substrate when the system is being sheared, even at extremely low loads.

MD simulations were used to study the asperity-asperity contact behavior between two metallic surfaces confining organic lubricants[65;66]. It is shown that the friction force as a function of load agrees with the modified Amontons' 1st Law for adhering surfaces (see Eq. 1.1), where friction exists even at zero-applied load due to adhesion occurring in the presence of lubricant.

Concerning ionic liquids, the effect of applying a Couette shear flow on an ionic liquid solution have revealed interesting changes in the structure and intermolecular ordering of the liquid when shear is applied[67]. In fact, as the shear rate increases the nanoscale order decreases. This is probably due to a weakly structured coordination shell of cations and anions. Furthermore, the long alkyl side chain of the imidazolium cations of the ionic liquid tend to be aligned with the direction of shear.

The tribological properties of a system composed of ionic liquid contacting with alkylsilane self-assembled monolayers (SAM) on SiO_2 surfaces was studied trough MD simulations[68]. Results point to a reduction in the frictional force between the contacting monolayers at a given load in the presence of lubricant. Moreover, the ionic liquid may incorporate into a damaged area of the SAM coating, restoring its tribological properties.

In spite of all the advances in analyzing tribological properties by MD, studies involving ionic liquids as lubricants for surfaces are quite scarce. This is most probably due to the complex structure of the ionic liquids and the difficulty to describe interactions between the ions and surfaces, that if metallic are conductive or highly polarizable. In a certain way, the present study comes to fulfill this gap.

1.6 Aim of this Work

The nature of the molecular interactions occurring at the solid–liquid interface play an important role in the performance of a lubricant oil, as well as affects wear and adhesion. The aim of this study is to describe at the molecular level the structure and organization of ammonium-based ionic liquids at metallic surfaces and to understand how this influences friction and related forces.

For that, models are build from first principles to accurately describe the ionic liquid–metal interaction taking into account the polarization of the metal surface. The parameters of interaction resulting from such models are then introduced in the MD simulations and the ionic liquid–metal systems are studied both at equilibrium and at non-equilibrium, by imposing shear and load.

Different factors that can influence the organization at the metal surface will be analyzed, such as the nature of the anion, the alkyl side-chain length, the shear velocity and the surface topology.

Although in some situations quantitative predictions can be attained, the most relevant information is usually of qualitative nature, in terms of trends and structure-property relations that can guide the choice of compounds for lubricants. Some of the topics that will be approached along this manuscript include the description of the interfacial layer; the evaluation of the affinity of the ionic liquids for the metal surface; the prediction of reliable friction coefficients and the influence of the ionic liquids chemical structure on the frictional forces. With these and other questions, we hope to give a contribution to the development of high performance lubricants.

Finally, as M.P. Allen and D.J. Tildesley wrote in their classical text[69] *Computer simulation of Liquids* (1987):

> "Eventually, if the model is a good one, the simulator hopes to offer insights to the experimentalist, and assist in the interpretation of new results."

CHAPTER 2

Principles of Computational Chemistry

2.1 Introduction

In computational chemistry, chemical problems are solved by computational methods, using models to describe the real world. Evidently, this doesn't mean that experiment can ever be replaced by a computer simulation, but that both worlds can be combined to efficiently resolve chemical questions. Examples of efficient combinations between computational chemistry and experiment can be divided into three categories: 1) when ambiguity exists in the interpretation of the existing experimental results; 2) to optimize the design and progress of an experimental program and 3) to predict properties which might be especially difficult, dangerous or costly, to measure experimentally. However, computational methods are not without costs, and more sophisticated is the model, the more expensive in terms of computational resources it becomes. The role of a modern computational chemist is also to be able to evaluate the accuracy *vs* cost relationship.

The foundations of computational chemistry reside in the principles of quantum mechanics, in particular in hypothesis developed by De Broglie[70], Born, Heisenberg and Schröedinger. They culminate in the well know Schrödinger's equation, which gives the energy E of a system:

$$\mathscr{H}\psi = E\psi \tag{2.1}$$

where ψ is a wave function, that for a given system, contains the measurable information about the system. And $\mathscr{H}$ is the Hamiltonian, *i.e.*, an operator associated with energy that when applied to the wave function, allows to determine the total energy of a given system. In general, the Hamiltonian takes into account five contributions to the total energy of a system: the kinetic energy of the electrons and nuclei, the attraction of the electrons to the nuclei and the inter-electronic and inter-nuclear repulsions. Considering the Born-Oppenheimer approximation, it is possible to decouple the motion of the electrons from the nuclear motion since the nuclei of molecular systems move much more slowly than the electrons. In this way, the nuclear kinetic energy can be neglected and the nuclei-nuclei repulsion energy is considered constant for a given set of fixed nuclear coordinates.

Apart from the electronic definition of the Hamiltonian, it is also possible to write a molecular Hamiltonian, within the Born-Oppenheimer approximation, of a microscopic system of N atomistic particles (atoms or molecules) as a sum of kinetic and potential energy functions of the set of coordinates q_i and momenta p_i of each molecule i:

$$\mathscr{H}(\boldsymbol{p},\boldsymbol{q}) = \mathscr{K}(\boldsymbol{p}) + \mathscr{V}(\boldsymbol{q}) \tag{2.2}$$

$$\boldsymbol{p} = (p_1, p_2, ..., p_N) \tag{2.3}$$

$$\boldsymbol{q} = (q_1, q_2, ..., q_N) \tag{2.4}$$

were the potential energy $\mathscr{V}$ contains the interesting information regarding all the interactions occurring inside the system. A solution of this equation will generally involve calculating, from $\mathscr{V}$, the forces $\boldsymbol{F_i}$ acting on the molecules. This will be subject of further analysis later in this chapter.

The kinetic energy takes the form of:

$$\mathscr{K} = \sum_{i=1}^{N} \sum_{\alpha} \frac{p_{i\alpha}^2}{2m_i} \tag{2.5}$$

where m_i is the molecular mass and α runs over the different (x,y,z) components of the momentum of molecule i.

It is possible to build, from $\mathscr{H}$, an equation of motion (in Hamiltonian, Lagrangian, or Newton form) which governs the entire time-evolution of the system and all its mechanical properties. This is the principle of molecular dynamics (MD). Furthermore, because the Hamiltonian also dictates the equilibrium distribution function for molecular positions and momenta, it constitutes the basic input parameter to any computer simulation program.

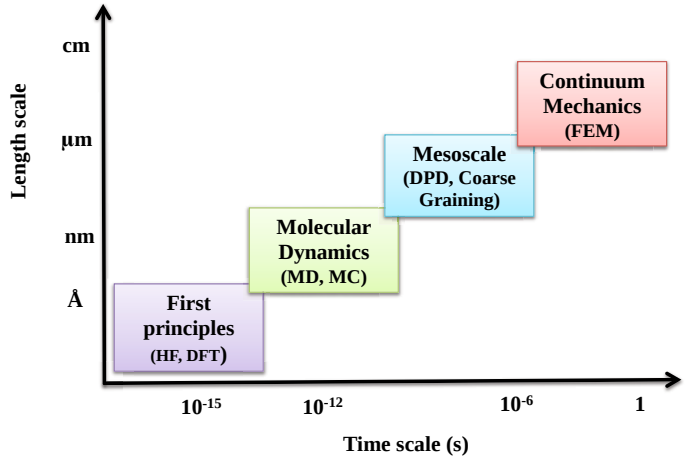

Figure 2.1: Computer simulation approaches required at a given time and length scale. An example of the method name is given in each case. HF= Hartree Fock; DFT=Density Functional Theory; MD=Molecular Dynamics; MC=Monte-Carlo; DPD=Dissipative Particle Dynamics; FEM=Finite elements method.

In this way applying the same basic principle, computer simulation methods describe systems having

different scales of time and space, with the conditions that the appropriate approximation is used in each particular case. Figure 2.1 summarizes the simulation methodology applied in each case.

The passage from one method to the other is made by matching successive levels of description, starting from first principles, ruled by quantum mechanics. In this work, both first principles and molecular dynamics methods (at the equilibrium and at the non-equilibrium) will be used.

2.2 Molecular Dynamics

Molecular dynamics is a powerful technique which allows computing equilibrium and transport properties of many-body systems. In this context, *classical* MD means that the motion of the constituent particles of the system obeys the laws of classical mechanics (Newton's Laws).

In the MD method, the trajectory of the molecular system as a function of time is generated by simultaneous integration of Newton's equations of motion for all the atoms in the system:

$$\frac{d\boldsymbol{r_i}(t)}{dt} = \boldsymbol{v_i}(t) \tag{2.6}$$

$$\frac{d\boldsymbol{v_i}(t)}{dt} = \frac{\boldsymbol{F_i}(t)}{m_i} \tag{2.7}$$

where $\boldsymbol{r_i}(t)$ and $\boldsymbol{v_i}(t)$ are the position and velocity of atom i at a given time t; m_i is the mass of atom i and $\boldsymbol{F_i}$ the total force acting on the atom. These equations can also be applied to a center of mass of a molecule and then, $\boldsymbol{F_i}$ represents the total force on molecule i, m_i the molecular mass and $\boldsymbol{r_i}(t)$ and $\boldsymbol{v_i}(t)$ the position and velocity of the center of mass.

These equations are solved on a step-by-step basis and the time interval δt is typically between 1-10 fs for molecular systems. To have an idea, δt will be significantly smaller than the typical time taken for a molecule to travel its own length.

In general, what a molecular dynamics program does at each timestep, along a simulation, can be resumed in the following steps (accompanied by Figure 2.2):

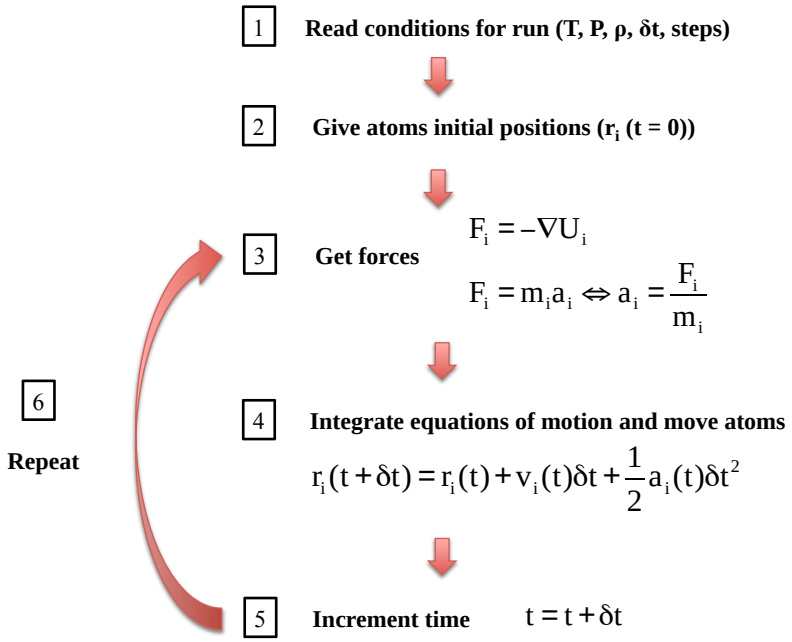

Figure 2.2: Steps performed in a molecular dynamics simulation code.

1. Read the parameters that specify the conditions of the run (temperature, number of particles, density, timestep, interaction parameters)

2. Initiate the system by selecting the initial positions and velocities of the constituent particles

3. Compute the forces acting on each particle

4. Integrate Newton's equations of motion, allowing the atoms to acquire new positions

5. Increment time δt

6. Repeat steps 3, 4 and 5 until the evolution of the system has reached the desired time length

Molecular dynamics simulations are in many aspects similar to real experiments. The latter start with a sample and set-up preparation, followed by the connection of the sample to a measuring instrument which will be used to measure the property of interest, during a certain period of time. The measurement can experience some statistical noise, therefore the longer is the acquisition period, the more accurate the measurement becomes. In molecular dynamics simulation the same approach is followed. First there is the preparation of the sample (consisting of N particles) with the selection of the appropriate interaction model potential, followed by the set up of the system properties (initial temperature, pressure, volume, etc). Newton's equations of motion are then solved until the properties of the system no longer change with time, in a process called equilibration. The actual measurement is performed after the equilibration process, where long simulation times are required to obtain an accurate property estimation.

One of the most important steps in a MD simulation is the calculation of the forces acting on the particles (step 3 of Fig. 2.2). The systems which are simulated are isolated systems and therefore conservative. As such, the force is originated by a potential energy function (gradient of the potential):

$$\boldsymbol{F}_i = -\nabla_{\boldsymbol{r}_i} U(\boldsymbol{r}_1, ..., \boldsymbol{r}_N) \tag{2.8}$$

where U is the total potential energy coming from the interactions occurring between particles in the system. By introducing the interaction parameters which allow to calculate U at each timestep, the gradient of U and the integration of the equations of motion are sufficient to obtain the trajectories of the atoms.

The parameters of the potential are a part of the molecular model or force field, used to model the molecular system. The next section concerns this subject.

2.2.1 Force Field

The total potential energy of a system – $\mathscr{V}$ (from Eq. 2.2), or more commonly U – for a system of N particles is given by the sum of the potential energy associated to all interactions occurring in the system:

$$\begin{aligned} U(\boldsymbol{r}_1, \boldsymbol{r}_2, ..., \boldsymbol{r}_N) &= \sum_{i=1}^{N-1} \sum_{j>i}^{N} u_{ij}^{B} + u_{ij}^{NB} \\ &= \sum_{i=1}^{N-1} \sum_{j>i}^{N} u_{ij}^{bond} + u_{ij}^{angle} + u_{ij}^{dih} + u_{ij}^{LJ} + u_{ij}^{Coul} \end{aligned} \tag{2.9}$$

Site-Site interactions can be divided into two categories: bonded and non-bonded. The bonded interactions (u_{ij}^{B}) are associated to the interactions occurring between atoms within the same molecule and the non-bonded interactions (u_{ij}^{NB}) to the interactions between atoms of different molecules, or between different atoms of the same molecule that are distant by more than three bonds.
The bonded interactions comprehend the stretching of covalent bonds (u_{ij}^{bond}), the bending of valence angles (u_{ij}^{angle}) and the torsion around dihedral angles (u_{ij}^{dih}). The non-bonded interactions have contributions from van der Waals and electrostatic interactions, represented by Lennard-Jones (u_{ij}^{LJ}) and Coulombic (u_{ij}^{Coul}) potentials, respectively. The LJ and Coulombic interactions between atoms that are 1–4 bonded, i.e., that correspond to the two outermost atoms in a dihedral, also contribute to the non-bonded term. However, these interactions are scaled by a factor, to prevent their contribution from overwhelming the torsional interaction.

A scheme of these different interactions can be seen in Figure 2.3. The total expression for the energy is given in Eq. 2.10.

$$
\begin{aligned}
U(\boldsymbol{r}_1, \boldsymbol{r}_2, ..., \boldsymbol{r}_N) &= \sum_{ij}^{\text{bonds}} \frac{k_{r,ij}}{2}(r_{ij} \quad r_{0,ij})^2 + \sum_{ijk}^{\text{angles}} \frac{k_{\theta,ijk}}{2}(\theta_{ijk} \quad \theta_{0,ijk})^2 \\
&+ \sum_{ijkl}^{\text{dihedrals}} \sum_{n=1}^{3} \frac{V_{n,ijkl}}{2}[1 + (\quad 1)^{n+1} cos(n\varphi_{ijkl})] \\
&+ \sum_{i}^{non} \sum_{j \neq i}^{bonded} \left\{ 4\varepsilon_{ij} \left[\left(\frac{\sigma_{ij}}{r_{ij}} \right)^{12} \quad \left(\frac{\sigma_{ij}}{r_{ij}} \right)^{6} \right] + \frac{1}{4\pi\varepsilon_0} \frac{q_i q_j}{r_{ij}} \right\}
\end{aligned}
\tag{2.10}
$$

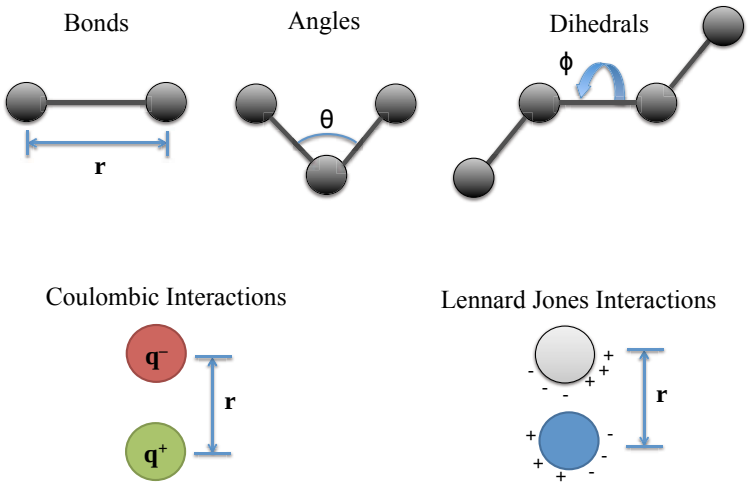

Figure 2.3: Type of possible interactions in the liquid phase.

In Equation 2.10, in the expressions corresponding to bonded interactions, i.e. u_{bond}, u_{angle} and u_{dih}, k_r and k_θ represent the harmonic force constants for bond stretching and angle bending; r_0 and θ_0 are the equilibrium distance and angle and V_n is the dihedral constant.

In the Lennard-Jones potential (u_{ij}^{LJ}), there are two distinct terms: $1/(r_{ij})^{12}$ and $1/(r_{ij})^6$, corresponding to repulsive and attractive interactions, respectively. The constant ε_{ij} is the potential well depth, and σ_{ij} the LJ core diameter. These two parameters are calculated using the geometric combining rules:

$$\varepsilon_{ij} = \sqrt{\varepsilon_i \varepsilon_j} \tag{2.11}$$

$$\sigma_{ij} = \sqrt{\sigma_i \sigma_j} \tag{2.12}$$

In the Coulombic contribution to the potential energy of the system (u_{ij}^{coul}), the constant ε_0 is the vacuum permittivity ($8.854 \times 10^{-12} F \cdot m^{-1}$) and the term $1/r_{ij}$ is related to the long-range character of the electrostatic interactions between the charges in the liquid. A long-range force is often defined as one in which the spatial interaction falls off no faster than r^{-d}, where d is the dimensionality of the system. When the potential is short ranged, the *minimum image convention*, in which each individual particle in the simulation interacts with the closest periodic image of the remaining particles in the system, is a good approximation for the interaction between the particles. However, for long range potentials this approximation is not sufficient because the energy of interaction decreases very slowly so that we cannot limit the interaction to the size of the simulation box. To tackle this problem, the electrostatic interactions in a MD simulation are handled through the *Ewald summation technique*, or simply *Ewald sum*, a method that sums the interactions between an ion and all its periodic images. In the *Ewald sum*, the coulombic potential is separated into two terms, a short range term accounting for the interactions occurring in *real space*; and a long range term for the interactions occurring in *reciprocal space*.

Consider N molecules in a volume $V = L_x L_y L_z$, with center of mass $\boldsymbol{r_i}$, and composed of a particles with charge q_{ia} at a position r_{ia}. The electrostatic potential energy in the *Ewald Sum* method for a box with orthogonal axes is written as:

$$
\begin{aligned}
u_{coul} &= \frac{1}{2\varepsilon_0}\sum_{k\neq 0} Q(h)\; S(\boldsymbol{h})\; S(-\boldsymbol{h}) \\
&+ \frac{1}{8\pi\varepsilon_0}\sum_i\sum_a\sum_{j\neq i}\frac{q_{ia}q_{jb}}{r_{iajb}}\,\mathrm{erfc}(\alpha r_{iajb}) \\
&- \frac{\alpha}{4\pi^{3/2}\varepsilon_0}\sum_i\sum_a q_{ia}^2 \\
&- \frac{\alpha}{8\pi\varepsilon_0}\sum_i\sum_a\sum_{b\neq a}\frac{q_{ia}q_{jb}}{r_{iajb}}\,\mathrm{erf}(\alpha r_{iajb})
\end{aligned}
\tag{2.13}
$$

where erfc(x) is the complementary error function; erf(x) is the error function and α is the convergence parameter. The functions $S(\mathbf{h})$ and $Q(h)$ are defined using the following equations:

$$
S(\boldsymbol{h}) = \sum_i\sum_a q_{ia}\,\exp(i\boldsymbol{h}\cdot\boldsymbol{r_{ia}}) \tag{2.14}
$$

$$
Q(h) = \frac{1}{h^2}\exp\left(-\frac{h^2}{4\alpha^2}\right) \tag{2.15}
$$

where the reciprocal lattice vector **h** is defined as

$$
\boldsymbol{h} = 2\pi\left(\frac{l}{L_x},\frac{m}{L_y},\frac{n}{L_z}\right) \tag{2.16}
$$

where l, m, n take values of 0, ±1, ±2, ... ,$\pm\infty$. For further explanations on this subject consult the book *Computer Simulation of Liquids*[69], of Allen and Tildesley.

The parameters of the force field (Eq. 2.10) are determined by first principles and then adjusted over experimental properties. There are generalized forms of the force field, like for example the OPLS-AA[71] (Optimized Potential for Liquid Simulations-All Atom) force field, with large parameter sets that represent different classes of organic molecules.

In the present work, the parameters of the force field corresponding to the liquid-liquid interactions were specifically parametrized for the ionic liquids in this study, and the model used is compatible with the OPLS-AA framework. Both adopt the same kind of functional form, represented in Equation 2.10. The sole difference between Eq. 2.10 and the functional form of OPLS-AA is that the values of harmonic force constants for bond stretching and angle bending in the latter correspond to k/2 in Eq. 2.10. Therefore, constants for bond stretching and angle bending which will be presented in this work must be divided by two to obtain true OPLS-AA values. The force field parameters used in this work, for the liquid-liquid interactions, will be presented in section 3.2.1.

2.3 Non-Equilibrium Molecular Dynamics

In this thesis, MD is used at equilibrium and in non-equilibrium. Non-equilibrium molecular dynamics (NEMD) is an efficient technique to obtain transport coefficients, like viscosity, thermal conductivity, and mobility of molecular systems. Furthermore, it's a technique widely used in the last decade, to study tribological systems[9].

The principle behind NEMD is to introduce an external field to the system, and to measure the response of the system to such perturbation, over time. If sufficient time is available, the system will tend towards a non-equilibrium steady state (as long as the external field is constant over time). In the particular case of this work, a shear flow will be applied in the x-direction (by imposing a certain shear velocity), to each fixed molecule of a surface, generating a velocity profile of the particles in the fluid. The perturbations will appear in the equations of motion refered in Eq. 2.6 as follows:

$$\frac{d\boldsymbol{r_i}(t)}{dt} = \boldsymbol{v_i}(t) + \mathscr{A}_p \cdot \boldsymbol{F}(t) \tag{2.17}$$

$$\frac{d\boldsymbol{v_i}(t)}{dt} = \frac{\boldsymbol{F_i}(t)}{m_i} - \mathscr{A}_q \cdot \boldsymbol{F}(t) \tag{2.18}$$

where $\boldsymbol{F}(t)$ is a vector representing the time-dependent external field being applied to each molecule, in each coordinate direction, separately. The quantities $\mathscr{A}_p$ and $\mathscr{A}_q$ are both a function of the particles momenta and position. In the same manner, the Hamiltonian of the system will have an additional term accounting for this perturbation:

$$\mathscr{H}^{NE} = \mathscr{H} + \mathscr{A}(q,p) \cdot \boldsymbol{F}(t) \tag{2.19}$$

where in the case of this work, F is the instantaneous shear rate, i.e. $F = (dv_x/dr_y)$.
In the present work, the simulations in non-equilibrium are performed with different values of shear rate. Furthermore, the system is also under a certain load. The details are presented in section 5.2.2.

CHAPTER 3

Bulk Properties of Ammonium Ionic liquids

3.1 Scope of the Chapter

In the present chapter, structural and dynamic properties of the bulk ionic liquids will be analyzed. Firstly, the available experimental physical properties for the novel structures presented in this work will exposed. Then, MD simulation results on the liquid structure will be discussed with the help of site-site radial distribution functions, focusing on the impact of the alkyl side chain length. By analyzing the mean-square displacement profiles as a function of time, we were able to determine the self-diffusion coefficients for the ions in the ionic compounds and to relate that with their molecular structure.

3.2 Methods

3.2.1 Force Field Description

For the ionic liquids in this work, which are based in alkyl-ammonium cations combined with alkyl-sulfonate or bistriflamide anions (Figure 1.8), ion-ion interactions were represented by an all-atom

molecular force field based on the OPLS-AA model[71;72], specifically parameterized for the ionic liquids studied in this work. The functional form of the force field is given in Eq. 3.1. It contains four kinds of potential energy: stretching of covalent bonds, bending of valence angles, torsion around dihedral angles, and nonbonded interactions. Nonbonded interactions are active between atoms of the same molecule separated by more than three bonds and between atoms of different molecules. Bonds and angles were treated with an harmonic potential, and torsion angles with a series of cosines that fits the torsion energy profiles. Nonbonded interactions are described by a Lennard-Jones and a Coulomb potential, which represent dispersion-repulsion and electrostatic interactions, respectively. A complete description of the MD principles, the potential form used, and each one of the interaction terms in the potential, is given in Chapter 2.

$$
\begin{aligned}
U &= \sum_{ij}^{\text{bonds}} \frac{k_{r,ij}}{2}\left(r_{ij}-r_{0,ij}\right)^2 + \sum_{ijk}^{\text{angles}} \frac{k_{\theta,ijk}}{2}\left(\theta_{ijk}-\theta_{0,ijk}\right)^2 \\
&+ \sum_{ijkl}^{\text{dihedrals}} \sum_{n=1}^{3} \frac{V_{n,ijkl}}{2}\left[1+(-1)^{n+1}\cos(n\varphi_{ijkl})\right] \\
&+ \sum_{i}^{non-bonded} \sum_{j\neq i} \left\{ 4\varepsilon_{ij}\left[\left(\frac{\sigma_{ij}}{r_{ij}}\right)^{12} - \left(\frac{\sigma_{ij}}{r_{ij}}\right)^{6}\right] + \frac{1}{4\pi\varepsilon_0}\frac{q_i q_j}{r_{ij}} \right\}
\end{aligned}
\tag{3.1}
$$

The intramolecular parameters that describe bonds, angles and dihedrals and the intermolecular parameters for the Lennard-Jones and Coulombic interactions are presented in Tables 3.1, 3.2 and 3.3. Nomenclature adopted for the interaction sites in the ionic liquids is represented in Figure 3.1. Note that atoms C1, C2, CS, CT and CS3 are all equivalent in terms of bonds, angles and dihedrals, having only different electrostatic charges. Therefore, for simplicity they will be all be named CT for the purpose of the intramolecular parameters. The same happens to H1, HC and HS3 which will be all named HC in bonds, angles and dihedrals. The other atoms maintain their nomenclatures. Bonds lengths of all C–H stretching modes were constrained, in both cation and anion.

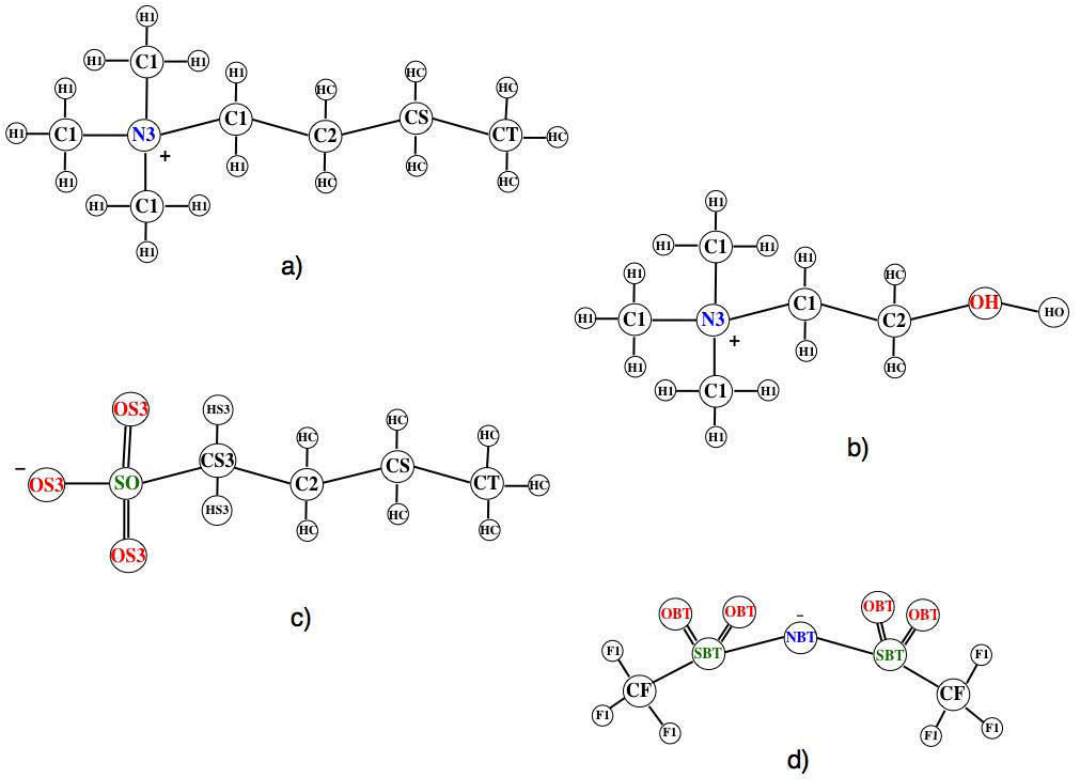

Figure 3.1: Nomenclature adopted for the interaction sites in a) 1-butyl-1,1,1-methylammonium cation (N^+_{1114}); b) cholinium cation (N^+_{112OH}); c) alkylsulfonate anion ($R_1SO^-_3$) and d) bistriflamide anion (NTf^-_2).

Table 3.1: Force-Field Parameters for Ionic Liquids containing tetralkyl-ammonium ions. Atomic partial charges from[73], Lennard-Jones, bonds, angles and dihedrals parameters taken from[72;74–76]. Parameters for the sites OH and HO (for the choline) are the same than for the OPLS-AA force field for alcohols[75].

atoms	q	ε	σ	**bonds**	r_0	k_r
	e	kJ·mol^{-1}	Å		Å	kJ·mol^{-1}
N3	+0.12	3.25	0.71128	N3–CT	1.471	3071
C1	–0.17	3.50	0.27614	CT–CT	1.529	2242
H1	+0.13	2.50	0.12552	CT–HC	1.090	(constrained)
C2	+0.01	3.50	0.27614	CT–OH	1.410	2678
CS	–0.12	3.50	0.27614	HO–OH	0.945	(constrained)
CT	–0.18	3.50	0.27614			
HC	+0.06	2.50	0.12552			
OH	–0.683	3.21	0.71128			
HO	0.418	0.00	0.00000			

dihedrals	V_1	V_2	V_3	**angles**	θ_0	k_θ
	kJ·mol^{-1}	kJ·mol^{-1}	kJ·mol^{-1}		deg	kJ·mol^{-1} rad $^{-2}$
HC–CT–CT–N3	–4.2384	–2.9665	1.9790	N3–CT–CT	109.5	669.4
CT–CT–CT–N3	10.0081	–2.8200	2.3012	CT–N3–CT	109.5	418.4
CT–N3–CT–CT	1.7405	–0.5356	2.9079	HC–CT–N3	109.5	209.2
HC–CT–N3–CT	0.0000	0.0000	2.3430	HC–N3–CT	109.5	418.4
HC–N3–CT–HC	0.0000	0.0000	0.0000	CT–CT–CT	112.7	488.3
HC–N3–CT–CT	0.0000	0.0000	0.0000	CT–CT–HC	110.7	313.8
HC–CT–CT–HC	0.0000	0.0000	1.3305	HC–CT–HC	107.8	276.1
CT–CT–CT–HC	0.0000	0.0000	1.5313	CT–CT–OH	109.50	418.40
CT–CT–CT–CT	7.2800	–0.6569	1.1673	HC–CT–OH	109.50	292.88
N3–CT–CT–OH	0.0000	0.0000	0.0000	CT–OH–HO	108.50	460.24

Table 3.2: Force-Field Parameters for Ionic Liquids containing Alkyl–Sulfonate ions. Parameters for the alkyl side chains can be found in Table 3.1. Parameters of interaction for the sulfonate sites were taken from[77].

atoms	q	ε	σ	**bonds**	r_0	k_r
	e	kJ·mol^{-1}	Å		Å	kJ·mol^{-1}
SO	+1.18	3.55	1.04600	CT–SO	1.792	1970
OS3	–0.68	3.15	0.83700	OS3–SO	1.455	5331
CS3	–0.14	3.50	0.27600			
HS3	0.00	2.50	0.12600			
dihedrals	$\mathbf{V_1}$	$\mathbf{V_2}$	$\mathbf{V_3}$	**angles**	θ_0	k_θ
	kJ·mol^{-1}	kJ·mol^{-1}	kJ·mol^{-1}		deg	kJ·mol^{-1} rad^{-2}
OS3–SO–CT–HC	0.0000	0.0000	1.6250	OS3–SO–OS3	114.00	969.00
OS3–SO–CT–CT	0.0000	0.0000	1.3938	CT–SO–OS3	104.50	870.00
SO–CT–CT–HC	0.0000	0.0000	1.3797	HC–CT–SO	107.30	390.30
SO–CT–CT–CT	–16.1000	–2.0046	0.7674	CT–CT–SO	113.30	583.00

Table 3.3: Force-Field Parameters for Ionic Liquids containing ions bistriflamide. Paramteres of interaction taken from [73].

atoms	q	ε	σ	**bonds**	r_0	k_r
	e	kJ·mol^{-1}	Å		Å	kJ·mol^{-1}
F1	–0.16	2.95	0.22175	F1–CF	1.332	3071.06
CF	+0.35	3.50	0.27614	CF–SBT	1.818	1950.00
SBT	+1.02	3.55	1.04600	SBT–OBT	1.437	5331.00
OBT	–0.53	2.96	0.87864	NBT–SBT	1.570	3137.00
NBT	–0.66	3.25	0.71128			
dihedrals	$\mathbf{V_1}$	$\mathbf{V_2}$	$\mathbf{V_3}$	**angles**	θ_0	k_θ
	kJ·mol^{-1}	kJ·mol^{-1}	kJ·mol^{-1}		deg	kJ·mol^{-1} rad^{-2}
OBT–SBT–CF–F1	0.0000	0.0000	1.4510	F1–CF–F1	109.10	644.34
NBT–SBT–CF–F1	0.0000	0.0000	1.3220	F1–CF–SBT	111.7	694.00
OBT–SBT–NBT–SBT	0.0000	0.0000	−0.0150	OBT–SBT–OBT	118.5	969.00
SBT–NBT–SBT–CF	32.7730	−10.4200	−3.1950	CF–SBT–OBT	102.6	870.00
				NBT–SBT–OBT	13.6	789
				NBT–SBT–CF	103.5	764
				SBT–NBT–SBT	125.6	671

3.2.2 Simulation Conditions

Two hundred ion pairs of the different ionic liquid were simulated in cubic boxes, at 373 K and 500 K, with the molecular dynamics simulation program DL_POLY[78]. The initial configuration was a low-density lattice which was equilibrated at constant pressure (1 atm) with a timestep of 1 fs in order to reach the correct density of the bulk liquid. Once an equilibrated liquid was obtained, a simulation run of 2 ns was executed with a time step of 2 fs, at constant NpT regulated by the Nosé–Hoover thermostat and barostat algorithm. Long-range electrostatic interactions were handled through the Ewald summation technique, using a real-space cut-off of 16 Å. The number of wave-vectors considered in the reciprocal space were $k_x = k_y = k_z = 4$, yielding a relative accuracy better than 0.001 in the calculation of the electrostatic energy. Configurations from the production runs were stored every 500 time steps. These configurations contain coordinates, the components of velocity and force vectors.

The ammonium-based ionic liquids studied in this section are the following: 1-butyl-1,1,1-trimethylammonium metane sulfonate ($[N_{1114}][C_1SO_3]$), 1-butyl-1,1,1-trimethylammonium butanesulfonate ($[N_{1114}][C_4SO_3]$), 1-butyl-1,1,1-trimethylammonium octylsulfonate ($[N_{1114}][C_8SO_3]$) and 1-butyl-1,1,1-trimethylammonium bis(trifluoromethylsulfonyl)imide (or bistriflamide) ($[N_{1114}][NTf_2]$). Their chemical structures are given in Figure 1.8.

3.2.3 Structural Correlation Analysis

A function that characterizes the local structure of a fluid is the so-called radial distribution function $g(r)$. This function gives the probability of finding a pair of atoms at a given distance r, relative to that same probability in a completely random distribution at the same density (Eq. 3.2) . When the distance r between the two atoms becomes large, the probability of correlation falls to that of a random, isotropic liquid and $g(r)$ becomes 1.

$$g(r) = \frac{\rho(r)}{\langle\rho\rangle} \tag{3.2}$$

The $g(r)$ of ionic liquids is quite particular, due to charge ordering. Figure 3.2 presents the radial distribution for $[N_{1114}][C_4SO_3]$, but a similar profile can be found in almost all ionic liquid. There is an alternation between shells of cations and anions (charge and counter-charge), being the 1^{st} peak of the radial distribution function associated to the cation–anion first-neighbor correlations, followed by the cation–cation and anion–anion distance probabilities (2^{nd} and 3^{rd} peaks, respectively), which are in opposition of phase with counter-ion correlation distances.

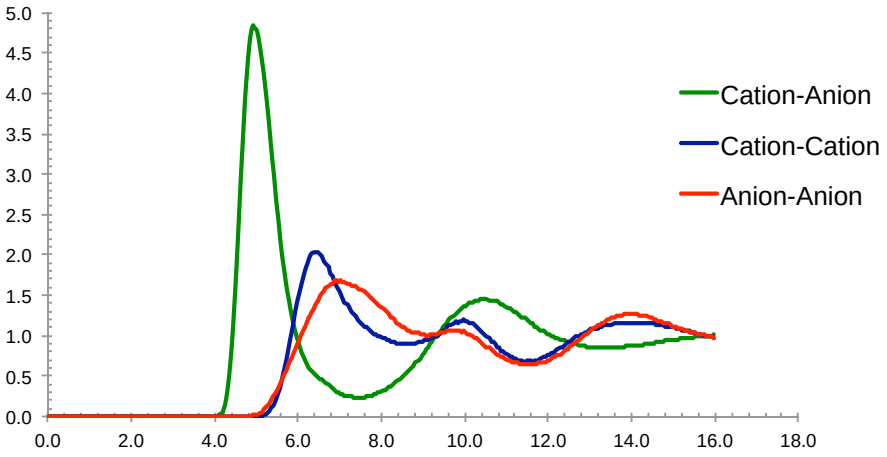

Figure 3.2: Radial distribution function – $g(r)$ – of an ionic liquid.

The pair distribution function is useful not only because it provides insights about the liquid structure, but also because it can be related to macroscopic thermodynamic quantities such as energy, pressure and chemical potential.

3.2.4 Time Correlation Functions

The structural properties mentioned previously do not depend on the time evolution of the system. However, in a molecular dynamics simulation at equilibrium, besides static equilibrium properties, dynamic properties can also be measured. The time-dependent property investigated here is diffusion.

Diffusion is caused by the molecular motion of the particles in the fluid, down a concentration gradient. The macroscopic law that describes diffusion is the Fick's law, however, in the present case, because the displacement of species is done without a concentration gradient, what we measure corresponds to the self-diffusion coefficient.

In computer simulations, transport coefficients like diffusion or viscosity can be calculated through the time integral of an equilibrium time correlation function of this form:

$$\gamma = \int_0^\infty \langle \dot{\mathscr{A}}(t) \cdot \dot{\mathscr{A}}(0) \rangle dt \tag{3.3}$$

where γ is the transport coefficient and A the associated variable. Correlated to any expression of this kind (by performing integration by parts to Eq. 3.3), there is an Einstein relation, which is valid at large values of t:

$$2t\gamma \;=\; \langle \Delta |A(t)|^2 \rangle \;=\; \langle (A(t) – A(0))^2 \rangle \tag{3.4}$$

The self-diffusion coefficient (in three dimensions) can be calculated through:

$$D = \frac{1}{3} \int_0^\infty \langle v_i(t) \cdot v_i(0) \rangle dt \tag{3.5}$$

where $v_i(t)$ is the velocity of the center of mass of molecule i. Such a relation between a transport coefficient and an integral over a time-correlation is called a *Green-Kubo* relation.

The corresponding Einstein relation is:

$$2tD = \frac{1}{3}\langle |r_i(t) – r_i(0)|^2 \rangle \tag{3.6}$$

where $r_i(t)$ is the position of the molecule center of mass. Thus, the self-diffusion coefficient may be estimated by observing the quantity in brackets $\langle |r_i(t) – r_i(0)|^2 \rangle$ which is called mean-square displacement (MSD), as a function of time. The Einstein relation is by far the most commonly used to calculate D.

For a correct estimation of the self-diffusion coefficient, the liquid has to be in a "real" diffusive regime. To characterize the dynamic nature of a liquid, the way in which the mean-square displacement scales with time is examined. This can be quantified as[79]:

$$\text{MSD} \propto \text{t}^{\beta} \tag{3.7}$$

where β characterizes the type of motion present in the system, which can be ballistic ($\beta = 2$), subdiffusive ($\beta < 1$) or diffusive ($\beta = 1$). By applying logarithms to each sides of Eq. 3.7, the quantity β can be obtained as :

$$\beta(t) = \frac{d\log(\Delta r^2)}{d\log(t)} \tag{3.8}$$

Therefore, by plotting the β as a function of time one can determine which dynamic regime a system is in.

A typical MSD graph for a Lennard-Jones Fluid is represented in Figure 3.3 with the respective regimes pointed in the figure. At very short times, a ballistic motion dominates. This regime is characterized by the"free flight" of the particles in the fluid. If the molecule encountered no other molecules she would travel ballistically and the distance traveled would increase quadratically with time. However, in dense phases quadratic behavior only holds for a few picoseconds, before the particles collides. After a while, the motion becomes diffusive and the MSD curve will increase linearly with time.

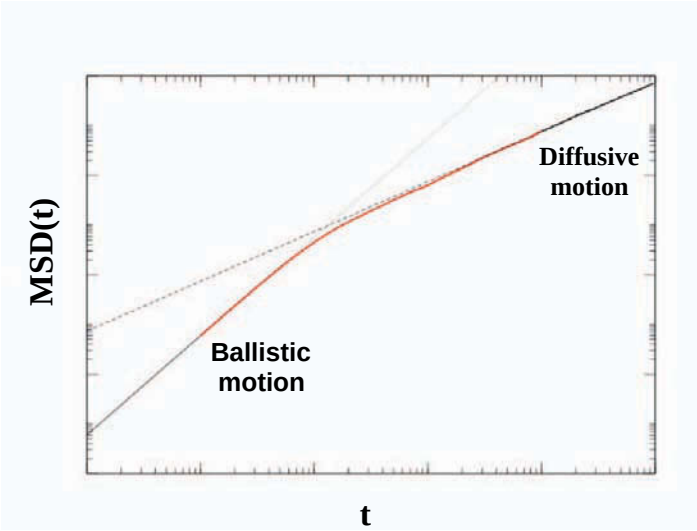

Figure 3.3: Mean-Square displacement profile of a Lennard-Jones fluid. Ballistic and diffusive regimes are represented in the graph.

At large values of t, the MSD increases linearly with time and, from Eq. 3.6

$$D = \frac{1}{6} \lim_{t\to\infty} \frac{d}{dt} \left\langle |r_i(t) - r_i(0)|^2 \right\rangle \tag{3.9}$$

In this linear regime, the slope of the curve will give, by the Einstein relation presented in Eq. 3.9,

the self-diffusion coefficient. In the sub-diffuse regime (at intermediate t), molecules of the liquid have cage-like dynamics, colliding with their near neighbors and thus loosing velocity and position correlation, but still not attaining true diffusion. Such behavior is present in supercooled liquids, in ionic liquids and other glass-forming liquids.

In Eq.3.5 the quantity $\langle v_i(t) \cdot v_i(0) \rangle$ is the so called velocity auto-correlation function (VACF) and it measures the correlation between the velocity of particles at different times, along an equilibrium trajectory. Calculating the VACF is another way to measure D by molecular simulations, although here we will use the MSD graphs to extract this transport property. However, the two approaches are thought to give identical values of D.

3.3 Results and Discussion

3.3.1 Physical Properties of the Novel Ammonium-Based Ionic Liquids

The present thesis is included in a multidisciplinary network the objective of which is to study ammonium based ionic liquids as "environmentally friendly" substances for potential application in the lubrication industry (section 1.1). The ionic liquid's structures presented here are novel structures (see Figure 1.8), therefore in most cases their physical properties are not yet measured experimentally. Our role in the network is to give insights about the structure and interactions of these ionic liquids in contact with metallic surfaces and the role of the other network partners is diverse, but includes providing properties for the chosen structures. Table 3.4 summarizes the available physical properties, measured by partners within the network, and it includes mass (m), melting point (T_{fus}), density (ρ) and viscosity (η).

Ionic liquids have a slow dynamics and long simulations are necessary to obtain accurate atoms trajectories necessary to measure important properties in the liquid and at the interface. Therefore, it becomes impossible to simulate all the structures present in Table 3.4 in a 3-years period, the time of a PhD thesis. For this, the present work will focus on the following ionic liquids: $[N_{1114}][NTf_2]$, $[N_{1114}][C_1SO_3]$, $[N_{1114}][C_4SO_3]$, $[N_{1124}][C_4SO_3]$ and $[N_{1114}][C_8SO_3]$.

Table 3.4: Measured physical properties for the ionic liquids within the network MINILUBES, by other partners in the consortium. Mass (m), melting point (T_{fus}), density (ρ) and viscosity (η) are part of the available data.

Cation	**Anion**	**MW**	T_{fus}	ρ	η
		g· mol^{-1}	°C	g · cm^{-3}	mPa · s
N_{1112OH}	NTf_2	384	36	1.461 (100°C)	11.51 (100°C)
N_{1112OH}	C_1SO_3	199	110	——	——
N_{1122OH}([80])	C_4SO_3	255	44	1.112 (25°C)	1354 (25°C)
N_{1112O1}	NTf_2	398	44	——	——
N_{1112O1}	C_1SO_4	229	45	——	——
N_{1112O1}	C_1SO_3	213	63		
N_{1114}	NTf_2	396	19	1.329 (100°C)	9.350 (100°C)
N_{1444}	C_1SO_3	295	80	0.979 (100°C)	48.54 (100°C)
N_{1114}([80])	C_1SO_3	211	169	——	——
N_{1114}([80])	C_4SO_3	253	62	——	——
N_{1124}	C_4SO_3	282	80	0.997 (100°C)	60.29 (100°C)
N_{1114}([80])	C_8SO_3	310	211	——	——
N_{1222}([81])	C_1SO_4	227	25	1.145 (70°C)	44.92 (70°C)
N_{1224}([81])	C_2SO_4	255	34	1.208 (25°C)	333.2 (25°C)

3.3.2 Liquid Structure

To obtain insights into the organization of the liquid, several site-site radial distribution function's (RDFs) were computed for the following ammonium based ionic liquids: $[N_{1114}][C_4SO_3]$, $[N_{1114}][C_1SO_3]$, $[N_{1114}][C_8SO_3]$ and $[N_{1114}][NTf_2]$. The ionic liquid's structures and interaction site labels can be seen in Figure 3.4.

The discussion will start with the RDFs for the cation-anion, cation-cation and anion-anion interactions, for the first three structures which are based in the ammonium-sulfonate ionic liquids (Figure

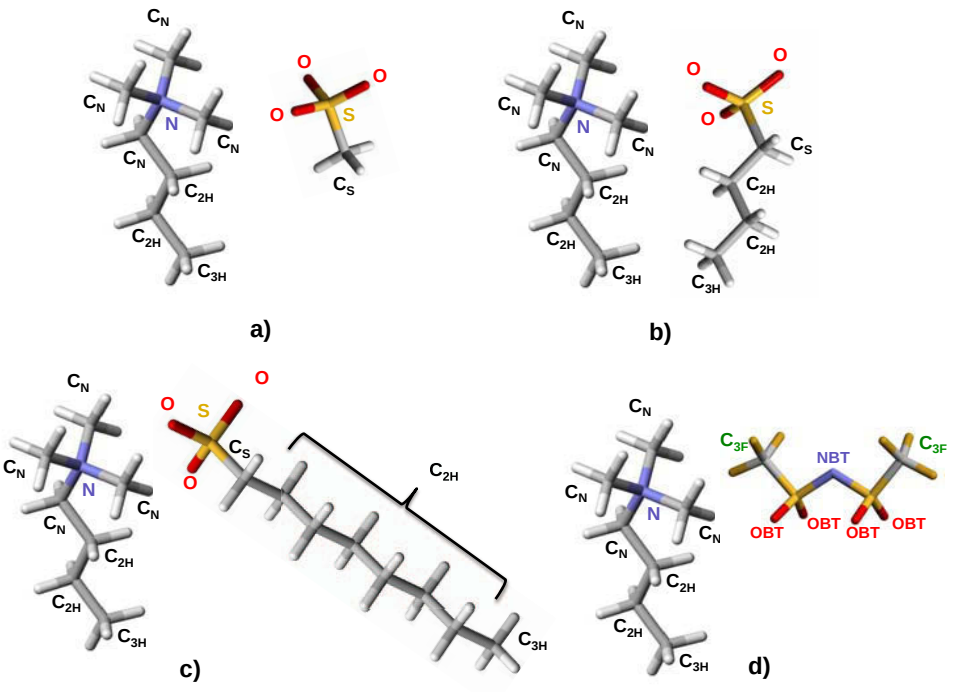

Figure 3.4: Molecular structures of the ammonium-based ionic liquid a) $[N_{1114}][C_1SO_3]$, b) $[N_{1114}][C_4SO_3]$, c) $[N_{1114}][C_8SO_3]$ and d) $[N_{1114}][NTf_2]$.

3.5). The N atom was chosen as the representative of the center-of-mass of the cation and in the case of the anion, the S atom.

In Figure 3.5, all ionic liquids exhibit a first cation-anion (CA) peak at $\sim$ 5 Å, followed by a cation-cation (CC) peak at $\sim$ 6.5 Å and finally an anion-anion (AA) peak, which has slightly different positions in each liquid. For example, in $[N_{1114}][C_4SO_3]$, the AA interaction peak is at 7.5 Å and in the ionic liquid $[N_{1114}][C_1SO_3]$, the same peak is at 7.0 Å. This is due to the fact that the anion alkyl side chain length in the former case is smaller, and therefore the anion-anion interaction will occur at a smaller r.

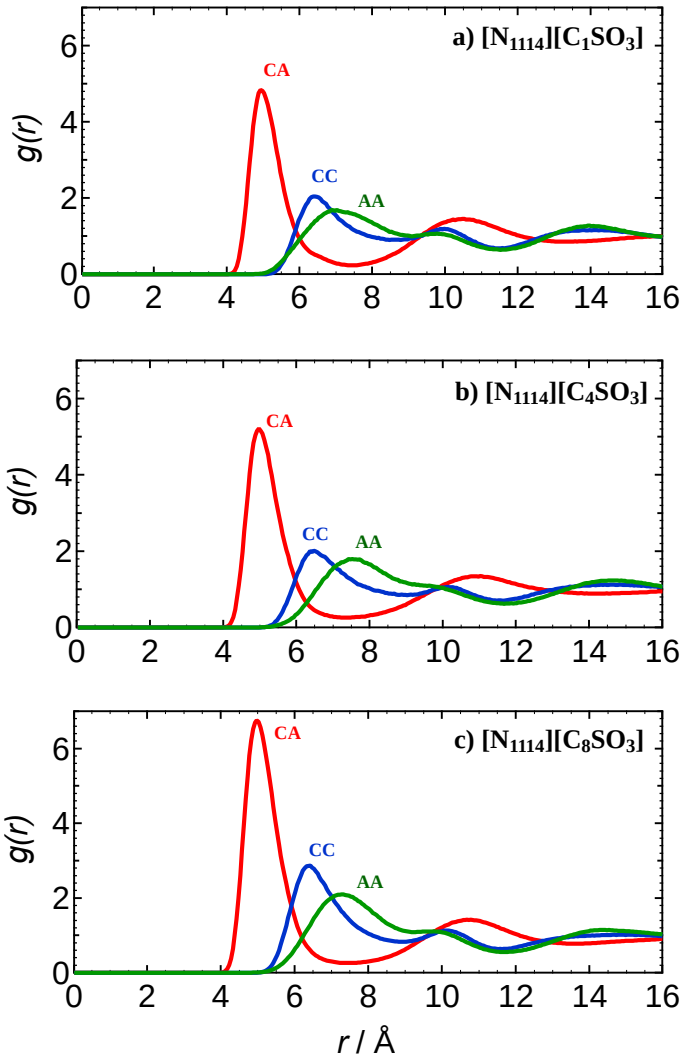

Figure 3.5: Radial distribution functions for the cation-anion (CA), cation-cation (CC) and anion-anion (AA) interactions in the ionic liquids a) $[N_{1114}][C_1SO_3]$, b) $[N_{1114}][C_4SO_3]$ and c) $[N_{1114}][C_8SO_3]$.

All systems exhibit long-range spatial correlations which extend beyond 16 Å, a characteristic of ionic liquids. The oscillations of CC and AA are out of phase with those of CA indicating a charge-ordering effect in which cations and anions are preferentially surrounded by their corresponding counter-ions, leading to the phenomenon of screening. Such behavior can be observed in the spatial distribution

functions (SDFs), plotted in Figure 3.6. SDFs can provide very useful visual insights into the spatial relations between different structural features of the ionic liquids. In the case plotted in Fig. 3.6, it gives the probability to find the SO_3^- group of the anion (yellow) around the $N(CH_3)_3$ group of the cation. The analysis of the SDFs shows a spherical symmetry of the first ionic coordination shell around the cation head group, which in fact corresponds to the spatial correlation functions between the oxygen atoms of the anion and the nitrogen atom of the cation. The spherical shell is only interrupted by the alkyl side chain in the cation.

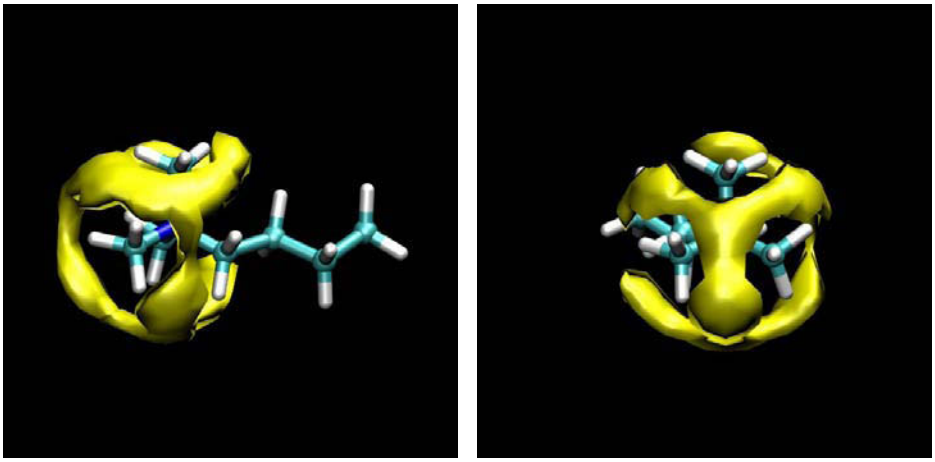

Figure 3.6: Spatial distribution functions for the probability to find the SO_3^- group around the $N(CH_3)_3$ group of the cation: frontal and lateral view.

Additional insights into the organization of this family of ionic liquids can be obtained by tracing the site-site RDFs between the terminal carbon atoms in the alkyl side chain. This method allows to analyze the clustering of the non-polar alkyl side chains into non-polar domains[23], which lead to the hypothesis of the existence of nanosegregated domains in ionic liquids[24;82]. The alkyl side chain length in the anion increases when passing from $[N_{1114}][C_1SO_3]$ to $[N_{1114}][C_8SO_3]$, therefore it can be interesting to check the correlation between end-carbons of the alkyl side chains. Figure 3.7 shows the site-site intermolecular RDFs for the C_{3H} C_S sites in $[N_{1114}][C_1SO_3]$ (blue) and for the C_{3H} C_{3H} sites in $[N_{1114}][C_4SO_3]$ (red) and $[N_{1114}][C_8SO_3]$ (green). All peaks are found ~ 4 Å, but the peaks become broader and less intense when the number of carbons in the alkyl side chain in the anion

increases from C_1 to C_8. Other MD studies with imidazolium based ionic liquids[23] and ammonium based ionic liquids[83] with increasing alkyl chain lengths in the cation, found an opposite behavior to the one found here. In those studies, the intensity of the main peaks increased with the alkyl chain length of the cation, indicating that the tendency to form segregated non-polar domains increased as the size of the non-polar moieties (alkyl side chain) became larger.

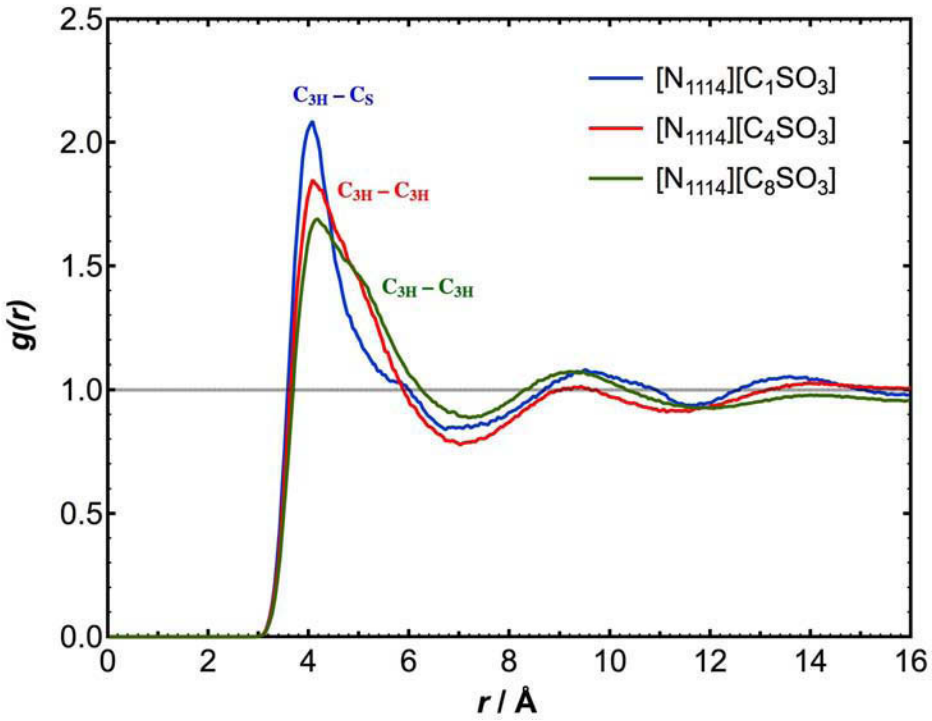

Figure 3.7: End-carbon to end-carbon RDFs for $[N_{1114}][C_1SO_3]$ ($C_{3H}-C_S$) and $[N_{1114}][C_4SO_3]$ and $[N_{1114}][C_8SO_3]$ ($C_{3H}-C_{3H}$).

Here, the high probability peaks at approximately 4 Å also indicate the presence of a strong interaction between the terminal carbons C_{3H} (or between C_{3H} and C_S). However, the fact that the peaks decrease intensity is most likely due to the additional conformational flexibility of the longer alkyl chains, causing these correlations to be more diffuse and extended into the solvation shell.

A simple way to visualize the polar and non-polar domains in the bulk ionic liquids is to use color-

coded snapshots of the simulation boxes. In Figure 3.8, both positive and negative parts of the ions were colored in red and the neutral (non-polar) side chains in green. In the positive part were included atoms N, C_N and the respective hydrogen atoms, from the cation specie. In the negative part, the O, S, C_S (and respective hydrogen atoms) from the anion were included. Finally, atoms C_{2H}, C_{3H} and respective hydrogens are part of the non-polar domain.

By observing the colored boxes, one can clearly identify that the regions denoted in green, representing the non-polar domains, increase with the lengthening of the alkyl side chain. The non-polar regions in $[N_{1114}][C_1SO_3]$ form islands in the middle of the polar regions, these last dominated by highly cohesive anion-cation interaction because the cation is quite small. On the other hand, in the simulation box of $[N_{1114}][C_8SO_3]$, the segregated alkyl chains form almost a continuous non-polar domain.

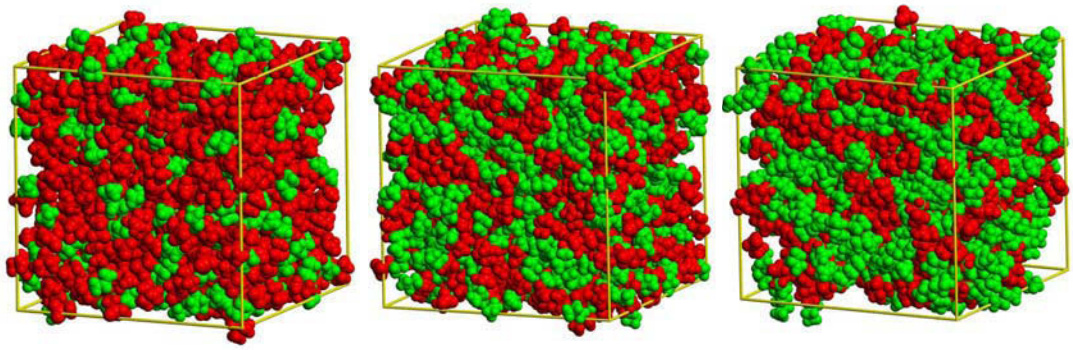

$[N_{1114}][C_1SO_3]$ **$[N_{1114}][C_4SO_3]$** **$[N_{1114}][C_8SO_3]$**

Figure 3.8: Polar and non-polar domains in simulation boxes containing ionic liquids $[N_{1114}][C_nSO_3]$ with $n = 1$, 4 and 8. The polar domain (red) correspond to the charged parts in the cation and anion and the non-polar domains (green) to the alkyl side chains in both ion species.

Another ionic liquid which is a part of the target structures in this work is $[N_{1114}][NTf_2]$. The size and nature of the anion can play an important role in the structure of the liquid and in particular, in the morphology of the polar/non-polar domains. The site-site RDFs for this ionic liquid can be seen in Figure 3.9 for the cation-anion (CA), cation-cation (CC) and anion-anion (AA) correlations. The N atom was chosen as the center-of-mass of the cation and it was correlated with several atoms in the

anion such as NBT, OBT and SBT.

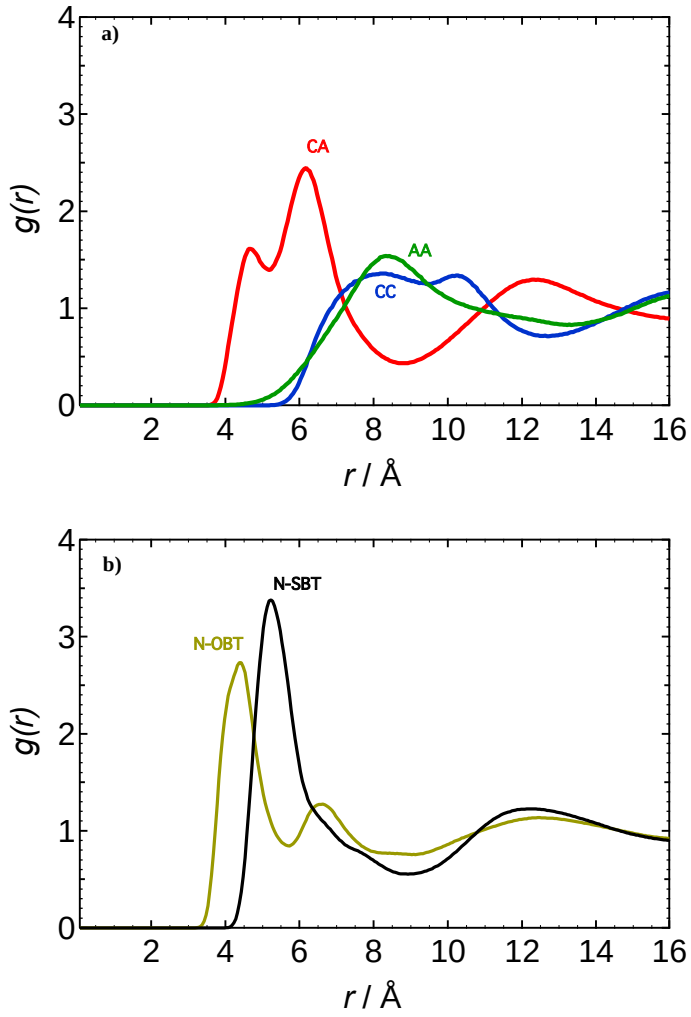

Figure 3.9: Radial distribution functions for: a) cation–anion (CA), cation–cation (CC) and anion–anion (AA) interaction; b) cation–oxygen atoms in the anion (N−OBT) and cation–sulfur atoms in the anion (N−SBT) interactions, in the ionic liquid $[N_{1114}][NTf_2]$.

Figure 3.9a shows that the correlation between the cation and the NBT atom in the anion only starts at ca. 4 Å, and that this interaction has two peaks of high probability density, one at 5 Å and the other one at 6 Å. Then, the AA and CC interactions occur at approximately the same distance r in

the solvation shell, i.e., $\sim$ 8 Å. When one looks to part b) of Figure 3.9, it can be seen that in fact the first coordination shell around the nitrogen atoms in the cation will correspond to the oxygen atoms in the anion bistriflamide (yellow curve). This is quite logic because the oxygen atoms are the most negative species in solution and they will tend to screen the positive charge coming from the cation head-group. This last interaction is also accompanied by some interaction with the NBT atoms, and that corresponds to the first peak in the CA curve of graph a), at ca. 4 Å. The sulfur atom in the anion (SBT) will interact at longer distances with N atoms and that is again accompanied by an interaction with the NBT atoms, at the origin of the 2nd peak in the CA curve of graph a), at ca. 5 Å. Finally, like in the amonium-sulfonate based compounds, there is a typical local charge-ordering arrangement in this ionic liquid, identified by the out-of-phase peaks.

3.3.3 Dynamic Properties

It is important to study the microscopic dynamic behavior of ionic liquids, in order to understand processes like their chemical reactivity, rheology, electrical conductivity and mass transfer. The mean square displacement (MSD) and the self-diffusion coefficient, which can be derived from observing the center-of-mass MSD behavior in function of time, measures the liquid dynamics. These principles were explained in section 3.2.4.

Figure 3.10 a) and b) presents the center-of-mass MSD curves as a function of time for the ions in the ionic liquid $[N_{1114}][C_1SO_3]$ at two different temperatures, 373 and 500 K. The respective $\log - \log$ plots of the MSD curves are presented in Fig. 3.10 c) and d). One can distinguish two behaviors in the MSD plots: at short times the displacement os the ions increases quadratically with time (ballistic motion) and at long times, after the molecules have experienced many collisions, the motion grows linearly with time. In order to evaluate if a diffusive regime is present at long values of t, the factor β was calculated in each one of the systems. The Einstein relation (Eq. 3.9), that allows measuring the self-diffusion coefficients, is only valid for systems in diffusive motion.

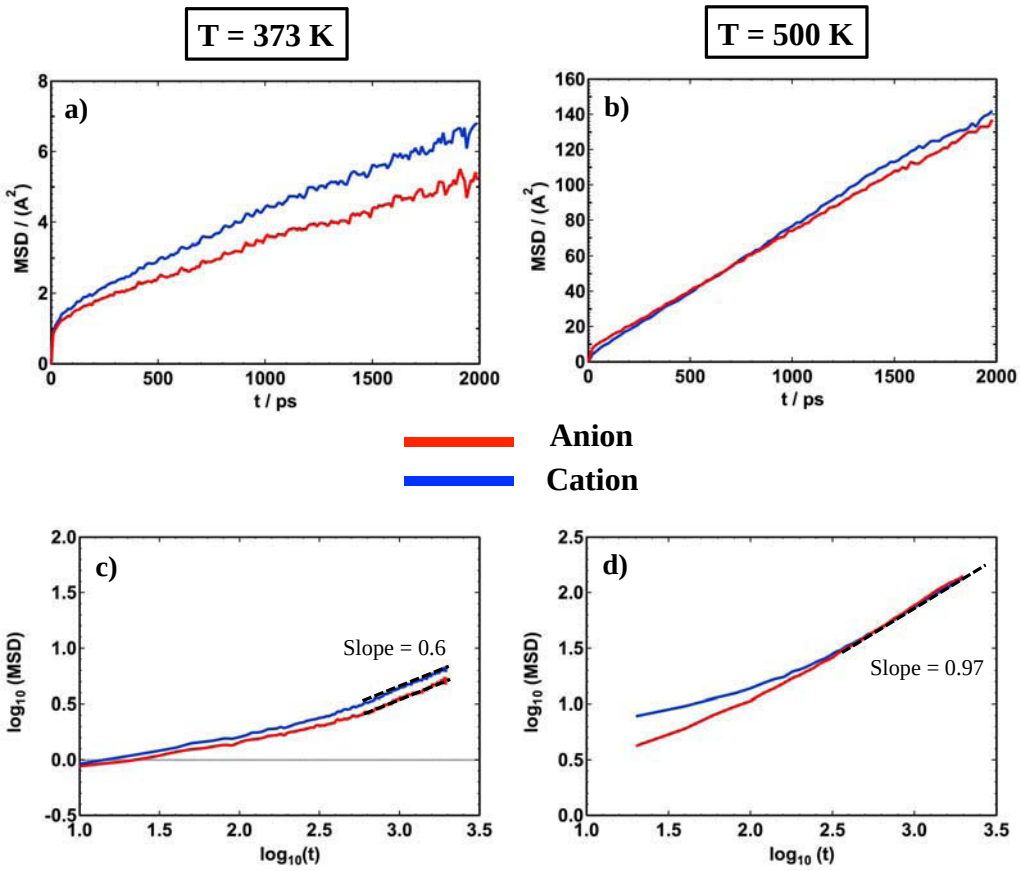

Figure 3.10: Mean square displacement profiles (MSD) in function of time and respective $\log - \log$ plots, for the cation (blue) and the anion (red) in the ionic liquid $[N_{1114}][C_1SO_3]$ at 373 K (for the a) and c) parts) and at 500 K (for the b) and d) parts). The slope values indicated in the figure correspond to the β parameter.

In the system at 373 K, it can be seen that β tends to a value of 0.6, meaning that the diffusive behavior is not really attained even after 2 ns of simulation. In the system at 500K, the diffusive behavior is approached with β having a value of 0.97. In order to see the evolution of the system's dynamics with time, the value of β was plotted in function of time, in Fig 3.11. It can be clearly seen that the diffusive regime ($\beta(t) = 1$) is obtained at long values of time. These results suggest that an accurate self-diffusivity cannot be determined at 373 K because the system exhibits a glassy dynamics at this temperature within the time of the simulation runs.

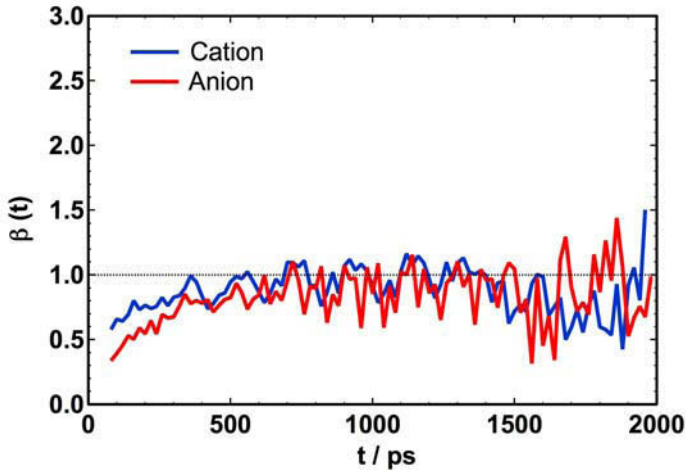

Figure 3.11: Evolution of the parameter β with time for the ionic liquid $[N_{1114}][C_1SO_3]$ at 500 K.

In table 3.5, a list of the computed self-diffusion coefficients for the anion and the cation species for the ionic liquids: $[N_{1114}][C_1SO_3]$, $[N_{1114}][C_4SO_3]$, $[N_{1114}][C_8SO_3]$ and $[N_{1114}][NTf_2]$ is presented. The self-diffusion coefficients were determined using Eq. 3.9.

Table 3.5: Self-diffusivities, β parameter and transport number parameters, for the ammonium based ionic liquids $[N_{1114}][C_1SO_3]$, $[N_{1114}][C_4SO_3]$, $[N_{1114}][C_8SO_3]$, and $[N_{1114}][NTf_2]$ at 373 and 500 K.

Ionic Liquid	β	D_{cation} $\times 10^{10}$ m$^2\cdot$ s^{-1}	D_{anion} $\times 10^{10}$ m$^2\cdot$ s^{-1}	t_+	t_-
$T = 373$ K					
$[N_{1114}][C_1SO_3]$	0.6	0.04	0.03	0.57	0.43
$T = 500$ K					
$[N_{1114}][C_1SO_3]$	0.97	1.23	1.07	0.53	0.47
$[N_{1114}][C_4SO_3]$	0.88	1.10	0.83	0.57	0.43
$[N_{1114}][C_8SO_3]$	0.78	0.78	0.48	0.62	0.38
$[N_{1114}][NTf_2]$	0.92	1.80	2.06	0.47	0.53

The values of D obtained by simulation are of the order of 10^{-10} m^2/s. The self-diffusivities of other ionic liquids based in pyridinium, imidazolium and ammonium cations with several anions including bistriflamide[84–86] range between 10^{-9} and 10^{-11} m^2/s. Although there are no experimental values for the ionic liquids $[N_{1114}][C_nSO_3]$, data is available for $[N_{1114}][NTf_2]$ at 303 K[87]: D_{cation}=1.7$\times 10^{-11}$ m^2/s and D_{anion}=1.4$\times 10^{-11}$ m^2/s. Our predicted values of D are higher than the ones obtained experimentally for this ionic liquid, however our study is performed at 500 K and as the temperature increases the self-diffusivities also increase, as it can be confirmed elsewhere[88]. In fact, several authors pointed to the fact that the self-diffusivities obtained by simulation tend to underestimate the experimental values for most cations and anions in an ionic liquid, of more or less 1 order of magnitude[84;86]. This is perceived as a consequence of using a non-polarizable force field (with static partial charges) that doesn't reproduce the high polarizability of the ions, responsible for a screening of the electrostatic interactions[89;90]. These, tend to restrict the motion of the ions and therefore the predicted dynamic properties are expected to be underestimated (in the case of diffusion) or overestimated (in the case of viscosity).

The general trend of the results obtained here is that the cations have a higher diffusivity than the anions, except for the ionic liquid with the NTf_2^- anion. In the ammonium-sulfonate ionic liquids, the fact that the anions have the negative charge distributed among the three oxygen atoms of the head-group, can induce some friction associated to the translational motion of these species. The cations, have the positive charge centered in the N atom, allowing an easier packaging with other ions and probably an easier diffusion. Furthermore, the increase of the alkyl side chain length in the anion decreases the diffusivity of both anion and cation species. An augmentation of the van der Waals interactions with other alkyl side chains can be at the origin of this diffusion reduction since the viscosity of the liquid increases. Despite this, the diffusion coefficients for the anions and cations are not very different, indicating a strong association of the counterions[91].

In the $[N_{1114}][NTf_2]$ ionic liquid, the molar volume of the anion is considerably higher than the one the cation, can be at the origin of the difference between their self-diffusivities. This ionic liquid has the highest self-diffusion values for the set of chosen structures, in agreement with its smaller viscosity.

For equimolar solutions, the relative contributions of the cations and anions to the total conductivity of the solution are characterized by transport numbers of the cation and anion. The transference numbers vary between 0 and 1 and are calculated by:

$$t_+ = \frac{D_{cation}}{D_{cation} + D_{anion}} \tag{3.10}$$

$$t_- = \frac{D_{anion}}{D_{cation} + D_{anion}} \tag{3.11}$$

The transport numbers are important in determining the behavior of the ionic liquids as electrolytes[91]. As presented in Table 3.5, the transport numbers for the cations in $[N_{1114}][C_nSO_3]$ are higher than the ones for the anions. In contrary, the anion in $[N_{1114}][NTf_2]$ has a higher transport number then the cation specie. A transport number higher then 0.5 indicates the ability of the ion to diffuse faster, and its stronger contribution to the ionic conductivity of the electrolyte.

3.4 Summary

MD results for the structural and dynamical properties of ionic liquids composed of ammonium cations and sulfonate or bistriflamide anions have been analyzed.

All systems exhibit long-range spatial correlations which extend beyond 16 Å. Charge-ordering is present in the bulk liquid, with the cations and anions preferentially surrounded by their corresponding counter-ions. RDFs between the terminal carbon atoms in the alkyl side chains of both ion species indicate the presence of segregation of the non-polar domains. This effect is emphasized when passing from C_1 to C_8, with the segregated alkyl chains forming a *quasi* continuous non-polar domain in this last case.

Self-diffusivities for the ionic liquid $[N_{1114}][C_1SO_3]$ were determined at 373 K and 500 K. The system at 373 K was found not to be in complete diffusive motion, but in a sub-diffusive regime. For the system at 500 K, a diffusive motion was attained at long values of time.The predicted self-diffusivities are of the order of 10^{-10} $m^2 \cdot s^{-1}$. It is known that the values predicted by simulation tend to underestimate the experimental ones, however in this case experimental data at this temperature is not available so that we can confirm such tendency.

The self-diffusion decreases with the increasing side chain length of the anion, in agreement with an increase in viscosity with the growth of the van der Waals interactions between the alkyl side chains. The ionic liquid with the anion bistriflamide was found to have the highest diffusivities, in accord to its lowest viscosity. Finally, it was seen that the difference between cation and anion self-diffusivities is not very significant and it is correlated, meaning that the ion–counter-ion association is strong.

CHAPTER 4

Ionic Liquids at Metallic Surfaces

4.1 Scope of the Chapter

In the present chapter, a force field developed specifically for the ionic liquids in this work interacting with a surface of iron will be described, based on quantum chemical calculations. Then, an analysis of the ordering and orientation of the ionic liquids at the metal surface will be presented, based on the molecular simulations results. The effect of the nature of the anion and the length of the alkyl side chain will be discussed.

We have chosen to build this model from first principles, due to the complexity linked to the iron–ionic liquid interactions. An intermolecular potential that describes liquid-metal interactions has to take into account not only van de Waals forces but also coulombic forces arising from polarization of the metal. Metal surfaces are conductive and highly polarizable, therefore when in contact with charged entities like ionic liquids, many-body interactions will occur that cannot be neglected. As such, the correct representation of the metal charge fluctuations is dependent of the nearby liquid structure, and the representation of the liquid structure itself, is also dependent on the metal polarizability.

4.2 Methods

4.2.1 Force Field Description

In systems composed by a solid and a liquid there are three types of interactions to take into account: liquid–liquid (IL–IL), solid–solid (M–M) and solid–liquid (M–IL), the last ones being the most complex to describe. The potential function of the system (U) will have contributions from all of these interactions:

$$U = U_{IL-IL} + U_{M-M} + U_{M-IL} \tag{4.1}$$

The complete functional form of the force field for the ionic liquid (U_{IL-IL}), which describes liquid-liquid interactions, is discussed in Chapter 2. These interactions were represented by an all-atom force field based on the OPLS-AA model, that was specifically parametrized for the ionic liquids present in this work. The parameters of interactions can be found in section 3.2.1 of this thesis.

For the interaction between atoms of the metal (U_{M-M}) a Finnis-Sinclair potential[92] was used, whith the following general form:

$$U_{M-M} = \frac{1}{2} \sum_{i=1}^{N_{metal}} \sum_{j \neq i}^{N_{metal}} V_{ij}(r_{ij}) + \sum_{i=1}^{N_{metal}} F(\rho_i) \tag{4.2}$$

where $V_{ij}(r_{ij})$ is a pair potential incorporating repulsive electrostatic and overlap interactions; N_{metal} is the number of metal atoms in the system and $F(\rho_i)$ is a functional describing the energy of embedding an atom at a given density, which is defined as:

$$\rho_i = \sum_{j=1, j \neq i}^{N_{metal}} \rho_{ij}(r_{ij}) \tag{4.3}$$

The Finnis-Sinclair potential is derived from quantum calculations and describes the bonding of metal atoms in terms of the local electronic density. The analytical form used here for this potential is given in Eq. 4.4. Parameters c_0, c_1, c_2, c, A, d, β for the bcc crystal structure were obtained from Watababe and Suzuki[93] and are presented in Table 4.1.

$$V_{ij} = (r_{ij} - c)^2(c_0 + c_1 r_{ij} + c_2 r_{ij}^2) \tag{4.4}$$

$$\rho_{ij}(r_{ij}) = (r_{ij} - d)^2 + \beta\frac{(r_{ij} - d)^3}{d}$$

$$F(\rho_i) = -A\sqrt{\rho_i}$$

Table 4.1: Iron-iron interaction parameters for Eq. 4.4[93].

c Å	c_0 kJ·mol^{-1}Å^{-2}	c_1 kJ·mol^{-1}Å^{-3}	c_2 kJ·mol^{-1}Å^{-4}	A kJ·mol^{-1}Å^{-1}	d Å	β
3.40	119.36	-34.66	-3.72	176.46	3.57	1.80

Finally, for the interaction between the ionic liquid and the metal atoms, an original model was developed based in first principles calculations. This model represents one of the main contributions of this thesis, since it opens the way for further studies on ionic liquids at metallic surfaces. The present model will include the polarization effect of electrostatically charged entities near a conducting surface, a contribution that is expected to be important for the systems studied here. Several molecular simulation studies of ionic liquids near conducting surfaces, such as metals or graphene-like surfaces, have been published, but most of them[57;94;95] totally omit these polarization terms and the results therefore may be far from reality.

The modeling of ions near metal or graphite electrodes using simpler representations (hard bodies point charges) shows that the inclusion of polarization is crucial in the reproduction of the metal charge fluctuations that depend on the nearby liquid structure[55;96]. Also, the ordering of the liquid layer will have great influence in the polarization of the metal surface. MD studies involving ionic liquids confined between graphite electrodes showed the importance of taking into account the polarization of the electrode by the ions (rather than assuming a constant electrode charge) in the interfacial structure and differential capacitance of the ionic liquid[97;98]. Further studies focusing in the application of ionic liquids in the build-up of supercapacitors, also showed the influence of the ionic liquids local structure on the charging of porous carbon electrodes[99].

4.2.2 Ionic Liquid–Iron Interaction Model

The energies of interaction between the ionic liquids based in alkyl-ammonium cations, alkyl-sulfonate or bistriflamide anions and an Fe(001) surface were determined from first principles, using methods based on the density functional theory (DFT). A brief description of this class of calculations will now take place.

In DFT calculations, the total energy of a system (i.e. the solution to the Schöringer's equation) is expressed in terms of the total electron density (ρ) rather than the wave function (ψ) as in the Hartree Fock calculations (the most basic type of *ab initio* calculations). The functional part of the name in DFT, comes from the fact that the energy is a function of the electron density, $E[\rho]$, and the electron density is itself a function of position, $\rho(r)$, and a function of a function is called a functional. This method is not truly *ab initio*, since the functional has to be specified and it is obtained by fitting parameters to molecular properties on a data set. Therefore, the results are not strictly derived from approximations based in the postulates and theorems of quantum mechanics, which is the basis of an *ab initio* calculation. The advantages of using DFT methods are that it is faster, it includes electron correlations and it gives results which are in better agreement with experiments, particularly for d-metal complexes. A great variety of density functionals have been defined, to better model the exchange and correlation interactions, accounting for the electron-electron interaction. The functional used here is named M06-L[100], a meta-GGA exchange-correlation functional. It was chosen because

it provides a correct description of long-range and non-bonded energies, bond lengths and vibrational frequencies, for systems involving both transition metal and main-group atoms.

In order to perform an *ab initio* calculation three specifications have to be defined: 1) type of calculation; 2) theoretical method and 3) basis set. The type of calculation which was performed in this work is the type 'single point energy', where the energy is predicted for a system with a specific geometry, at a single, fixed point on the potential energy surface. For the point 2), the theoretical method, it refers to the technique to solve the Schöringer's equation numerically and in this case is the meta-GGA functional MO6-L mentioned before. Finally, the basis set denotes a set of functions, each representing an atomic orbital (centered on the atoms), of which linear combinations generate the molecular orbitals. The basis sets used here will be of triple-zeta quality, TZVP[101], and an effective core potential (ECP) basis set from the Stuttgart/Cologne group[102]. Where the TZVP basis set is used for the non-metallic atoms and the ECP for iron. This last basis set permits to use an energy adjusted pseudopotential to represent the core electrons of the transition metals as a Ne-like core, in an attempt to replace the complicated effects of the motion of the core. Two different pseudopotentials are available for iron: ECP10MHF and ECP10MDF. In both, the number of core electrons which are replaced by the pseudopotential is 10 and the reference system used for generating the pseudopotential is M, meaning neutral atom. The last two letters stand for the theoretical level: HF is Hartree-Fock and DF is relativistic (that takes into account "relativistic effects"). We chose to use the ECP10MHF form of the pseudopotential.

In order to optimize the computational time and construct a transferable model, which should be able to describe families of ionic liquids, the ionic system was split into four fragments: butane (C_4H_{10}), tetramethylammonium (N^+_{1111}), methylsulfonate ($CH_3SO_3^-$) and NTf_2^-. The transferability of parameters, known as the *LEGO* approach[103], is based in the assumption that the electron density distribution in a given molecular fragment is similar for different molecules and different locations of the fragment, which is a reasonable approximation if the fragments are carefully chosen. Butane, for example, will be composed of sites that, once parameterised, can be re-used to represent alkyl side chains of different lengths. Present knowledge about the structure and charge distribution of ionic liquids supports the existing rationale for defining the fragments, by separating charged head-groups and non-polar

alkyl side-chains. Then, by assembling different molecular fragments one can build a great variety of cation-anion combinations. Calculations with each fragment will allow us to obtain specific site-site parameters for interactions between the atoms of the ions and those of an iron cluster. If the fragments are too complex, it becomes difficult to isolate the role of each site.

The interaction energies of each fragment was sampled at different distances and different orientations from a (001) bcc cluster of iron, containing 21 atoms. Figure 4.1 presents snapshots of the different systems.

All the DFT calculations were carried out using the Gaussian 09[104] software. As referred before, for the ionic fragments we employed a TZVP[101] basis set, and for iron an ECP10MHF. Convergence problems led us to proceed by obtaining an initial approximation with the LSDA[105] functional and the LanL2DZ[106;107] basis set for both metal and liquid.

Iron is ferromagnetic therefore open-shell calculations were performed with a spin multiplicity M=2S+1 (S represents the number of unpaired electrons) of 2.9 per atom according to Frauenheim et al.[108]. The basis set superposition error was corrected through the counterpoise (CP) technique[109], which will be briefly explained. The energy of interaction (E_{inter}) of a dimer formed by molecules A and B can be defined in a simplified way as:

$$\Delta E_{inter} = E_{\mathrm{AB}}^{\mathrm{A\cup B}}(\mathrm{AB}) - \mathrm{E}_{\mathrm{A}}^{\mathrm{A}}(\mathrm{A}) - \mathrm{E}_{\mathrm{B}}^{\mathrm{B}}(\mathrm{B}) \tag{4.5}$$

where the superscripts represent the basis functions, the subscripts represent the geometry and the quantity in parentheses denotes the chemical system considered. Therefore $E_{\mathrm{AB}}^{\mathrm{A\cup B}}(\mathrm{AB})$ represents the energy of the bimolecular complex AB evaluated in the dimer basis (the union of the basis sets on A and B), computed at the geometry of the dimer. The other terms represent the energy of each one of the molecules, evaluated in its own basis. However, when monomer A approaches monomer B, the dimer can be artificially stabilized as A can ”borrow” some extra basis functions from B to describe

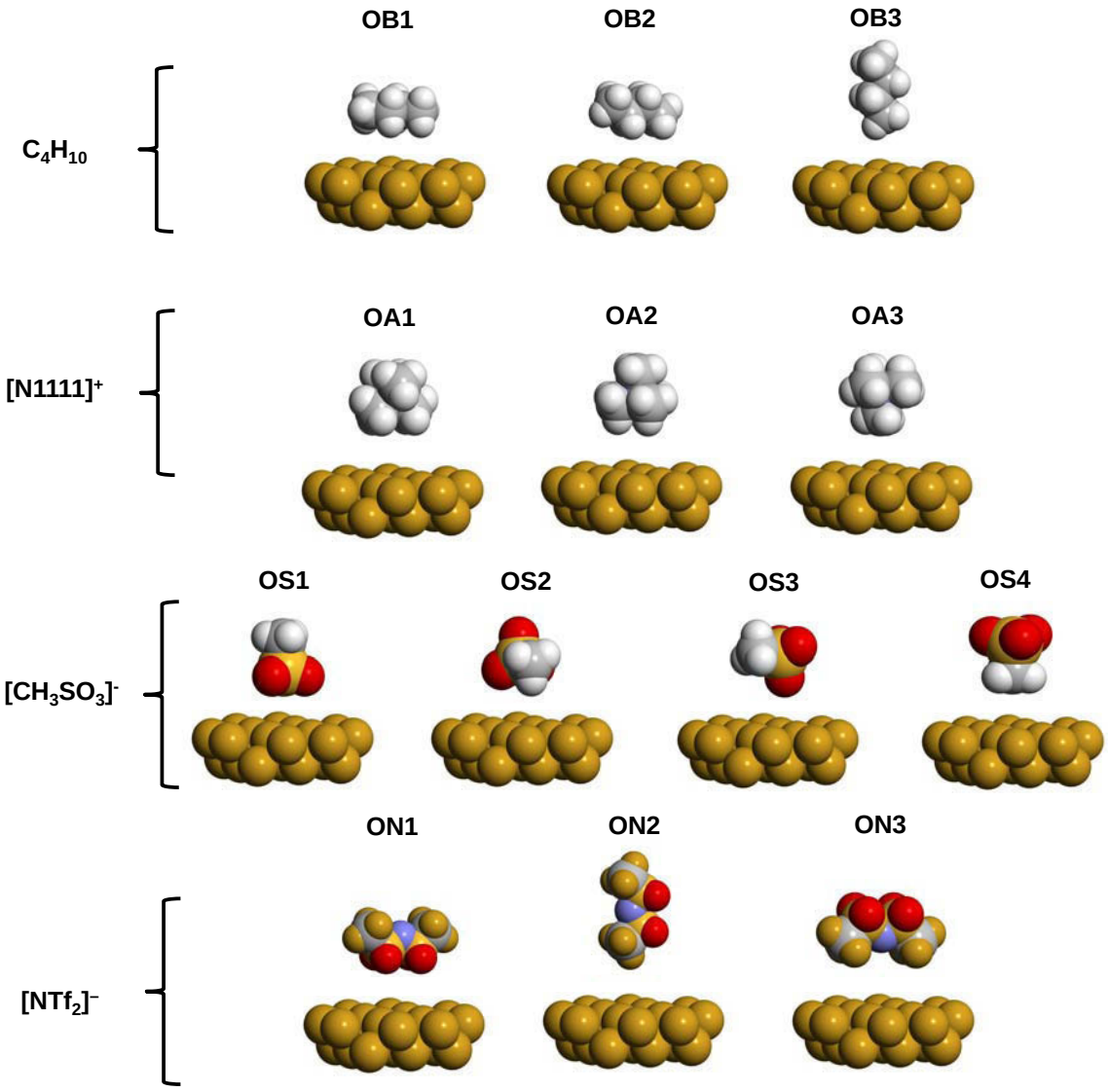

Figure 4.1: Orientations of the fragments of ionic liquid in respect to a 21 atom Fe(001) cluster .

its electron distribution, and vice versa. The improvement in the descriptions of monomers A and B through the addition of extra accessible basis functions is not an error itself; the error arises from the inconsistent treatment of the monomers, once they are able to access additional functions from the other monomer at shorter intermolecular distances, but at large intermolecular distances, the other monomer is too far away (the overlap integrals are too small) for its functions to provide stabilization. One method proposed to correct this phenomenon is the CP correction where the corrected interaction energy is defined as:

$$\Delta E_{inter}^{CP} = E_{\mathrm{AB}}^{\mathrm{A\cup B}}(\mathrm{AB}) - \mathrm{E}_{\mathrm{AB}}^{\mathrm{A\cup B}}(\mathrm{A}) - \mathrm{E}_{\mathrm{AB}}^{\mathrm{A\cup B}}(\mathrm{B}) \tag{4.6}$$

The potential energy between the fragments of the ionic liquid and the metal cluster are shown in Figure 4.2, where the points represent DFT energy calculations for each ion fragment at different orientations and distances from the metal cluster.

It can be seen that the adsorption energy of butane on Fe(001) (Figure 4.2a) in the most favorable orientation (in red) is –33 kJ·mol^{-1}, corresponding to a physisorption mechanism[110], where the attraction between the absorbed species and the surface arises from van der Waals forces. We could not find experimental values of adsorption energies of butane on iron, but it is known that the adsorption at Ni(111)[111] is –37 kJ·mol^{-1}. Interactions between adsorbed butane molecules can account for about 25% of the total adsorption energy[112], therefore we can conclude that our calculation is a very reasonable prediction. This is a stringent test to the DFT method used, because if electron correlation is not included, then the interaction of an alkane with a metal would be essentially non-binding, since it is due to dispersion forces.

For the methylsulfonate fragment (Figure 4.2c) the binding energy to the iron surface is larger than that of the other molecules, especially in the orientation labeled in red where the oxygen's are directed towards the surface. This reveals the possible presence of a component of chemisorption[113] between

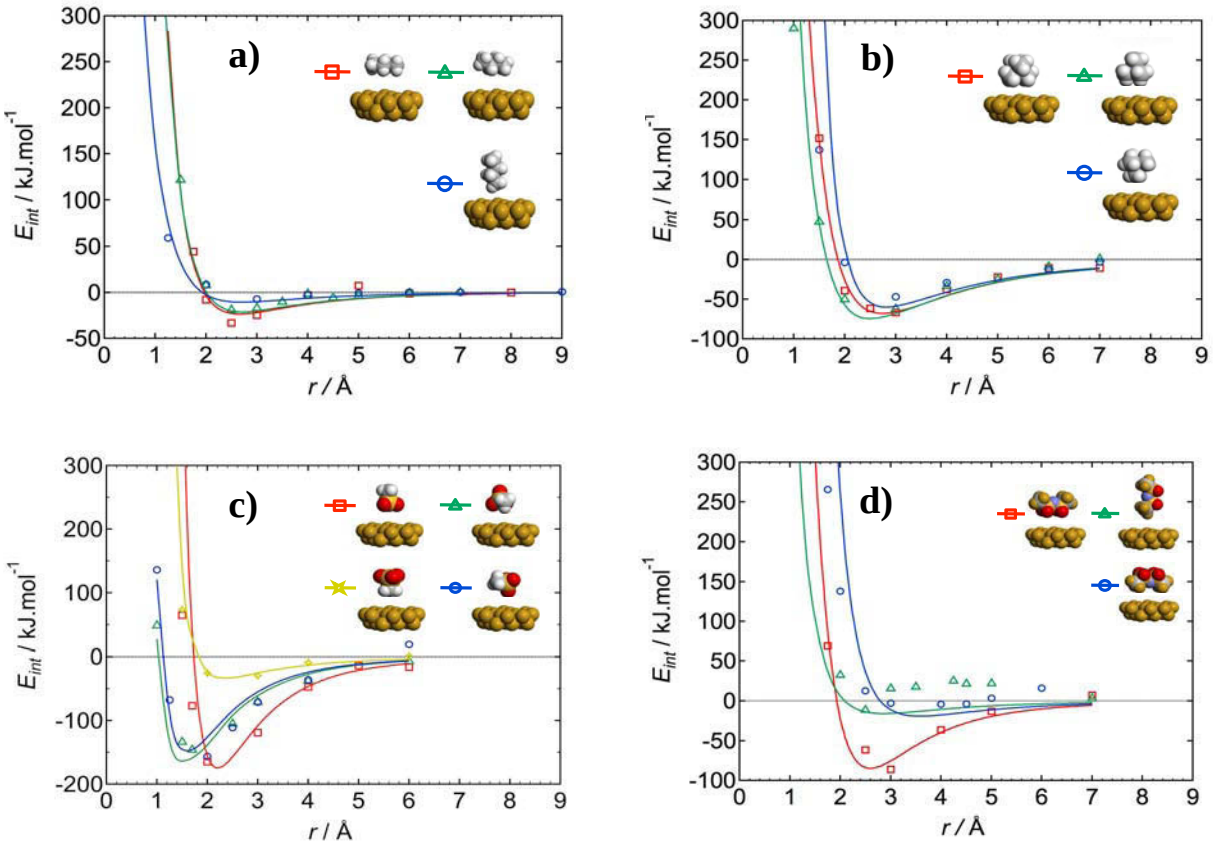

Figure 4.2: Interaction energy of the different fragments of ionic liquid at a series of distances and orientations from a 21-atom cluster of Fe(001): a) butane; b) tetramethylammonium; c) methylsulfonate; d) bistriflamide.

the oxygen's and sulfur of the fragment and the iron atoms. Such a strong sorption is not seen when the methyl group is directed towards the cluster.

In the case of the NTf_2^- anion (Figure 4.2d), the orientation where the oxygen atoms are pointing directly towards the surface is, once again, the one having the highest adsorption component in respect to the iron surface. The orientation labeled in blue has a repulsive character, due to the presence of the electronegative F atoms closer to the metal surface.

In order to use the results of interaction energies in a molecular simulation, a mathematical function

must be chosen to represent the potential energy surface in terms of distance and orientation. We decided to use an site-site model, in which the overall energy of the fragment of ionic liquid and the metal cluster is decomposed into site-site contributions. As such, each energy point for a given distance and orientation in Figure 4.2 is the result of all the pairwise interactions between each site of the ionic liquid fragment and each metal atom. This allows the representation of flat or of arbitrary surface topologies, or different conformations of the ions, and to apply the fragment approach to build different ions by combining head-groups and alkyl side chains.

The number of different sites cannot be too large since we start from a data set of about 30–40 points of discrete energies for the series of distances and orientations, for each fragment. This data set allows only the definition of so many parameters. We therefore chose not to represent H atoms explicitly on the fragments of the ionic liquid where these atoms are present in alkyl groups, but instead to include them in united-atom sites. The model of the ionic liquid, for the purpose of interactions with the metal, is therefore a united-atom model in terms of the alkyl chains, but an all-atom model for the remaining sites (however, when calculating ion-ion interactions the full, all-atom force field is kept). More specifically, the interactions between butane and the Fe cluster are represented by two kinds of site: one for the $–CH_3–$ groups and another for the $–CH_2–$ groups. The interactions of tetramethylammonium are represented by one site for the N and four sites for methyl groups attached to the positively charged central atom. Methylsulfonate is represented by five sites, i.e., explicit O and S atoms, and one united $–CH_3$ site connected to the negative head-group. Finally, NTf_2^- was represented by three types of interaction sites: one for the united $–CF_3$ group, one for the N atom and one for the O atoms. Due to the very different chemical environments of the methyl groups in butane or in the cation and the sulfonate anion, it is expected that the parameters describing this group are not the same. The first methyl or methylene group attached to a charged head-group is specifically parameterised, because of induction effects. If the alkyl chain is longer than one carbon, then the methyl or methylene groups further away are represented by the parameters obtained from the butane fragment. Previous experience in developing force field for ionic liquids[74] showed that from the second carbon after a charged head-group the charge distributions are close to those of alkanes.

Finally, each curve shown in Figure 4.2 represent the best fit of the DFT points using a site-site poten-

tial functions of the type nm[114], with the following form:

$$u_{ij}(r_{ij}) = \frac{E_0}{(n-m)}\left[m\left(\frac{r_0}{r_{ij}}\right)^n - n\left(\frac{r_0}{r_{ij}}\right)^m\right] \tag{4.7}$$

where i and j represent an interaction site in the ionic liquid and an atom in the metal surface, respectively. The parameters of interactions E_0, r_0, n and m, obtained by the fitting, to the DFT energies are summarized in Table 4.2.

Table 4.2: Fitting parameters of interaction that will be used in the molecular dynamics simulations of ionic liquid confined between the two iron surfaces.

Fragment	**Site**	$\boldsymbol{E_0}$ (kJ·mol^{-1})	$\boldsymbol{r_0}$ (Å)	$\boldsymbol{n}$	$\boldsymbol{m}$
C_4H_{10}	C_{2H}	2.069	3.116	7	6
	C_{3H}	0.530	4.654	7	6
N^+_{1111}	N	1.999	5.166	6	5
	C_N	1.480	4.277	6	5
$CH_3SO_3^-$	O	17.226	2.258	7	6
	S	11.018	3.402	7	6
	C_S	0.573	3.864	7	6
NTf_2^-	OBT	2.553	3.414	7	6
	NBT	0.516	3.505	7	6
	C_{3F}	0.701	5.215	7	6

The polarization of the metal surface was taken into account in the metal-liquid force field by adding a coulombic term to Eq. 4.7. To obtain a polarizable metal surface, a Drude-rod concept was employed[115], by addition of an embedded dipole into each metal atom, which is free to rotate in response to the local electric field. It was demonstrated that this technique reproduces the interaction energy of

charges with conducting surfaces, in a similar manner to induced dipoles, while avoiding instability issues. Two opposite charges (q) are separated by a distance (l_0) and have the same mass (m). The parameters used herein are: l_0 = 0.7 Å, m = 0.5 a.u., q = 0.3 e. These parameters were taken from[115] and are suitable to molecular dynamics simulations. The Drude dipoles interact with the point charges present in all sites of the ionic liquid, as specified by the IL-IL force field.

The induced dipoles represent the polarization of the metal surface. However, the typical time-scales of this polarization are much faster than the nuclear motions. Thus, a careful choice of the mass of the fictitious charged atoms and the time-step have to be made, so that the nuclear motions and the oscillators are adiabatically decoupled. Otherwise, the Drude oscillators will exchange too much kinetic energy with the rest of the simulation and the energy of the system is not conserved. If a system obeys the laws of classical mechanics (Newton's Laws) than the energy of such system is a conserved quantity. The integration algorithm used in the MD simulations (Verlet leapfrog) generates trajectories, in which the total energy (kinetic plus potential energy) is conserved. Such condition was confirmed in all the performed simulations by observing the constant profiles for this quantities.

A Lennard-Jones potential is sometimes not sufficient to describe these complex interactions and other potential functions are required, like the function nm used here. In order to show that such a potential model is not sufficient to describe the complex interactions involving ionic liquids and a metal surface, Figure 4.3 represents the fitting of the DFT energies for the fragments butane and tetralkylammonium, using a Lennard–Jones potential function instead of the nm potential function. The difference between these curves and the ones plotted in Figures 4.2a) and b) is quite evident. With the LJ potential, repulsive and attractive interactions are not correctly described, even for the small and neutral butane fragment.

In summary, the final system studied in this chapter is formed by slabs of iron atoms in contact with a central slab of ionic liquid, as shown in Figure 4.4. Three main types of interaction potentials are used: i) ion-ion interactions within the ionic liquid are described by a classical force field with intramolecular terms including harmonic covalent bonds, harmonic valence angles, and cosine series for torsion energy profiles around dihedral angles; non-bonded intermolecular forces are given by Lennard-Jones

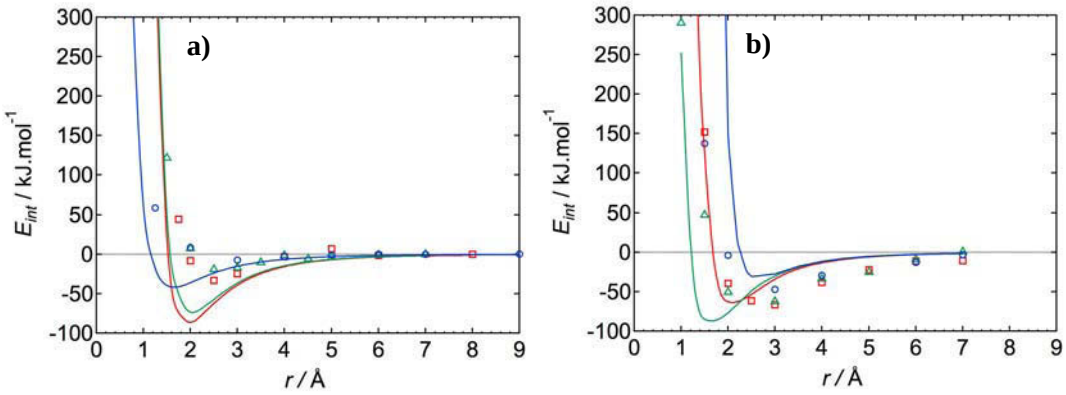

Figure 4.3: Fitting of the DFT interaction energies for fragments a) butane and b)tetramethylammonium with the cluster of iron, with a Lennard-Jones potential function.

atomic sites and fixed electrostatic point charges; ii) metal-metal interactions within the iron slabs are represented by a Finnis-Sinclair potential; iii) interactions between the metal and the ionic liquid are described by the nm potential functions developed here, between each metal atom and each site on the ions, augmented by electrostatic forces of the point charges on the ions and the Drude dipoles on the metal atoms that represent the polarization of the surface. The Drude dipoles have no effect on the lattice structure of the metal slabs at the temperatures of this study.

4.2.3 Simulation Conditions

A slab of 500 ion pairs was simulated between surfaces of bcc iron by molecular dynamics using the DL_POLY package[78]. The simulation box is a rectangular parallelepiped of dimensions $L_x L_y L_z$ ($L_x = L_y = 49$ Å, $L_z \approx 120$ Å) with periodic conditions applied in the three dimensions (Figure 4.4).

All simulations were performed at 500 K in order to improve statistical sampling, since due to the high viscosity of ionic liquids convergence of the molecular dynamics trajectories is too slow at room temperature for practical purposes[116]. This behavior was also identified in section 3.3.3 of this thesis.

The initial configuration was a low-density lattice containing only the ionic liquid that was equili-

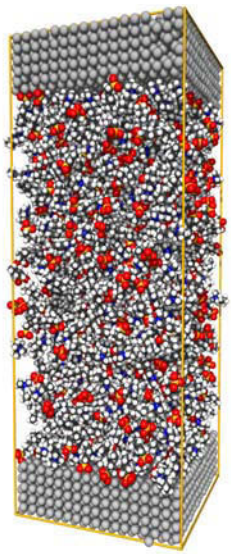

Figure 4.4: Snapshot of the equilibrated simulation box composed by 500 ion pairs confined between two surfaces of bcc iron, with tridimensional periodic conditions.

brated at constant pressure (1 atm) with a timestep of 1 fs in order to reach the correct density of the bulk liquid. Then the metallic surfaces, each composed of 2890 Fe atoms in the bcc structure, were inserted. The dimension of the resulting box was increased along the z-axis by placing 60 Å of empty space on the external sides of the surfaces. This procedure is necessary in order to apply the three-dimensional *Ewald summation method* in a slab geometry using the 3D periodic boundary condition[69].

After equilibration of the system, a simulation run of 2 ns was executed with a time step of 2 fs, at constant NpT regulated by Nosé-Hoover thermostat and barostat. Long-range electrostatic interactions were handled through the *Ewald summation technique*, using a real-space cut-off of 14 Å. The number of wave-vectors considered in the reciprocal space were of $k_x = k_y = 5$ and $k_z = 23$, yielding a relative accuracy better than 0.001 in the calculation of the electrostatic energy. Configurations from the production runs were stored every 1000 time steps for subsequent analyses.

Four ammonium-based ionic liquids were simulated: 1-butyl-1,1,1-trimethylammonium metanesulfonate [N_{1114}][C_1SO_3], 1-butyl-1,1,1-trimethylammonium butanesulfonate [N_{1114}][C_4SO_3], 1-butyl-1-ethyl-1,1-dimethylammonium butanesulfonate [N_{1124}][C_4SO_3] and 1-butyl-1,1,1-trimethylammonium

bis(trifluoromethylsulfonyl)imide (or bistriflamide) $[N_{1114}][NTf_2]$. Their structures and the labels used for each atom are presented in Figure 4.5.

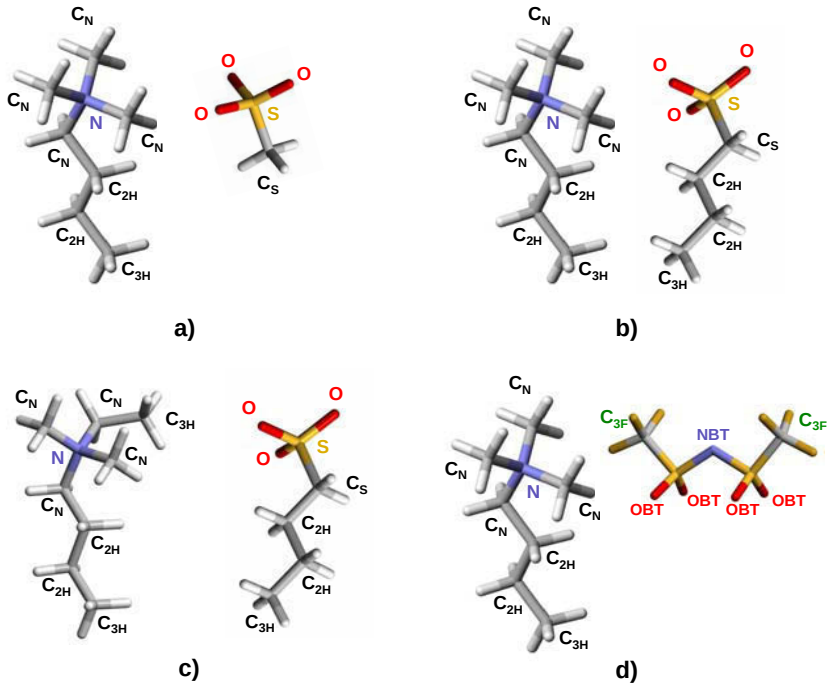

Figure 4.5: Molecular structures of four simulated ionic liquids based in alkylammonium cations and alkyl-sulfonate anions or bistriflamide: a) $[N_{1114}][C_1SO_3]$; b) $[N_{1114}][C_4SO_3]$ and c) $[N_{1124}][C_4SO_3]$ and d) $[N_{1114}][NTf_2]$.

4.2.4 Alkyl Side Chain Orientation

To analyze in detail the orientations of the ions at the interface, the position of the alkyl side chains with respect to the ionic head groups is plotted with the aid of a Legendre polynomial of this type:

$$\langle P_2(\theta)\rangle = \left\langle \frac{1}{2} \quad 3\cos^2(\theta) \quad 1) \right\rangle \tag{4.8}$$

where θ is the angle between the surface normal ($\vec{v}$) and a vector chosen in the ion ($\vec{u}$). A scheme is represented in Figure 4.6. In the ionic liquids of this study based in alkylammonium cations and alkylsulfonate anions, both ions are composed of an essentially spherical head-group (trimethylammonium or sulfonate) and an alkyl side chain, therefore the vector representing the orientation of the ions was defined between a central atom of the cation or anion head-group and the terminal atom of the respective alkyl side chain.

$P_2(\theta)$ varies from 1 to 0.5. A value of 1 indicates that the vector on the ion is parallel to the surface normal and therefore the alkyl side chains are perpendicular to the metal surface. A value of 0.5 means that the vectors are perpendicular and the preferred orientation of the side chains is parallel to the metal surface.

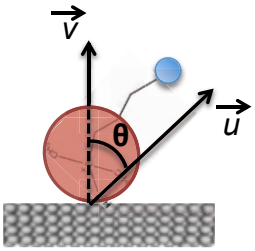

$-0.5 < P_2(\theta) < 1$

$P_2(\theta) = 1$ $\quad \vec{u} \parallel \vec{v}$

$P_2(\theta) = -0.5$ $\quad \vec{u} \perp \vec{v}$

Figure 4.6: A legendre polynomial is used to measure the angle between an alkyl side chain in the cation or the anion, in respect to the surface normal.

4.3 Results and Discussion

The results will be organized as follows: first, the effect of the alkyl side chain length in the cation or the anion will be analyzed, through the study of three different ionic liquid structures composed of alkylammonium and alkylsulfonate: $[N_{1114}][C_1SO_3]$, $[N_{1114}][C_4SO_3]$ and $[N_{1124}][C_4SO_3]$; then, the nature of the anion will be evaluated, by comparing two ionic liquids which have the same cation, but two different anions — $[N_{1114}][C_4SO_3]$ and $[N_{1114}][NTf_2]$. The ordering and interactions occurring at the interfacial layer will be analyzed.

4.3.1 Effect of the Alkyl Side Chain Length

The first results from MD simulations analyzed here are the structure of the ions near the surface, through the number-density profiles for atoms of $[N_{1114}][C_1SO_3]$, $[N_{1114}][C_4SO_3]$ and $[N_{1124}][C_4SO_3]$, presented in Figure 4.7.

The oxygen atoms (O) and the sulfur atom (S) are representative of the head group of the alkylsulfonate anion, the nitrogen atom (N) is representative of the positive head-group of the alkylammonium cation and, finally, the terminal carbon atoms (C_{3H}) represent the position of the longer alkyl chains in either anions or cations.

In the local density profiles of the ionic liquid $[N_{1114}][C_1SO_3]$ (Figure 4.7a), two layers of anion head-groups are observed, clearly marked by the peaks of S and O atoms. Logically, O atoms approach closer to the surface. The distance between the first two peaks of O density is 5.0 Å, therefore this really corresponds to two layers of anions, not to distances between O atoms within the same sulfonyl group, which is of 2.4 Å. Only one structured layer of cation head-groups is perceived through the strong peak of N atoms, at distances from the surface that are slightly larger than that of S atoms from the anion. The most probable positions of the terminal C atoms in the butyl side chain of the cations correspond to a second peak, which is slightly higher than the first, and appears further away from the surface than the charged head-groups. The interfacial layer of this ionic liquid is composed of anion and cation head-groups separated by 2 Å, with a second, less-ordered layer of anions. Separation between cations and anion layers is significantly smaller than their diameters, therefore both types of ion are present at the interface, with the alkyl chains preferentially directed towards the bulk liquid.

Overall similar features are seen in the atomic density profiles of the other two ionic liquids, which have longer alkyl side chains. The main difference from the ionic liquid discussed above is a reduction in the height of the peaks arising from the anion and cation head-groups. In $[N_{1114}][C_4SO_3]$ (Figure 4.7b) the second peak of terminal atoms of the alkyl side chains (of cations and anions confounded) is strong, denoting an ordering of alkyl tails pointing away from the metal surface. This is characteristic of segregation between the alkyl chains, which aggregate to form non-polar regions, and the charged head-groups[24]. In this ionic liquid the second layer of anions appears less structured than in

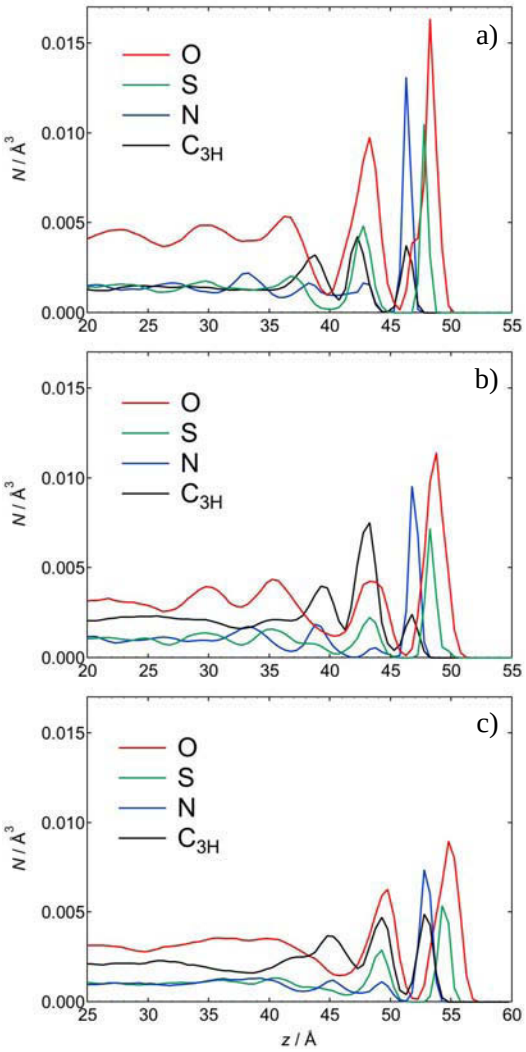

Figure 4.7: Atomic density profiles at the metal surface for the ionic liquids: a) $[N_{1114}][C_1SO_3]$, b) $[N_{1114}][C_4SO_3]$ and c) $[N_{1124}][C_4SO_3]$. The red curve and the green curve represent the oxygen atoms and sulfur atoms of the head-group of the anion, respectively; the blue curve represents the nitrogen atoms of the head-group of the cation, and the black curve represents the terminal carbon atoms of the butyl side chains of either the anion or the cation.

the first ionic liquid.

Finally, in $[N_{1124}][C_4SO_3]$ (Figure 4.7b) the ordering of the alkyl tails is less prominent than in $[N_{1114}][C_4SO_3]$, an interesting effect of the ethyl group in the ammonium cation. The presence of this short alkyl chain attached to the cation head-group seems to disrupt some of the segregation between charged and non-polar moieties, clearly apparent when comparing plots b) and c) in Figure 4.7.

Color-labeling the atoms belonging to different functional groups of the ionic liquid allows the visualization of the interfacial layer, depicted in Figure 4.8: anion head-groups (red) tend to reside closer to the surface followed by the alkylammonium head groups (blue) and finally the alkyl chains (black). The influence of the alkyl side chain length in the structure at the interface is clearly present, mostly for cases a) and b).

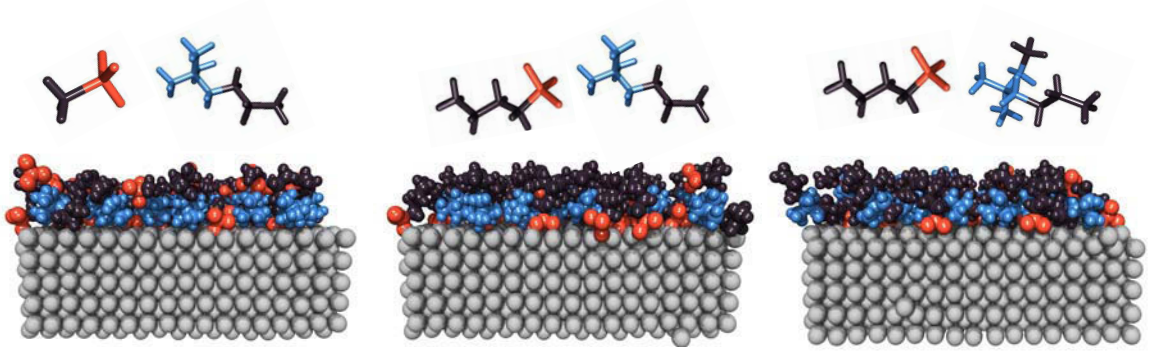

Figure 4.8: Snapshots of the metal-ionic liquid interface using color labeling: a) $[N_{1114}][C_1SO_3]$, b) $[N_{1114}][C_4SO_3]$ and c) $[N_{1124}][C_4SO_3]$. Red, blue and black colors depict the sulfonyl head-groups of anions, ammonium head-groups of cations, and alkyl chains of both ions, respectively.

In order to analyze in detail the orientations of the ions at the interface, the position of the alkyl side chains with respect to the ionic head groups was plotted with the aid of a Legendre polynomial. The principle was described in a previous section, 4.2.4.

For the ionic liquids studied here, as central atom of the cation or anion head-group the atoms N and S were chosen, respectively. As terminal atoms of the respective alkyl side chains, the C_S atoms were chosen for $[N_{1114}][C_1SO_3]$ and the C_{3H} atoms for $[N_{1114}][C_4SO_3]$ and $[N_{1124}][C_4SO_3]$. Figure 4.9 shows the preferred orientations of the cation (blue curves) and the anion (red curves) for the different ionic liquids in this study. Reference orientations are also present for a better understanding.

For $[N_{1114}][C_1SO_3]$ (Figure 4.9a), there is a first negative peak corresponding to the C_S group in the anion of the first adsorbed layer that is oriented parallel to the metal surface. Then, for an length of 1.5 Å the C_S group will form an angle of around 45° with the surface, after which the orientation becomes random and $P_2(\theta)$ decays to zero.

In $[N_{1114}][C_4SO_3]$ (Figure 4.9b) the orientational order extends up to 12 Å from the surface and there are two pronounced peaks due to the anions separated by about 3.5 Å, in agreement with the number-density profile for the C_{3H} atom (Fig. 4.7a). The first of these peaks corresponds to an angle of $\sim 50°$ with the metal surface, while the second peak corresponds to a position quasi perpendicular to this surface.

Finally, for the anions of $[N_{1124}][C_4SO_3]$ (Figure 4.9c) the ordering of the alkyl chains decays at shorter lengths in comparison with the other two ionic liquids, in agreement with the density profiles presented in Figure 4.7c. The first peak indicates the tendency of the $S-C_{2H}-C_{2H}-C_{2H}-C_{3H}$ chain to adopt an orientation parallel with respect to the metal, followed by a second layer in which the anions are mostly perpendicular. It is interesting to observe that, although there is only one methyl group differentiating $[N_{1124}][C_4SO_3]$ from $[N_{1114}][C_4SO_3]$, the behavior of the first layer of the alkyl side chains in the anions are opposite. In general the anions adopt a perpendicular orientation to the surface due to the strongly adsorbed oxygen atoms that render conformations parallel to the surface unfavorable.

The cation chains behave similarly in all three ionic liquids, being preferentially parallel to the surface for the first $\sim$1 Å after which, for 2 Å, they lie at an average angle of 35° with the surface. This proximity of the cation side chains with the surface is opposite of what is observed for the anions,

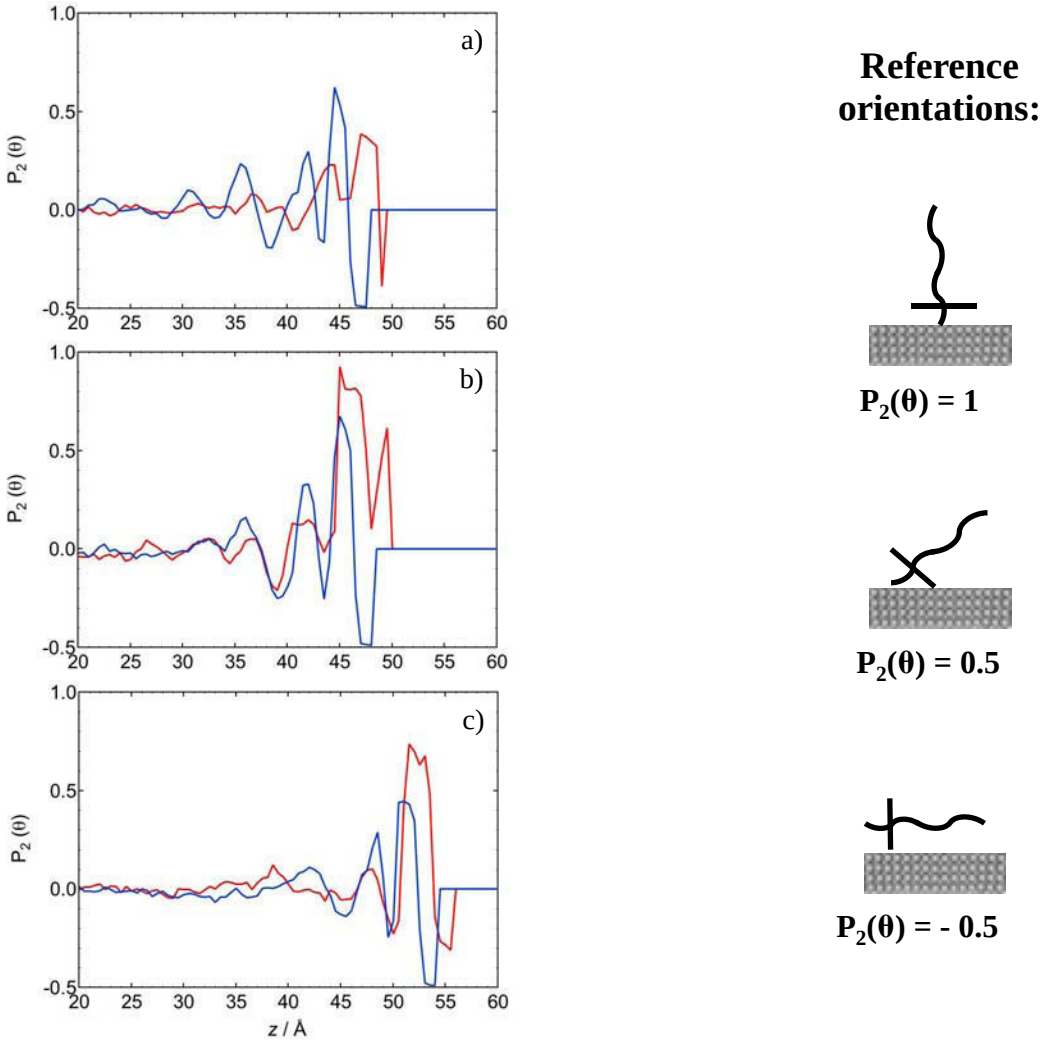

Figure 4.9: Orientational ordering parameter, $P_2(\theta)$, for the ionic liquids a) $[N_{1114}][C_1SO_3]$, b) $[N_{1114}][C_4SO_3]$ and c) $[N_{1124}][C_4SO_3]$. The red curves represent the orientation of the anions and the blue curves those of the cations. The reference orientation of the alkyl side chains is illustrated in the figure.

likely because in the cation head-groups there are no specific interactions with Fe, as is the case of the oxygen atoms of the anions.

The thickness and structure of the electrostatic layer near the surface, resulting from the ordering of ions, can be seen in the plots of electrostatic charge distribution in Figure 4.10. The net charge in the liquid when moving away from the surface is first negative (due to the closest layer of anion head-groups) and then positive (due to the first layer of cations). The overall result is that the charges at the interface form an Helmholtz-like layer (see section 1.4), characterized by the formation of two layers of equal and opposite charge at the metal surface.

In $[N_{1114}][C_1SO_3]$ (Figure 4.10a) a second negative peak is present as a result of the second layer of anions, which is still structured, in this ionic liquid. The interfacial layer is roughly one-ion thick, extended between 5 and 10 Å into the liquid.

Spectroscopic studies[52] using vibrational sum frequency generation revealed the formation of an interfacial layer at a metal surface, which is one-ion thick, with both anions and cations present at the surface, thus the present results agree with this general picture. Unfortunately, the study concentrates on the orientation of the imidazolium ring of the cations and provides no information on the orientation of the alkyl side chains.

A previous molecular simulation study using a model analogous to the one presented here[56], but focusing on the structure of imidazolium bistriflamide ionic liquids solvating a metal nanoparticle, yielded the same overall pictures as the present work: an interfacial layer that is essentially one ion thick with cation head-groups and anions in the vicinity of the surface and the alkyl side chains directed away from the nanoparticle.

Simulations of molten salts at conducting surfaces, for spherical ions such as in LiCl[55] also indicate the formation of one adsorbed layer (in the absence of an applied surface electrical potential) with charge fluctuations quickly screened into the liquid.

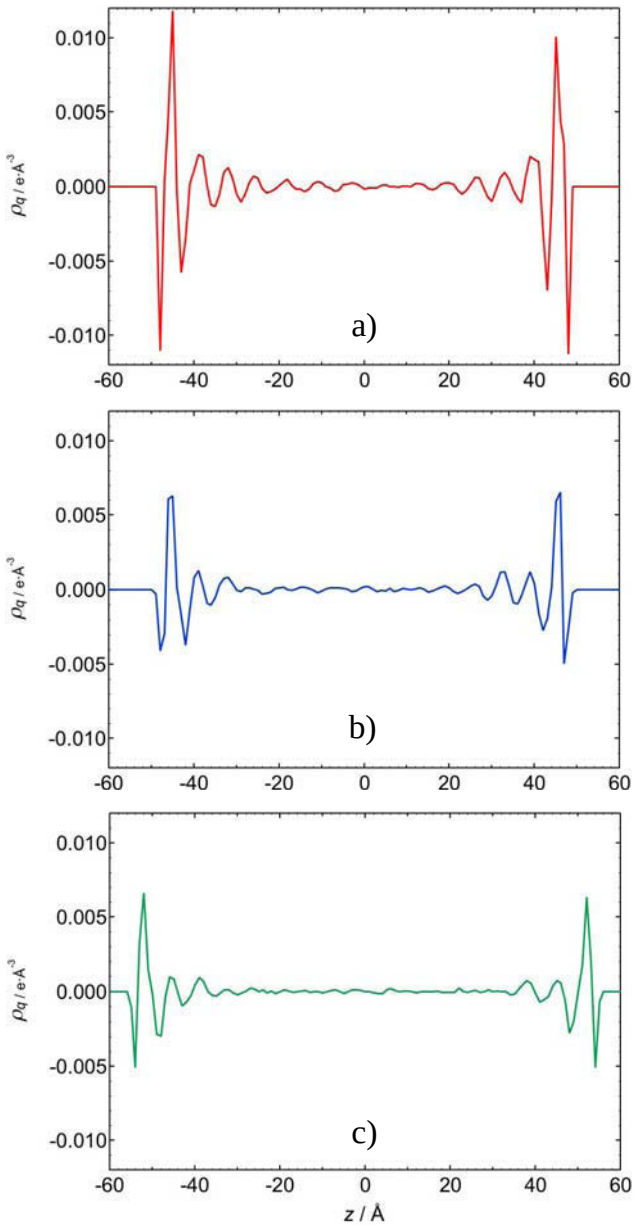

Figure 4.10: Plots of electrostatic charge distribution along the simulation box for the ionic liquids a) $[N_{1114}][C_1SO_3]$, b) $[N_{1114}][C_4SO_3]$ and c) $[N_{1124}][C_4SO_3]$.

4.3.2 Effect of the Nature of the Anion

The impact of the anion's structure on the arrangement of the atoms at the interface was analyzed via the simulation results of two ionic liquids: $[N_{1114}][C_4SO_3]$ and $[N_{1114}][NTf_2]$.

The number density profiles of the atoms of both ionic liquids is presented in Fig. 4.11. Their structures and corresponding atoms labels can be seen in Fig. 4.5. The atomic density profile of $[N_{1114}][C_4SO_3]$ has already been discussed in Figure 4.7b, but it is also given here for a more direct comparison with the ionic liquid with NTf_2^- anion.

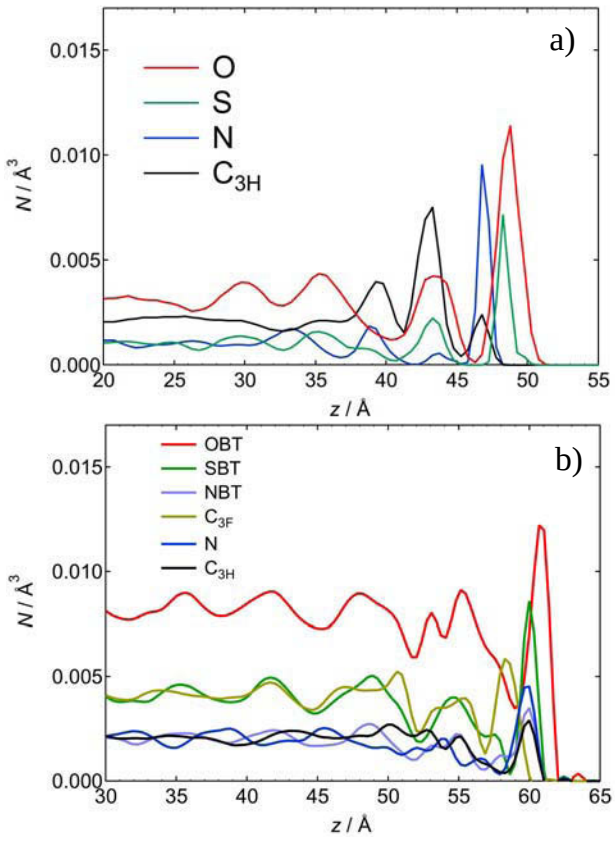

Figure 4.11: Atomic density profiles at the metallic surface for two ionic liquids composed of the same cation, but different anions: a) $[N_{1114}][C_4SO_3]$ and $[N_{1114}][NTf_2]$.

By observing both graphs one can easily realize that the ordering at the interface changes according

to the type of anion, even if the oxygen atoms are in both cases next to the surface. In the ionic liquid based in butanesulfonate (Fig. 4.11a) there is an ordered interfacial layer composed of the anion species closer to the surface, followed by the cation and the alkyl side chains. The anion-cation layer thickness is about 5 Å, but an atomic ordering can be observed up to 10 Å from the surface.

In the case of $[N_{1114}][NTf_2]$ (Fig. 4.11b) the atoms which reside closer to the surface are the oxygen atoms of the anion species and all the other atoms, expect for the C_{3F} group, are in the same layer. This means that the NTf_2^- anions will adopt a position which is preferentially parallel to the surface with the C_{3F} groups pointing away from the metal. Each anion unit occupies around 6 Å of the surface, impeding the packing of other ionic species. The molecular ordering for this ionic liquid is lost after the first layer, which is ∼5 Å thick.

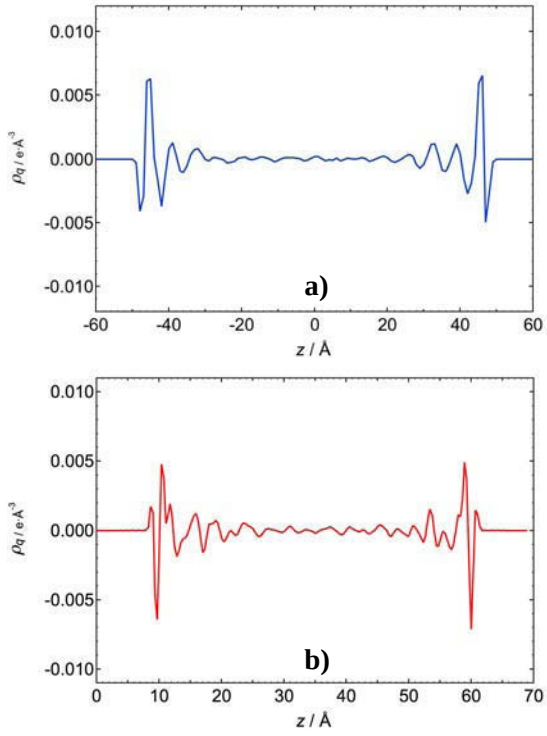

Figure 4.12: Plots of electrostatic charge distribution along the simulation box for the ionic liquids: a) $[N_{1114}][C_4SO_3]$ and b) $[N_{1114}][NTf_2]$.

The charge ordering at the metallic surface can be seen in the plots of electrostatic charge distribution

in Figure 4.12. To simplify the comparison of the two ionic liquids, image a) is plotted, although its discussion was already done in Fig. 4.10b.

In a first conclusion, the charge distribution for $[N_{1114}][C_4SO_3]$ seems to have a higher degree of order than for $[N_{1114}][NTf_2]$. In this last compound, the first negative peak corresponds to the oxygen atoms which are closer to the surface. The positive peak at around 59 Å corresponds to the SBT and NBT atoms of the anion specie and the N atoms of the cation, resulting in a net positive charge. There is a small negative peak at $\sim$ 55 Å that corresponds to the F atoms.

4.4 Summary

In the present chapter, an interaction model between an ionic liquid and a metal surface based on quantum chemical calculations and including the polarization of the metal was developed. The model is of atom-atom type and therefore it is independent of the conformation of the ions and of surface topology and can be used to represent flat or rough surfaces.

The ordering of three alkylammonium alkylsulfonate ionic liquids ($[N_{1114}][C_1SO_3]$, $[N_{1114}][C_4SO_3]$ and $[N_{1124}][C_4SO_3]$) with different alkyl side chain lengths was studied at an iron surface. The variations in the molecular structure of the ions allowed us to deduce relations between these structures and the interfacial layer of ionic liquid. The first conclusion is that both anions and cations are found in the interfacial layer, which is of the order of one-ion thick, a result of the electrostatic screening of the ionic medium. This is in agreement with experimental results from the literature. Nonetheless, when the alkyl side chains are shorter in the anions, a second layer of anions with a significant ordering is observed. The charged head groups lie close to the surface, with a predominance of the oxygen atoms of the anions that are strongly adsorbed. The role of the alkyl side chains in the cation and the anion are not similar: whereas the alkyl (butyl) side chains of the anions tend to point away from the surface, the butyl side chains of the first layer of ammonium cations tend to orient parallel to the surface. Therefore, there is a non-negligible interaction of the alkyl side chains with the iron surface.

Furthermore, when the nature of the anion was changed, the behavior at the surface was found not to be the same. It was found that the anion has in fact a very important role in the formation of ordered layers of ions at the surface. When an ionic liquid $[N_{1114}][NTf_2]$ was present, both cation and anion were found to be in the same layer close to the surface and the charge ordering is reduced to one layer.

In the next chapter, the models developed here will be used to perform non-equilibrium molecular dynamics simulations of systems under shear, in order to study the impact of the molecular structures in the friction coefficient and to be able to establish structure-property relations.

CHAPTER 5

Non-Equilibrium Molecular Dynamics Simulations of Ionic Liquids at Metallic Surfaces

5.1 Scope of the Chapter

In the present chapter, the results from non-equilibrium molecular dynamics (NEMD) simulations of ionic liquids interacting with surfaces of iron will be analyzed. Our purpose is to mimic the experimental conditions by modeling the interactions between the ionic liquid and shearing surfaces.

We develop a procedure for a quantitative prediction of the friction coefficient at different loads and shear rates. The dependence of friction on the load, shear velocity, surface topology, length of the alkyl side chains and nature of the anion in the ionic liquid are investigated. The changes in the frictional forces are explained in terms of the specific arrangements and orientations of the ionic liquid near the surface.

5.2 Methods

5.2.1 Geometry of the System

Each simulated system was composed of 200 ion pairs of ionic liquid confined between surfaces of bcc iron. The simulation box is a rectangular parallelepiped of dimensions $L_x L_y L_z$ ($L_x = L_y = 43$ Å, L_z variable) with periodic boundary conditions applied in the three dimensions.

Two types of surfaces were studied: a rough and a flat surface. Each rough surface was composed of 1572 Fe atoms and each flat surface of 1200 Fe atoms. Both surfaces were in a (001) plan of a body-centered cubic crystal (bcc) lattice.

The rough surface was build from a solid block of iron with a large number of iron layers. Two asperities in the truncated cone geometry were carved out from the block through elimination of atoms. The truncated cones have different radius (basis radius) — 12 Å and 10 Å— but the same height — 8 Å. This process was made for one of the surfaces and the other one was made by translation of the coordinates of the first. In the end both surfaces were opposite to each other with the asperities in the interior part. The topology of the surfaces can be seen in Figure 5.1.

Each metallic structure was built with two distinct regions: an outermost region composed of 4 monolayers of iron atoms and an innermost region, which also included the asperities in the case of the rough surface. See Figure 5.2 for a clear explanation. The outermost region (Fe-rigid), which will not be in direct contact with the liquid, was kept rigid during the simulations meaning that it is able to move as a solid block. To this region, velocity (v_x) and load (F_z) will be applied. The innermost region (Fe-mobile), which is in direct contact with the liquid, is free to move according to its interactions (through the appropriated potentials), and is the one which will be thermostated.

A problem associated with the modeling of friction through MD is that the kinetic energy will be converted into heat that needs to be removed in order to keep a steady state. By coupling a Langevin thermostat to the Fe-mobile regions of the surface including the asperities, the liquid lubricant was allowed to heat up and at the same time there will be some heat dissipation through the solid[117].

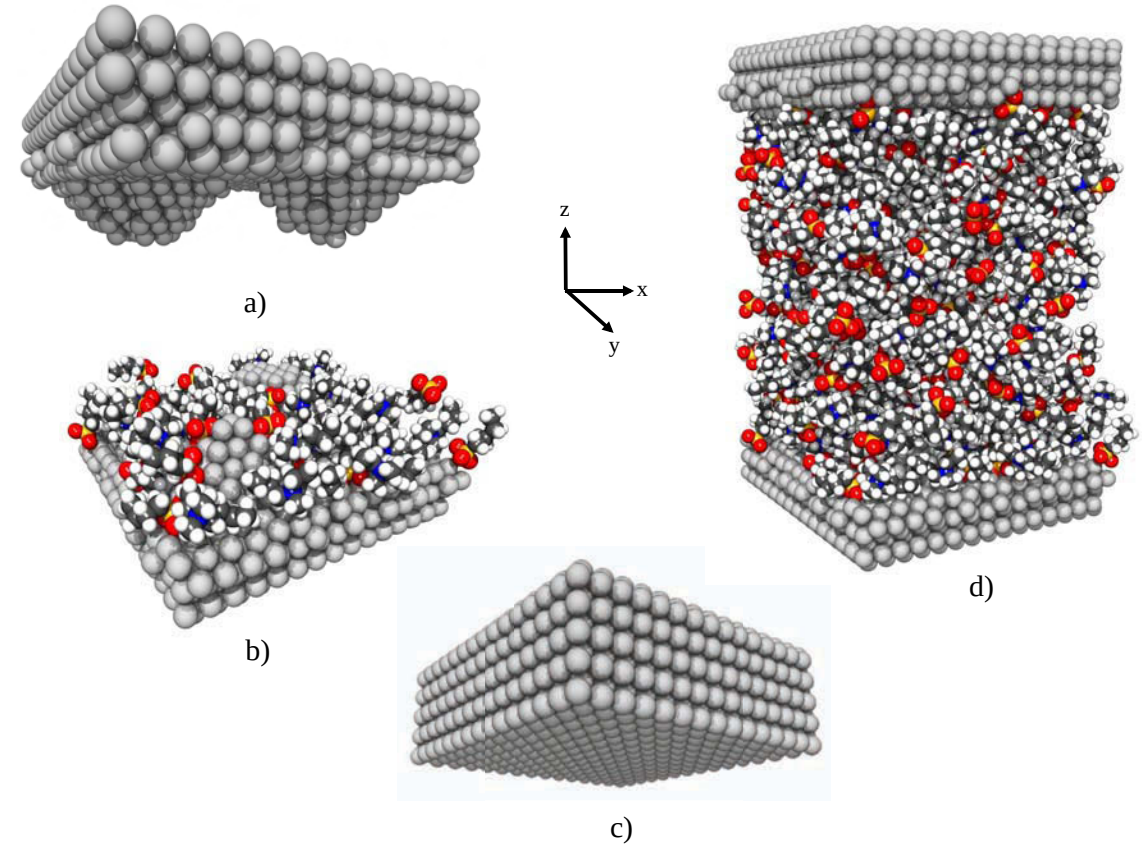

Figure 5.1: Snapshots of the simulated system: a) topology of the rough surface, with two different asperities; b) representation of the region of the metal surface that will be in direct contact with the liquid; c) representation of the flat surface; d) snapshot of the equilibrated cell, a slab of 200 ion pairs confined between two surfaces of bcc iron.

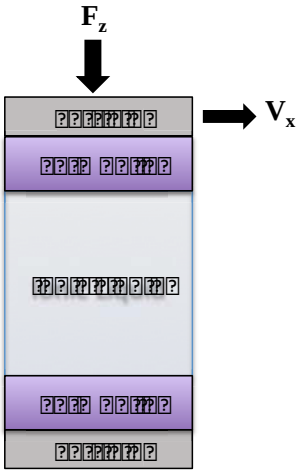

Figure 5.2: Scheme of the sheared system. The Fe-rigid region represents the iron atoms which are displaced as a rigid block, and the Fe-mobile region, the atoms of iron which are free to move according to their interactions and that will be thermostated. In the middle of the surfaces there will be the ionic liquid. Load and shear velocity will be applied to the Fe rigid region.

5.2.2 NEMD Simulation Conditions

Five ionic liquids containing different alkyl chains in the cation or the anion were studied: 1-butyl-1,1,1-trimethylammonium metanesulfonate $[N_{1114}][C_1SO_3]$, 1-butyl-1,1,1-trimethylammonium butanesulfonate $[N_{1114}][C_4SO_3]$, 1-butyl-1-ethyl-1,1-dimethylammonium butanesulfonate $[N_{1124}][C_4SO_3]$, 1-butyl-1,1,1-trimethylammonium octylsulfonate $[N_{1114}][C_8SO_3]$ and 1-butyl-1,1,1-trimethylammonium bis-(trifluoromethylsulfonyl)imide (or bistriflamide) $[N_{1114}][NTf_2]$. Their structures and the labels used for each atom were presented in the last chapter — Figure 4.5 — except for the ionic liquid $[N_{1114}][C_8SO_3]$ which structure is the same than for $[N_{1114}][C_4SO_3]$, but with six units $–C_{2H}–$ between the C_S and C_{3H} atoms, instead of only two.

The LAMMPS molecular dynamics package[118] was used to perform all simulations. The initial configuration was a low-density lattice containing both the ionic liquid and the surfaces that was equilibrated in the microcanonical ensemble (NVE) from 0 K to 500 K, by small temperature increments.

All C−H bonds of the ionic liquid and the Fe−q bonds of the Drude dipoles on the metal were constrained using the SHAKE algorithm.

To achieve the correct density of the bulk (see section 3.4), the surfaces were brought together by applying a constant velocity to the upper surface, in the $-z$ direction. When this condition was achieved the compression was stopped and the system was further equilibrated for 1 ns with a time step of 1 fs, at constant NVT regulated by a Langevin thermostat connected to the Fe-mobile regions, as explained in the previous section. A snapshot of the equilibrated cell can be seen in Figure 5.1.

A non-equilibrium simulation was then performed over 1.5 ns with a time step of 1 fs, by imposing a continuous shear velocity along the x direction (v_x) to the Fe-rigid region of the upper surface, while keeping the Fe-rigid region of the bottom surface fixed. At the same time that shear occurred, a constant force (F_z) was applied in the $-z$ direction to the sheared region. All non-equilibrium simulations were performed at constant NVT coupled with a Langevin thermostat connected to the Fe-mobile regions. To understand the principle behind a MD simulation at the non-equilibrium, the reader is redirected to chapter 2, section 2.3.

Long-range electrostatic interactions were handled through the particle-particle particle-mesh solver[119] (P3M) with a relative accuracy of 0.0001 in the calculation of the interaction energy and a real-space cut-off of 14 Å. In order to apply the three-dimensional P3M method in a slab geometry using the 3D periodic boundary condition, the dimension of the simulation box was increased along the z-axis by placing 30 Å of empty space on the external sides of each surfaces[69].

As already mentioned, during the NEMD simulations different values of shear velocity and load were imposed. The goal is to study the behavior of the system as a function of such quantities. Two approaches were followed: 1) imposing a constant value of shear velocity while varying the applied load and 2) imposing a constant value of load while varying the velocity of shear. Thus, for constant shear velocities varying from 0.01 to 15 m·s^{-1}, different values of load were applied: 1.6, 3, 6, 10 and 14 nN, which correspond to a nominal pressure of 89, 166, 333, 555 and 776 MPa, respectively. Trajectories of all atoms were stored every 500 steps during the course of the simulation for subsequent

analyses, described in the next section.

5.2.3 Determination of Thermodynamic Properties. Definition of the Pressure Tensor.

The application of a certain shear along the x-axis will create a velocity gradient in the $z-$direction for the particles in the fluid. It is then very important to check the thermodynamic properties along the z-axis where the heterogeneities take place. This may influence the local equilibrium properties and also dynamic properties of the liquid such as viscosity and diffusion. The local properties are averaged in each slab z_k of thickness Δz, obtained by splitting the simulation cell along the z-direction into N_{slabs}. The value of Δz cannot be to high, if one wants to have a consequent number of points to calculate an average, but it cannot also be to small, so that each slab has satisfactory statistics. The value used here varied between 0.2 and 1.0 Å.

The average instant velocity, $v_\alpha(z_k)$, of particles in the slab z_k of the simulation box along the α direction (x, y or z) is given by:

$$v_\alpha(z_k) = \frac{\sum_{i=1}^{N} H_k(z_i)(v_i)_\alpha}{\sum_{i=1}^{N} H_k(z_i)} \tag{5.1}$$

where N denotes the total number of particles, $(v_i)_\alpha$ is the velocity of particle i in the direction α and $H_k(z_i)$ is a top-hat function, defined as:

$$H_k(z_i) = \begin{cases} 1 & \text{if } z_k - \frac{\Delta z}{2} < z_i < z_k + \frac{\Delta z}{2} \\ 0 & \text{otherwise} \end{cases} \tag{5.2}$$

In a non-equilibrium MD simulation, the stored data (that will be used in subsequent analysis) need to correspond to configurations which are in local thermodynamic equilibrium. For a chemical system, such condition is achieved when the following three equilibria are simultaneously verified: thermal, mechanical and chemical. Taking into account that the chemical potential of the constituents of the system doesn't change with time, only the thermal and mechanical equilibrium need to be verified.

The thermal equilibrium is associated to the temperature ($T_{\alpha\beta}$), given by:

$$k_B T_{\alpha\beta}(z_k) = \left\langle \frac{\sum_{i=1}^{N} H_k(z_i) m_i \left[(v_i)_\alpha - u_\alpha(z_k)\right] \left[(v_i)_\beta - u_\beta(z_k)\right]}{\sum_{i=1}^{N} H_k(z_i)} \right\rangle \tag{5.3}$$

where $\langle \cdots \rangle$ denotes the average over all configurations of the system; m_i is the mass of particle i; $(v_i)_\alpha$ and $(v_i)_\beta$ is the velocity of particle i in the α and β directions, respectively; $u_\alpha(z_k)$ and $u_\beta(z_k)$ are the streaming velocity, defined by the average of the velocity in those directions, defined in Eq. 5.1, for a given configuration and $H_k(z_i)$ is the top-hat function defined in Eq. 5.2.

The conditions to reach thermal equilibrium are that the terms corresponding to $\alpha \neq \beta$ are zero along the box, and the diagonal terms, i.e., the terms where $\alpha = \beta$, have a temperature corresponding to the imposed value in every slab z_k. The total temperature of the system can be calculated from the diagonal components of the temperature tensor by:

$$T_{tot} = \frac{T_{xx} + T_{yy} + T_{zz}}{3} \tag{5.4}$$

The mechanical equilibrium is measured through the pressure. As with thermal equilibrium, mechanical equilibrium is achieved when the pressure is constant over time and every point of the system

experiences the same value. The total pressure of a system is given by the virial equation:

$$PV = Nk_BT + \frac{1}{3}\sum_{i=1}^{N-1}\sum_{j<i}^{N} r_{ij} \cdot F_{ij} \tag{5.5}$$

where P is the virial pressure; T is the temperature; V is the volume; k_B is the Boltzmann's constant and F_{ij} is the force associated to the site-site interactions between i and j at a given distance r_{ij}. The first term of this equation is associated to the ideal behavior of the particles and the second term is a configurational term, associated to the non-bonded interactions between the particles.

To obtain a profile of pressure along the z-axis that allows to conclude about the mechanical equilibrium, it is necessary to measure the different components of the pressure tensor along this direction, as in the case of the temperature tensor. In the present work, the calculation of the components of the pressure tensor is based in the Irving-Kirkwood (IK) definition [120;121]. This definition allows a local description of the elements of the pressure tensor and leads to a correct calculation of these elements in a pseudo two-dimensional periodic system (Eq. 5.6). Using this molecular definition, it is assumed that molecules i and j give a local contribution to the pressure tensor in a given slab, if the line joining the center of mass of i and j crosses, starts, or finishes in that slab. Each slab will have $1/N_{slabs}$ of the total contribution from the i–j interaction.

$$\begin{aligned} P_{\alpha\beta}(z_k) &= P^{kin}_{\alpha\beta}(z_k) + P^{conf}_{\alpha\beta}(z_k) \\ &= \langle\rho(z_k)\rangle k_B T_{\alpha\beta}(z_k) \\ &+ \frac{1}{L_x L_y}\left\langle \sum_{i=1}^{N-1}\sum_{j>i}^{N} \frac{(\boldsymbol{r_{ij}})_\alpha (\boldsymbol{F_{ij}})_\beta}{|z_{ij}|}\, \theta\left(\frac{z_k - z_i}{z_{ij}}\right)\theta\left(\frac{z_j - z_k}{z_{ij}}\right)\right\rangle \end{aligned} \tag{5.6}$$

Each pressure component is expressed as a sum of a kinetic term $P_{\alpha\beta}^{kin}(z_k)$ and a configurational term $P_{\alpha\beta}^{conf}(z_k)$, corresponding to the first and the second arguments of Equation 5.6, respectively. In Eq. 5.6, $\rho(z_k)$ is the density of particles in the slab z_k; $T_{\alpha\beta}(z_k)$ is the temperature of Eq. 5.3; $(\mathbf{r_{ij}})_\alpha$ is the vector distance between the center of mass of molecules i and j in the direction α; $\theta(z)$ is a unit step function that is 0 for $z < 0$ and 1 elsewhere; L_xL_y is the surface area normal to the z axis and finally $(\mathbf{F_{ij}})_\beta$ is a vector in the direction β, that represents the sum of all site–site forces acting between molecules i and j in that direction, and is defined as:

$$\boldsymbol{F_{ij}} = \sum_{a=1}^{N_i}\sum_{b=1}^{N_j}(\boldsymbol{f_{iajb}}) = \sum_{a=1}^{N_i}\sum_{b=1}^{N_j} -\frac{\boldsymbol{r_{iajb}}}{r_{iajb}}\left[\frac{dU_{ab}^{NB}(r_{iajb})}{dr_{iajb}}\right] \tag{5.7}$$

where f_{iajb} is the force between atom a in molecule i and atom b in molecule j; r_{iajb} is the distance between atom a and atom b; N_i and N_j are the number of atoms in molecules i and j, respectively and U_{ab}^{NB} is the total potential energy associated to the non-bonded interactions between atoms a and b. This potential function will have contributions from van der Waals interactions occurring within the liquid; electrostatic interactions occurring within the liquid and between the liquid and the point charges in the surface and finally, contributions from the liquid-metal interactions. Van der Walls interactions are represented by a Lennard-Jones potential (LJ), electrostatic interactions are handled with the *Ewald summation technique* and the interactions between liquid and metal are represented by a nm potential function (M–IL). Equation 5.6 can be written as:

$$\begin{aligned} P_{\alpha\beta}(z_k) &= \langle\rho(z_k)\rangle k_B T_{\alpha\beta}(z_k) \\ &+ P_{\alpha\beta}^{LJ}(z_k) + P_{\alpha\beta}^{M-IL}(z_k) + P_{\alpha\beta}^{R}(z_k) + P_{\alpha\beta}^{K,1}(z_k) + P_{\alpha\beta}^{K,2}(z_k) \end{aligned} \tag{5.8}$$

where the superscripts R and K represent the contributions of the Ewald real space and Ewald reciprocal space, respectively. As explained in section 2.2.1, electrostatic interactions (which have a long-range character) are handled through the *Ewald Summation* technique, in which the Coulombic potential is divided into a short-range term representing the real space (R) and a long range term representing the reciprocal space (K).

The Lennard-Jones contribution to the pressure tensor can be calculated from the following expression:

$$P_{\alpha\beta}^{LJ}(z_k) = -\frac{1}{A}\left\langle \sum_{i=1}^{N-1}\sum_{j>i}^{N}\sum_{a=1}^{N_i}\sum_{b=1}^{N_j} \frac{(\boldsymbol{r_{ij}})_\alpha(\boldsymbol{r_{iajb}})_\beta}{r_{iajb}} \times \frac{dU_{LJ}(r_{iajb})}{dr_{iajb}}\frac{1}{|z_{ij}|}\,\theta\left(\frac{z_k - z_i}{z_{ij}}\right)\theta\left(\frac{z_j - z_k}{z_{ij}}\right)\right\rangle \tag{5.9}$$

For further details on the U_{LJ} term the reader is redirected to section 2.2.1. The contribution of the M–IL interaction to the local pressure is

$$P_{\alpha\beta}^{M-IL}(z_k) = -\frac{1}{A}\left\langle \sum_{i=1}^{N-1}\sum_{j>i}^{N}\sum_{a=1}^{N_i}\sum_{b=1}^{N_j} \frac{(\boldsymbol{r_{ij}})_\alpha(\boldsymbol{r_{iajb}})_\beta}{r_{iajb}} \times \frac{dU_{M-IL}(r_{iajb})}{dr_{iajb}}\frac{1}{|z_{ij}|}\,\theta\left(\frac{z_k - z_i}{z_{ij}}\right)\theta\left(\frac{z_j - z_k}{z_{ij}}\right)\right\rangle \tag{5.10}$$

For further details on the potential function U_{M-IL} see section 4.2.2. The real space contribution to the local pressure tensor is given by:

$$
\begin{aligned}
P^{R}_{\alpha\beta}(z_k) &= \frac{1}{4\pi\varepsilon_0 A}\left\langle \sum_{i=1}^{N-1}\sum_{j>i}^{N}\sum_{a=1}^{N_i}\sum_{b=1}^{N_j} q_{ia}q_{jb} \right. \\
&\times \left(\frac{2}{\sqrt{\pi}}\,\alpha\, r_{iajb}\exp(-\alpha^2 r_{iajb}^2) + \operatorname{erfc}(\alpha\, r_{iajb})\right) \\
&\times \left. \frac{(\boldsymbol{r_{ij}})_\alpha(\boldsymbol{r_{iajb}})_\beta}{r^3_{iajb}}\frac{1}{|z_{ij}|}\,\theta\left(\frac{z_k - z_i}{z_{ij}}\right)\theta\left(\frac{z_j - z_k}{z_{ij}}\right)\right\rangle
\end{aligned}
\tag{5.11}
$$

Finally, the contributions of the reciprocal space are given by the following two expressions:

$$
\begin{aligned}
P^{K,1}_{\alpha\beta}(z_k) &= \frac{1}{4\pi\varepsilon_0}\left\langle \frac{2\pi}{V^2}\sum_{h\neq 0} H_k(z_i)Q(h)S(\boldsymbol{h})S(-\boldsymbol{h}) \right. \\
&\times \left. \left(\delta_{\alpha\beta} - \frac{2\boldsymbol{h}_\alpha\boldsymbol{h}_\beta}{h^2} - \frac{2\boldsymbol{h}_\alpha\boldsymbol{h}_\beta}{2\alpha^2}\right)\right\rangle
\end{aligned}
\tag{5.12}
$$

$$
\begin{aligned}
P^{K,2}_{\alpha\beta}(z_k) &= -\frac{1}{4\pi\varepsilon_0}\left\langle \frac{2\pi}{V^2}\sum_{i=1}^{N}\sum_{a=1}^{N_i}(\boldsymbol{r}_{ia} - \boldsymbol{r}_i)_\beta\, q_{ia} \right. \\
&\times \left. \sum_{h\neq 0} H_k(z_i)Q(h)i\boldsymbol{h}_\alpha\ [S(\boldsymbol{h})\exp(-i\boldsymbol{h}\cdot\boldsymbol{r}_{ia}) - S(-\boldsymbol{h})\exp(-i\boldsymbol{h}\cdot\boldsymbol{r}_{ia})]\right\rangle
\end{aligned}
\tag{5.13}
$$

The description of the different terms in Equations 5.11–5.13 which were not mentioned along this text, can be found in section 2.2.1.

An algorithm was implemented using these definitions, that allows measuring the components of the pressure tensor tensor of Eq. 5.6. We aim to demonstrate that the methodology used here allows

an accurate calculation of the tangential and normal elements of the pressure tensor, which are key-elements in the prediction of the kinetic friction coefficient, subject of the next section.

5.2.4 Determination of Rheological Properties: Calculation of Friction

The definition of friction based in the Amontons' 1^{st} Law ($F_x = \mu F_z$), is only valid for non-adhering surfaces. This subject has been discussed in section 1.2.1. In summary, if adhering surfaces are present, a non-zero friction coefficient associated to the adhesion of lubricant particles at the surface will exist, even when no "external" load is applied. To overcome this problem, a modified Amontons' 1st Law was proposed by Derjaguin[10] in 1934, by adding a term — F_0 — related to the "internal" load contribution due to the adhesion of particles to the surface. The Amontons' Law becomes:

$$F_x = F_0 + \mu F_z$$

where:

$$P_{xz} = \frac{F_x}{A} \text{ and } P_{zz} = \frac{F_z}{A} \tag{5.14}$$

Therefore we can obtain a modified Amontons' 1^{st} law in terms of pressure:

$$\langle P_{xz}(z_k) \rangle = P_0 + \mu \langle P_{zz}(z_k) \rangle \tag{5.15}$$

where P_0 represents the adhesion-dependent contribution to the pressure, a term which is proportional to the number and strength of interactions between the fluid and the surface when sliding is occurring. The terms $\langle P_{xz}(z_k) \rangle$ and $\langle P_{zz}(z_k) \rangle$ are the tangential and normal components of the pressure tensor as defined in Equation 5.6, averaged over all the slabs z_k in the z-direction and over all the configurations

of the system. The slope of $\langle P_{xz}(z_k)\rangle$ as a function of $\langle P_{zz}(z_k)\rangle$ will yield the friction coefficient μ.

With this modification, the friction coefficient will be no longer independent of the load, in disagreement with Amontons' 1st Law:

$$\mu = \frac{P_{xz} - P_0}{P_{zz}} \tag{5.16}$$

which gives $\mu = \infty$ when the applied pressure in the z direction is zero.

5.3 Results and Discussion

The molecular ordering and rheological properties of ionic liquids at a metallic surface under shear will now be investigated. First, a validation of methods will take place with the verification of the thermodynamic quantities. Then, based on a definition of pressure measured locally, the dependence of the friction with load, shear rate, surface topology and structure of the ionic liquid will take place.

5.3.1 Validation of Methods

The application of a certain shear velocity to the surfaces will generate a velocity-gradient of the particles in the fluid along the z-axis, provoking local perturbations that can have some influence in the local thermodynamic equilibrium of the system (see section 5.2.3). To predict reliable kinetic friction values using NEMD, we must guarantee that the system is in local thermal and mechanical equilibrium. Therefore it is essential to check how the temperature and pressure components along the direction normal to the surface are affected by shear.

The x-component of the velocity of the liquid along z-axis calculated through Eq. 5.1 is plotted in Figure 5.3. For completeness, different sliding velocities are represented. At each sliding velocity there is a constant z-velocity profile (*plateau*) close to the metal surface, indicating that a large fraction of ionic liquid molecules are carried by the surface. This is due to the physical adsorption of lubricant molecules at the surface, giving a *no-slip* boundary condition, in which, at the solid boundaries, the fluid will have zero velocity relative to the boundary.

At a certain distance from the surfaces, the molecules exhibit a linear velocity profile, which is a characteristic of a classical newtonian fluid. It is observed that the amount of fluid in the *no-slip* condition decreases with the increasing sliding velocity.

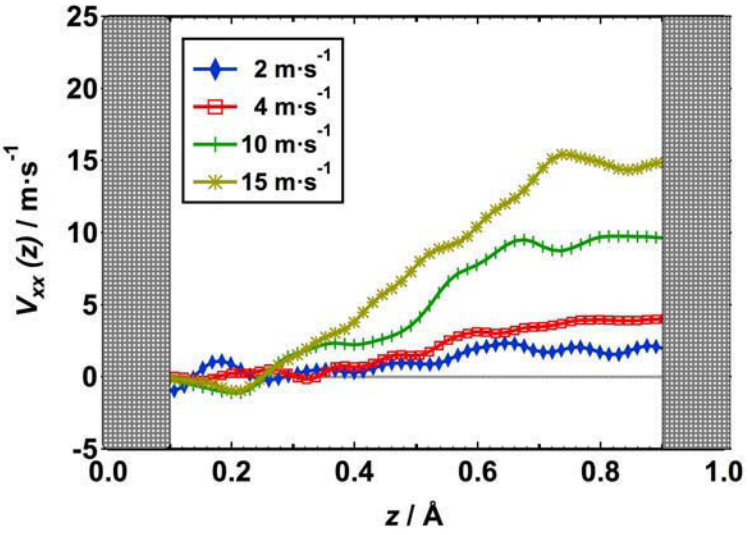

Figure 5.3: x-component of the velocity profile of the particles in the liquid, when different values of shear are applied.

The temperature tensor is an indicator of the thermal equilibrium of the system. Figure 5.4 shows the z-component of the temperature calculated from Eq. 5.3 along the z-direction, in reduced coordinates (z/L_z). We observe that the temperature profile is constant along the simulation cell. The fact that the temperature is identical at each z for the bulk liquid indicates that the configurations are well equilibrated, as expected from the thermal equilibrium of the constant-NVT statistical ensemble.

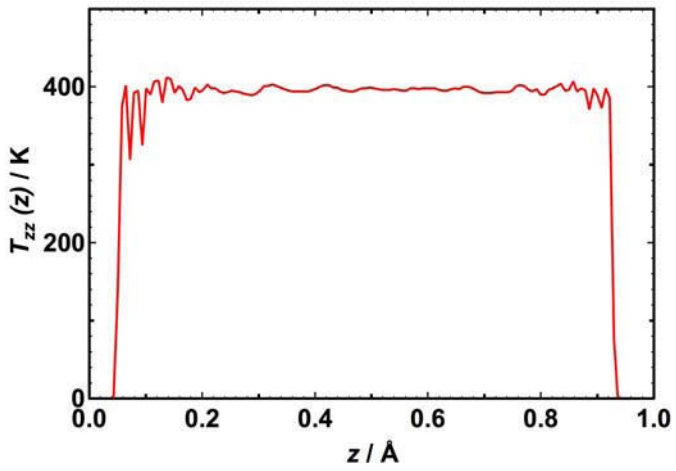

Figure 5.4: Temperature profile of the system along the simulation box, for a simulation at 500 K.

Relative to the calculation of the local elements of the pressure tensor using Equation 5.6, Figure 5.5 shows the different contributions to the normal component of the pressure tensor as a function of z.

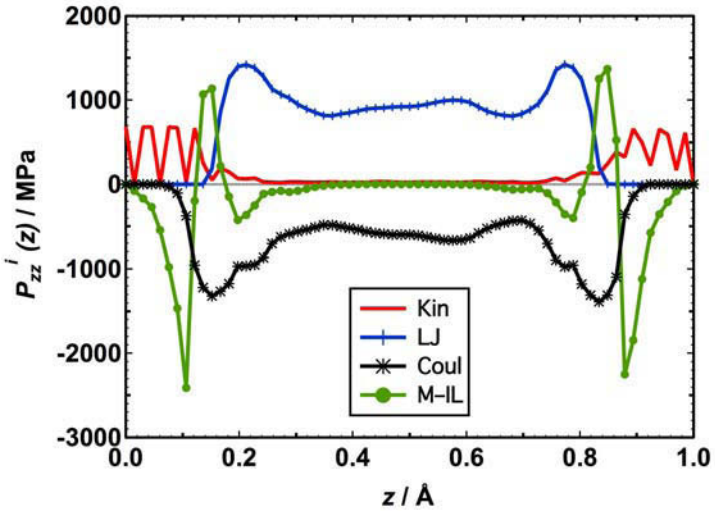

Figure 5.5: The normal component of the pressure tensor decomposed into kinetic (Kin), Lennard-Jones (LJ), Ewald (Coul) and Metal-Liquid (M-IL) contributors.

In Fig. 5.5 $P_{zz}(z)$ is separated into its kinetic (Kin), Lennard-Jones (LJ), Ewald (Coul) and Metal-Liquid (M-IL) contributors. Except for the oscillations near each surface, the different contributions show flat profiles in the bulk region that are expected for configurations at mechanical equilibrium. These oscillations come from the surface where there is a strong organization of molecules (as can be seen by the kinetic contribution, which will be compensated by the other contributions).

The tangential (xz) and normal (zz) components of the pressure tensor, under no shear and at a constant shear velocity of 4 m·s ^{1} are shown in Figures 5.6 a and b.

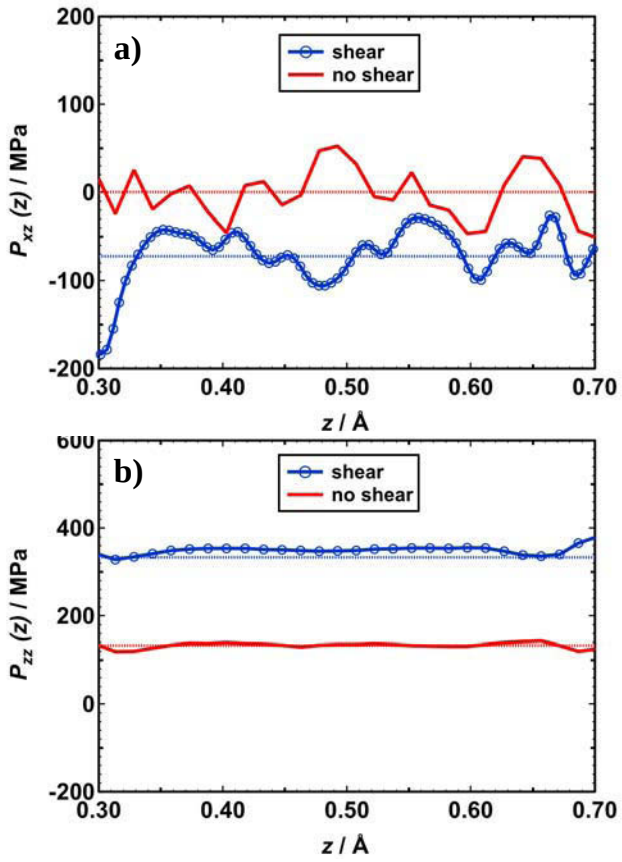

Figure 5.6: Components of the pressure tensor: a) $P_{xz}(z)$ and b) $P_{zz}(z)$ profiles when no shear and a constant shear velocity of 4 m·s ^{1} is applied, at 500 K.

The tangential component $P_{xz}(z)$, as expected from equilibrium simulations, is zero when no shear

is applied and it is negative when a sliding velocity is applied in the x-direction. When the system is sheared under a load of 6 nN, $P_{zz}(z) = 351 \pm 2$ MPa. When no shear is applied $P_{zz}(z)$ decreases to 133 ± 1 MPa. Both components of the pressure tensor are constant through the middle of the simulation box, a condition required for the local mechanical equilibrium and for a good estimation of the average components.

In conclusion, the calculations of the pressure tensor allowed us to evaluate the local mechanical equilibrium inside the simulation cell: the normal pressure ($P_N = P_{zz}$) and the tangential pressure (P_{xz}) were constant through the simulation box for a planar interface. The temperature profiles also demonstrated that the system is in thermal equilibrium. An accurate calculation of the local elements of the pressure tensor is the key-element to predict the friction coefficient by molecular simulations.

Here we have developed and validated tools to measure the kinetic friction between ionic fluids and metal surfaces. This strategy opens the way to understanding the relationship between the structure of the ionic liquid and its lubricant properties.

5.3.2 Friction as a Function of Temperature and Load

In this section, a discussion on the dependence of the kinetic friction coefficient on the load and temperature will take place, for the ionic liquid $[N_{1114}][C_4SO_3]$.

In the NEMD simulations performed in this study, a certain load is applied to the Fe rigid region (see Fig. 5.2) of the top surface, and at the same time, shear is imposed. To study the behavior of the system with load, several values of loads were applied, varying from 1.6 to 14 nN, at a constant shear velocity of 4 m·s^{-1}.

Figure 5.7 represents the relation given in Equation 5.15, plotted at different average values of P_{xz} and P_{zz}. Each point represents an isolated simulation at a given load, using a constant shear velocity of 4 m·s^{-1}. The values of P_{xz} will correspond to the frictional force and the values of P_{zz} to the force applied in the normal direction.

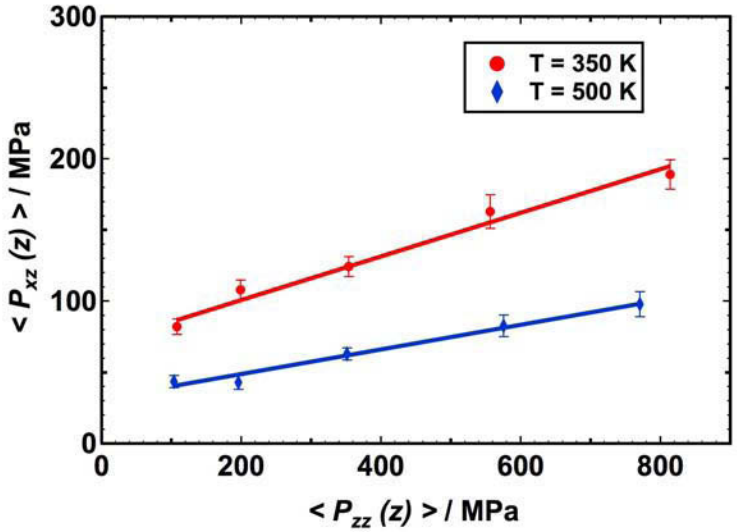

Figure 5.7: Frictional forces P_{xz} as a function of the normal forces P_{zz}

Experiments at two given temperatures were performed: 350 K (red curve) and 500 K (blue curve). The slope of these curves, in agreement with Eq. 5.15, corresponds to the kinetic friction coefficient (μ). Linear regressions give the following equations for each temperature:

$$\begin{aligned} T &= 350K : P_{xz} = (72.7 \pm 5.5) + (0.149 \pm 0.015) P_{zz} \\ T &= 500K : P_{xz} = (31.0 \pm 4.2) + (0.087 \pm 0.012) P_{zz} \end{aligned}$$

The non-equilibrium molecular dynamics predict here a friction coefficient of 0.087 at 500 K and 0.149 at 350 K. Interestingly, the simulated kinetic friction coefficients are close to the ones measured

experimentally for similar ionic liquids[47;122]. Furthermore, in most of the cases the experimental friction coefficient of systems composed of metallic surfaces in contact with ionic liquids varies between 0.05 and 0.12 [30;32;35], for a shear rate of the order of 0.01 m·s^{-1}. Therefore our results predict quite well the experimental results even if the frictional force is velocity dependent, as it will be discussed in section 5.3.3.

It can be seen that friction decreases with temperature. In fact, the temperature dependence of the friction coefficient finds its origin in the temperature dependence of the tangential component (P_{xz}) of the pressure tensor whereas the normal force is very little T-dependent. This can be seen in Figure 5.8, where the variation of the tangential and the normal components of the pressure tensor as a function of the surface separation are presented.

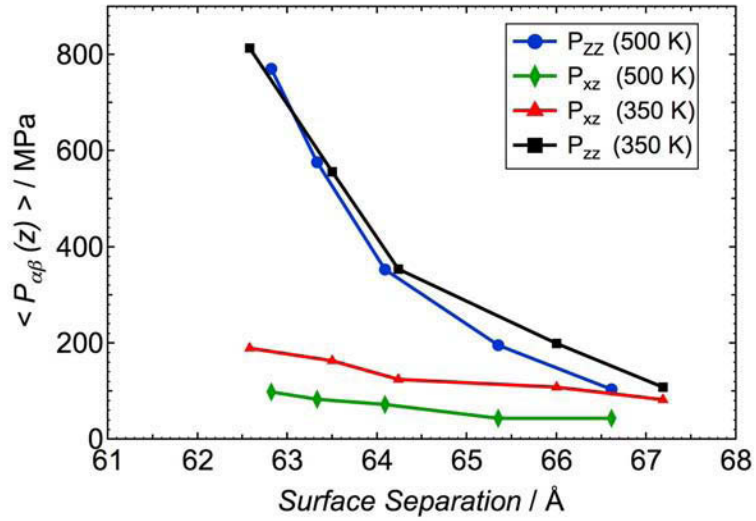

Figure 5.8: P_{xz} and P_{zz} components of the pressure tensor as a function of the surface separation.

The surface separation is also a measure of the applied load once higher loads imply lower surface separation. It can be seen that the normal component of the pressure is more significant influenced by the surface separation. This means that high values of load are necessary to approach the two metallic surfaces. In boundary lubrication, when surface separations approach the molecular dimensions, physical adsorption of the lubricant molecules at the surface occurs (*no-slip* condition) and the fluid

becomes capable of supporting high loads, in agreement to what is observed here.

These findings led us to the conclusion that the ionic liquids present in this work based in alkylammonium cations and alkylsulfonate anions present a high-load carrying capacity and form a protective film of fluid at the surface which can contribute to the reduction of friction and wear.

5.3.3 Friction as a Function of Shear Velocity

In the last section it was seen that the kinetic friction coefficient obtained by the correlation of the tangential and normal forces, predicted quite well the experimental values. But will the friction coefficient be the same at different values of shear velocity? In the last predictions, a constant shear velocity of 4 m·s^{-1} was applied, i.e., a value 100 times higher than the one practiced experimentally. In this section, different values of shear velocity and load will be used, and the kinetic friction coefficient will be compared in the different conditions. The tested shear velocities correspond to 0.01 m·s^{-1} (experimental value), 2 m·s^{-1}, 4 m·s^{-1} and 15 m·s^{-1}. To each shear velocity, three values of load were applied, 1.6 nN, 6 nN and 14 nN. All simulations are at 500 K and the ionic liquid which was used in this analysis corresponds to [N_{1114}][C_4SO_3].

Figure 5.9a) represents the relation given in Equation 5.15, plotted at different average values of P_{xz} and P_{zz}, for different shear velocities and different loads. The average friction forces and normal forces at each value of load and shear velocity are given in Table 5.1, together with the coefficients P_0 and μ of the respective linear regressions.

When looking at the values of the internal load contribution — P_0 — it increases as the shear velocity also increases. The same is not valid for the friction coefficient, which surprisingly, is lower at 4 m·s^{-1} than at 2 m·s^{-1}. However, it is interesting to see that the values predicted by molecular simulations are not significantly different from the ones obtained experimentally, for the shear rates that are used in experiments.

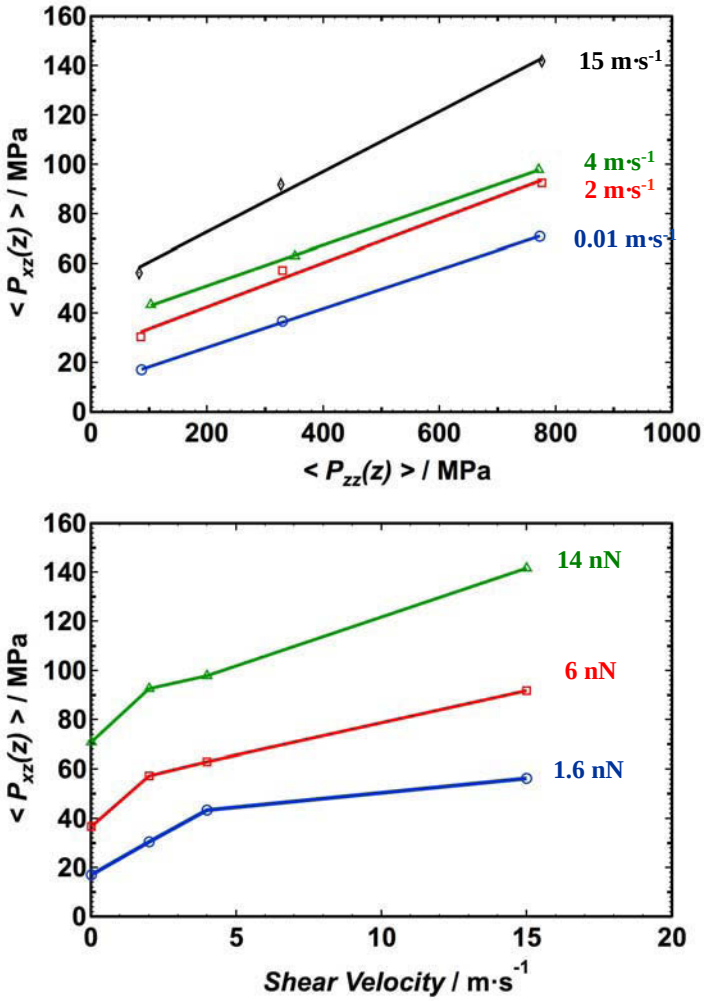

Figure 5.9: Behavior of the components of the pressure tensor with load and shear velocity: a) P_{xz} and P_{zz} profiles at 0.01, 2, 4 and 15 m·s ^{1}; b) dependence of P_{xz} with the shear velocity, for different applied loads.

The frictional force was plotted in function of the velocity of shear in Figure 5.9b), for three different values of applied load. This graph shows two features: P_{xz} increases with the applied load and with the shear velocity. In the first case, a higher applied load may signify an increase of the necessary force to maintain a continuous sliding. The same shear velocity dependence of P_{xz} were also found by other authors[8;60]. This is supposed to be associated to thermal activation at the interface, when the shear rate increases.

Table 5.1: $P_{zz}(z)$ and $P_{xz}(z)$ components of pressure tensor (Eq. 5.6), average friction coefficient (μ) and internal pressure (P_0) calculated using Eq. 5.15. Four shear velocities were applied to the systems: 0.01, 2, 4 and 15 m·s^{-1}, composed by the ionic liquid[N_{1114}][C_4SO_3] in contact with the rough surface of iron. Three values of load were tested at each shear velocity: 1.6, 6 and 14 nN.

Imposed load nN	$\langle P_{zz}(z)\rangle$ MPa	$\langle P_{xz}(z)\rangle$ MPa	P_0 MPa	μ
0.01 m·s^{-1}				
1.6	87	17		
6	330	37	10	0.078
14	772	71		
2 m·s^{-1}				
1.6	86	30		
6	330	57	25	0.089
14	776	93		
4 m·s^{-1}				
1.6	103	43		
6	351	63	35	0.082
14	771	98		
15 m·s^{-1}				
1.6	83	56		
6	327	92	48	0.122
14	776	142		

The static friction force, *i.e.*, the necessary force to initiate sliding for a given applied load, will be between 0 and the P_{xz} point where each one of these curves crosses the velocity axis at zero. As such, taking into account that 0.01 m·s^{-1} is the lowest simulated velocity, the static friction force for this system, at each one of the applied loads, will be always bellow the corresponding P_{xz} value at this velocity. One way to measure the static friction coefficient is to correlate the values of friction forces with time, in a MD simulation at the equilibrium (no shear applied), using a Green-Kubo relation[123]:

$$\mu = \frac{1}{Ak_BT}\int_0^\infty \langle F_x(t)\cdot F_x(0)\,dt\rangle \tag{5.17}$$

where A is the area of contact, k_B is the Boltzman constant, T is the temperature and F is the frictional force. Such approach will not be studied in the present work, but it will be the object of future investigations.

5.3.4 Friction as a Function of the Surface Topology

Two surface topologies, a flat and a rough surface, were studied in contact with the ionic liquid [N_{1114}][C_4SO_3]. The roughness was modeled by the introduction of two asperities with truncated cone geometry (see Figure 5.1).

The average components of the pressure tensor, the friction coefficient (μ) and P_0 are presented in Table 5.2, as a function of the load and surface topology. Friction and P_0 were obtained by linear regression in agreement with Eq. 5.15. The standard deviations for the measured variables of pressure are around 2% for $P_{zz}(z)$ and 10% for $P_{xz}(z)$, of the average values. The errors associated to the linear fit are represented in the table, for P_0 and μ. Simulations at different loads were performed with a constant shear velocity of 4 m·s^{-1}.

Table 5.2: $P_{zz}(z)$ and $P_{xz}(z)$ components of the pressure tensor (Eq. 5.6), average friction coefficient (μ) and internal pressure (P_0) calculated using Eq. 5.15, and associated errors. Results concern systems composed of: flat and rough iron surface in contact with the ionic liquid $[N_{1114}][C_4SO_3]$.

Imposed load nN	$\langle P_{zz}(z)\rangle$ MPa	$\langle P_{xz}(z)\rangle$ MPa	$P_0 \pm \varepsilon$ MPa	$\mu \pm \varepsilon$
Flat Surface				
1.6	85	30		
3	176	44		
6	335	58	20 ± 5	0.126 ± 0.013
10	554	96		
14	781	116		
Rough Surface				
1.6	103	43		
3	196	43		
6	351	63	31 ± 4	0.087 ± 0.012
10	576	82		
14	771	98		

In Table 5.2 it is interesting to observe that the friction coefficient of the flat surface ($\mu = 0.126$) is higher than that of the rough surface ($\mu = 0.087$). Explanations for that will be given next.

The normal and tangential components of the pressure tensor were plotted against the surface separation for the two types of surfaces in Figure 5.10. It can be seen that for the same surface separation, the normal component P_{zz} associated to the rough surface is lower than the one associated to the flat surface. This means that it is more difficult to approach two flat surfaces than two rough surfaces, which can be associated to the more ordered adsorbed layer at the flat metallic surface. From Figure 5.10, we can also conclude that the decrease of the friction coefficient with the roughness of the surface is mainly caused by the normal force and not by the weak change in the shear force.

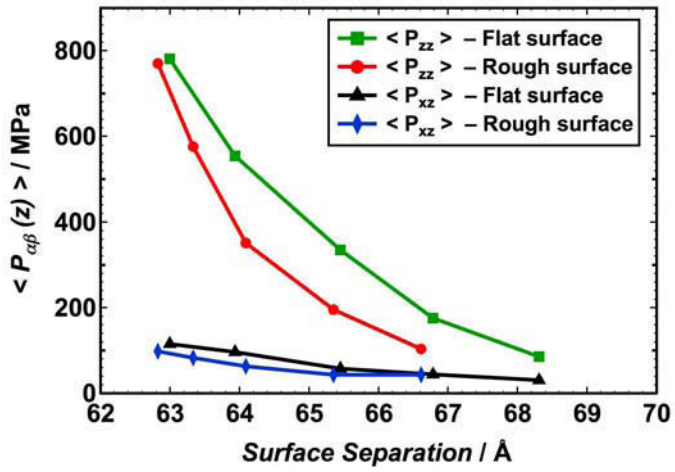

Figure 5.10: P_{xz} and P_{zz} components of the pressure tensor as a function of the surface separation, for two system with different surface topologies: rough and flat surfaces.

We expect to find an explanation to this behavior by analyzing the local density profiles of both systems. In Figure 5.11 you can find such profiles for systems composed by rough or flat surfaces, at the equilibrium (no shear) and under shear (shear). To make a direct comparison between the local density profiles in both flat and rough surfaces (once the surface volume is not the same in both surfaces), the volume occupied by the asperities was removed from the rough surface total volume, and the density of atoms in the interfacial layers in this case corresponds to density in the flat parts only.

The oxygen atoms (O) and the sulfur atom (S) are representative of the head group of the alkylsulfonate anion, the nitrogen atom (N) is representative of the positive head-group of the alkylammonium cation and, finally, the terminal carbon atoms (C_{3H}) represent the position of the longer alkyl chains in either anions or cations. The structure and labels given to each atomic site in this ionic liquid can be found in Figure 4.5.

In the graph corresponding to the flat surface at the equilibrium (Figure 5.11a) two layers of anion head-groups are observed, clearly marked by the peaks of S and O atoms. Logically, O atoms approach closer to the surface. Only one structured layer of cation head-groups is perceived through the strong peak of N atoms, at distances from the surface that are slightly larger than that of S atoms from

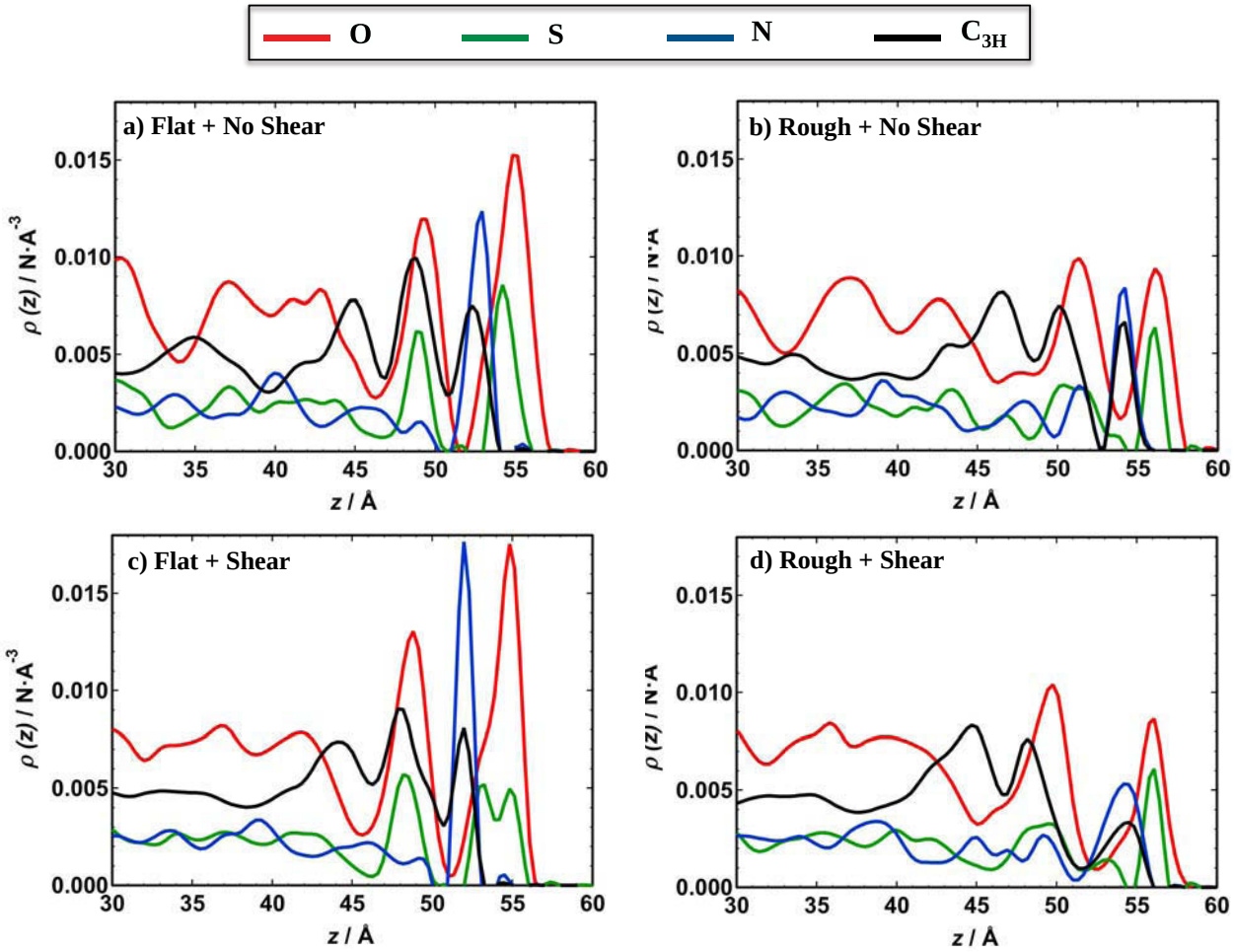

Figure 5.11: Atomic density profiles of O (red), S (green), N (blue) and C_{3H} (black) atoms, for the following systems: a) flat surface under zero shear; b) rough surface under zero shear; c) flat surface under a shear velocity of 4 m·s ^{1}; d) rough surface under a shear velocity of 4 m·s ^{1}. The systems under shear were also submitted to a constant load of 6 nN. Both surfaces were in contact with the ionic liquid $[N_{1114}][C_4SO_3]$.

the anion. Two peaks corresponding to the terminal C atoms of the alkyl side chains in the cation or the anion are also present and appear further away from the surface than the charged head-groups. The second peak of the C atoms at 49 Å is slightly higher than the one at 52 Å, indicating an ordering of the alkyl tails pointing away from the metal surface. This is characteristic of the segregation between the alkyl chains, which form non-polar regions[23]. In general, the interfacial layer of this ionic liquid is approximately 10 Å thick and it is composed of anion and cation head-groups separated by 2 Å, and a second, less-ordered layer of anions. The corresponding system under shear is represented in Figure 5.11c. Here, the intensity of the O and N atoms increases, as a result of the applied load in the normal direction. The position of the peaks is maintained. From the velocity profiles, we observe that the region of the constant velocity along $z-$axis corresponds to that of the two layers of anion head groups indicating a strong interaction with the surface under shear.

Concerning the system with rough surfaces (Figure 5.11b), the main difference in terms of local density profile from the system discussed above is a reduction in the height of the peaks and in the molecular ordering at the interface. Furthermore, when shear is applied (Figure 5.11d), a decrease in the intensity of all peaks corresponding to the cation-anion layer closer to the surface is observed. These findings may be associated with the lower friction for this last system when compared to the one with the flat surface. The ordering of the adsorbed film of fluid at the interface in the case of the flat surface seems to be more significant than for the rough surface system, which can have some influence on friction.

The orientation of the alkyl side chains in the anion or the cation with respect to the metallic surface was analyzed with the aid of a Legendre polynomial function (see section 4.2.4). Figure 5.12 presents the orientations of the alkyl side chains in the cation (blue curves) and the anion (red curves) for the ionic liquid $[N_{1114}][C_4SO_3]$ in contact with flat and rough surfaces. In the orientational ordering parameter ($P_2(\theta)$), θ is the angle between the surface normal and a vector chosen in the ion. In the present ionic liquid, both cation and anion are composed of an essentially spherical head-group (trimethylammonium and sulfonate) and an alkyl side chain, therefore the vector representing the orientation of the ions was defined between a central atom of the cation or anion head-group, i.e. N or S, and the terminal atom of the respective alkyl side chain, i.e. C_{3H}.

For the flat surface the first peaks of the anion correspond to an orientation of the alkyl tails that is essentially perpendicular to the metal surface, after which the orientation becomes random and $P_2(\theta)$ decays to zero as expected for bulk configurations. In the case of the cation, the alkyl side chains closer to the surface have a parallel orientation for $\sim$ 2 Å, after what it becomes perpendicular. This means that the alkyl chains of the first layer of cations and anions have different orientations towards the surface.

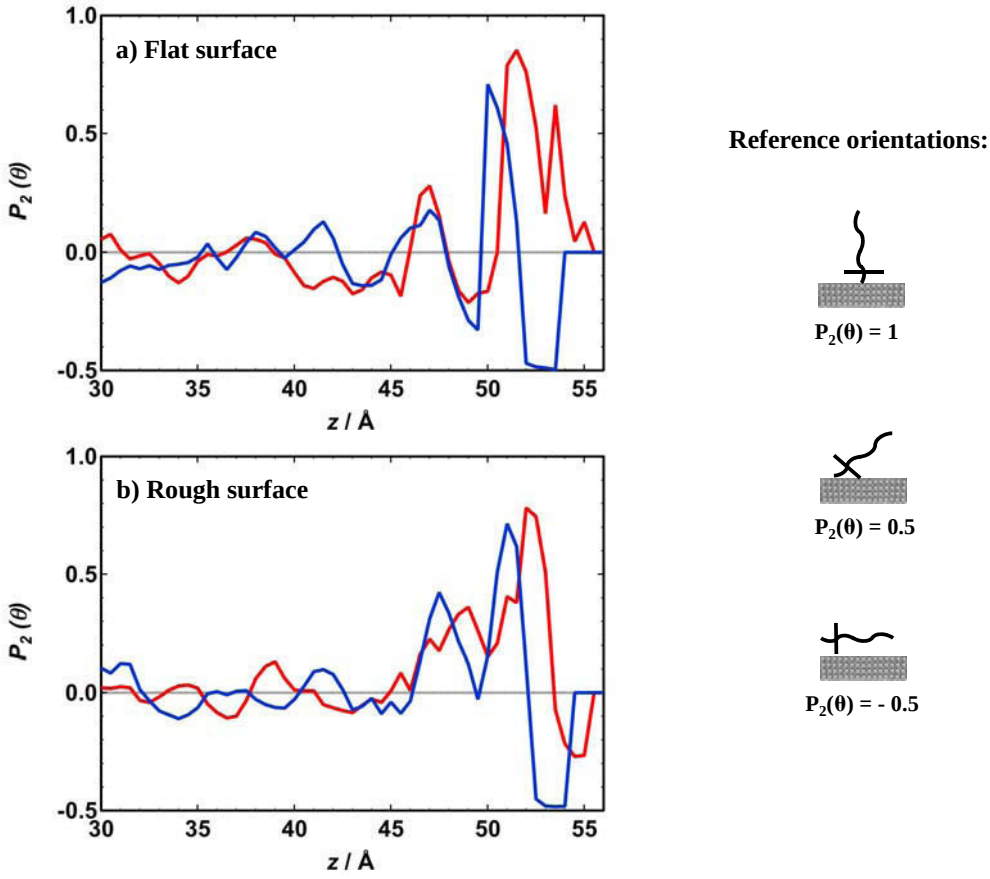

Figure 5.12: Orientational ordering parameter, $P_2(\theta)$, for the ionic liquid $[N_{1114}][C_4SO_3]$ in contact with a) flat surface and b) rough surface. The red curves represent the orientation of the anions and the blue curves those of the cations. The reference orientation of the alkyl side chains is illustrated in the figure.

This behavior differs in the rough surface. Actually, the cation and the anion side chains are in phase with each other and adopt the same orientation at the interface, i.e., they are parallel for the layers closer to the surface and perpendicular afterwards. The fact that they have the same orientation can promote the segregation of the alkyl tails and create non-polar domains at the interface, which may promote sliding. Experimentally, it is known that the increase of the number of carbons in the alkyl tails reduces the friction coefficient.

5.3.5 Friction as a Function of the Ionic Liquid Structure

In the last three sections we have studied the behavior of friction as a function of load, temperature, shear velocity and surface topology. One last condition will be here tested, which is the structure of the ionic liquid and in what that can influence friction.

For this purpose, friction was measured for five ionic liquids interacting with a rough iron surface. Results are presented in Table 5.3, where friction and P_0 were obtained by linear regression in agreement with Eq. 5.15. As a complement to Table 5.3, Figure 5.13 presents the tendency of the kinetic friction, going from the ionic liquid with the lowest friction ($[N_{1114}][C_4SO_3]$) to the one with the highest friction value ($[N_{1124}][C_4SO_3]$).

When looking to the structures of $[N_{1114}][C_4SO_3]$ and $[N_{1114}][C_1SO_3]$ one expects that the friction coefficient increases with shorter alkyl side chains. It is known that as the alkyl side chain of the lubricant increases, friction decreases[30]. However, the same reasoning is not valid when going from $[N_{1114}][C_4SO_3]$ to $[N_{1124}][C_4SO_3]$ or $[N_{1114}][C_8SO_3]$, where the friction coefficient increases, although the number of total carbon atoms passes from 11 to 12 and 15, respectively. Therefore, increasing the anion alkyl side chain is not conclusive with respect to an increase/decrease of the kinetic friction. Also, taking into account the associated error, μ is quite close for the different ionic liquids. Nevertheless, one can assume that an increase in the alkyl side chain of the cation induces a higher friction coefficient, so much that the ionic liquid with an ethyl group in the cation head group – $[N_{1124}][C_4SO_3]$ – corresponds to the structure with the highest friction coefficient.

Table 5.3: Components of the pressure tensor (Eq. 5.6), average friction coefficient (μ) and internal pressure (P_0) calculated using Eq. 5.15, and associated errors. Results concern five ionic liquid structures in contact with the rough surface.

Imposed load nN	$\langle P_{zz}(z)\rangle$ MPa	$\langle P_{xz}(z)\rangle$ MPa	$P_0 \pm \varepsilon$ MPa	$\mu \pm \varepsilon$
$[N_{1114}][C_4SO_3]$				
1.6	103	43		
3	196	43		
6	351	63	31 ± 4	0.087 ± 0.012
10	576	82		
14	770	98		
$[N_{1114}][C_1SO_3]$				
1.6	58	26		
3	149	38		
6	341	65	21 ± 4	0.106 ± 0.017
10	525	73		
14	747	102		
$[N_{1124}][C_4SO_3]$				
1.6	94	37		
3	186	58		
6	296	50	22 ± 8	0.144 ± 0.018
10	576	110		
14	794	136		
$[N_{1114}][C_8SO_3]$				
1.6	86	20		
6	315	39		
10	527	67	10 ± 4	0.104 ± 0.016
14	736	91		
20	1052	131		
$[N_{1114}][NTf_2]$				
1.6	90	21		
3	177	31	9 ± 2	0.117 ± 0.010
6	327	44		
14	766	100		

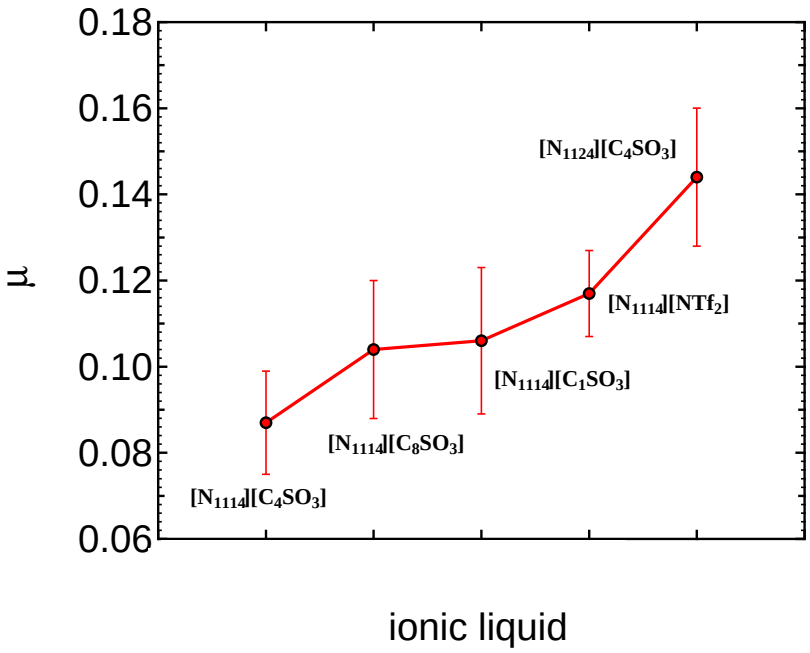

Figure 5.13: Kinetic friction tendency curve. The ionic liquid with the lowest friction coefficient is $[N_{1114}][C_4SO_3]$ (μ =0.087).

Then, when passing from the family of the ionic liquids based on sulfonate anions to the family based on the bistriflamide anions, the coefficient of friction increases. The fact that the anion in the former case has no alkyl side chain, can be at the origin of this behavior. In fact, it is known that the structural properties in the anion influence more significantly the tribological performance of the ionic liquid, when compared to the influence of the cation structure. From the discussion of chapter 4, we have learned that the NTf_2^- anion has a position parallel to the surface so that all the oxygen's atoms can interact with iron. Plus, both anion and cation species are found in the same layer close to the surface, creating a charge ordering of only one layer.

In order to understand the role of the alkyl side chains in the friction coefficient of the family of ionic liquids based on sulfonate anions, the orientational ordering parameter – $P_2(\theta)$ – was plotted in Figure 5.14. The graph concerning the ionic liquid $[N_{1114}][C_4SO_3]$ (Figure 5.14a) has already been discussed in Figure 5.12b but it is also given here for a more direct comparison with the other three ionic liquids:

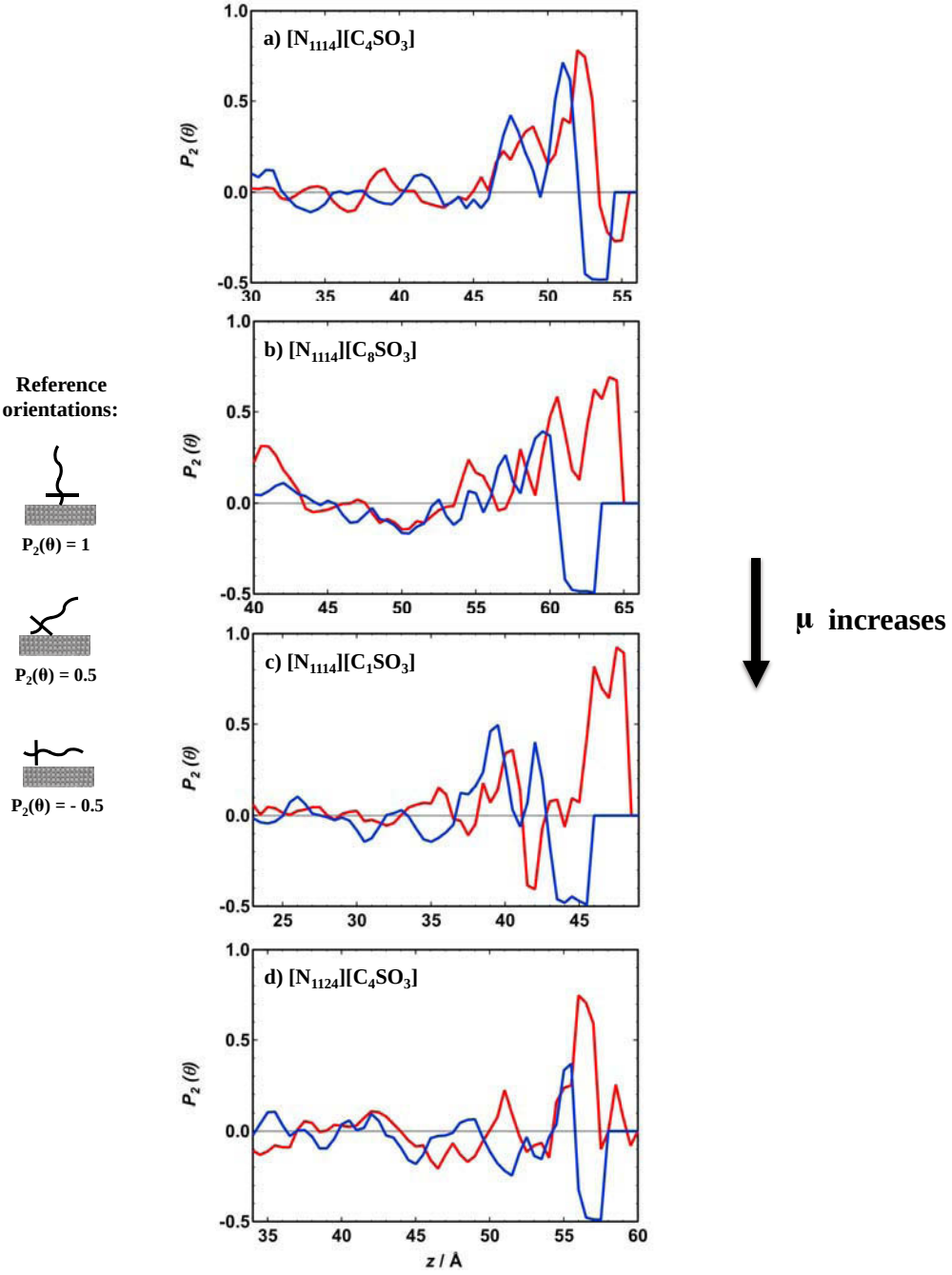

Figure 5.14: Orientational ordering parameter $P_2(\theta)$, for the ionic liquids a) $[N_{1114}][C_1SO_3]$; b) $[N_{1114}][C_8SO_3]$; c) $[N_{1114}][C_1SO_3]$ and d)$[N_{1124}][C_4SO_3]$ in contact with a rough surface. The red curves represent the orientation of the anions and the blue curves those of the cations. The reference orientation of the alkyl side chains and the trend of the friction coefficient are represented in the figure.

$[N_{1114}][C_1SO_3]$, $[N_{1124}][C_4SO_3]$ and $[N_{1114}][C_8SO_3]$.

Figure 5.14 clearly establishes that the changes in the friction coefficient are also accompanied by changes in the orientation of the ionic liquid close to the surface. Firstly, when the layer closer to the surface is populated by parallel orientations, the friction coefficient is smaller (see Figure 5.14a). In opposite, when groups that are rather perpendicular to the surface occupy the first layer, the friction coefficient is higher (see Figure 5.14d). The difference between friction coefficients of parts c) and d) of Figure 5.14 may be explained by the ionic liquid $[N_{1124}][C_4SO_3]$ showing two different orientations in the same layer, which is not the case for $[N_{1114}][C_1SO_3]$, where the alkyl chains of cation and anion, although oriented in opposite senses, occupy different layers at the surface. In the ionic liquid with the octyl side chain (see Figure 5.14b), the two first layers of anion alkyl side chains make an angle of about 45° with the surface and the cation alkyl side chain has a parallel position.

As already discussed before, in the ionic liquid $[N_{1114}][C_4SO_3]$ (Fig. 5.14a), the cation and the anion alkyl chains are in phase with each other in the two layers close to the surface, a feature which can promote the segregation of the non-polar domains and decrease the friction coefficient of this last ionic liquid.

5.4 Summary

The method used here to calculate the components of the pressure tensor has already been applied to measure the friction coefficient of grafted polymer chains with coarse grain models[124] and with dissipative particle dynamics approach[125]. Nevertheless, such methods have not been widely applied with atomistic models due to the difficulty of calculating the pressure tensor with electrostatics in a two-dimensional simulation cell under shear.

Here we report a strategy to calculate accurate friction coefficients of ionic liquids interacting with surfaces, based on the calculation of the tangential and normal components of the pressure tensor in a two-slab geometry. We mimic the experimental conditions by performing non-equilibrium molecular dynamics simulations under a constant load and by moving one of the surfaces at constant velocity. The thermal and mechanical equilibria are checked locally by plotting profiles of the temperature and

pressure tensors along the direction where the heterogeneity takes place.

Once the methodology was developed, we have investigated the dependence of the frictional forces on the load, temperature, shear velocity, surface topology and nature of the ionic liquid. The simulated friction coefficients are in good agreement with the available experimental data, establishing our methodology as a quantitative method for the prediction of friction.

The ionic liquid $[N_{1114}][C_4SO_3]$ was studied in contact with both flat and rough surfaces of iron. The molecular simulations predict a decrease in the friction when the ionic liquid interacts with the rough surface. This was interpreted in terms of the specific distribution of the charged groups of the ionic liquid and of the orientational order of the alkyl side chains close to the surface. A higher charge ordering in the interfacial layer seems to decrease the ability of the surface to slide and to promote higher friction coefficients. Besides, as the alkyl side chain in the anion increases, the orientation of both species tends to become parallel to the surface, which can promote the segregation of the alkyl side chains and facilitate sliding. The friction coefficient in this last case will be lower.

We have also explained the difference in the friction coefficients of several ionic liquids by exploring the orientations of the anions and cations close to the surface.

CHAPTER 6

Adding Water to the Ionic Liquid–Iron System — Preliminary Results

6.1 Scope of the Chapter

In the present chapter, a water-iron interaction model is build from first principles, using the same approach described in chapter 4 for the ionic liquid–iron interaction. Then, water will be introduced into the IL-metal MD simulations, at equilibrium and non-equilibrium conditions. The structure at the solid-liquid interface is expected to change when water is added to the system. Furthermore, the lubricant performance is known to decrease in humid conditions. The objective of this chapter is to provide some preliminary results on the structure at the interface when water is present in the system and to estimate the possible effects that it can have on the friction coefficient.

One of the most interesting properties of ionic liquids, is their ability to dissolve a large variety of compounds, associated to the existence of polar and non-polar moieties in the ionic liquids. ILs can be soluble in water and in polar base lubricants, allowing their application as lubricating additives. Water can also be present as a contaminant in the pure ionic solutions, influencing their thermo-oxidative stability. This aspect is even more significative if the constituent ions are hydrophilic. Furthermore, water can also play a role in the corrosion of the metallic surface, because in presence of the sulfonate

anion there can be the formation of species such as sulfonic acid (RSO_3H) and sulfuric acid (H_2SO_4) that can corrode the metallic surface.

Water can also play a role in the adhesive forces at the surface, known to increase with the relative humidity. In fact, if the surface is hydrophilic a rapid adsorption of water molecules will occur. In several ionic liquids including the present ones, the presence of water increases the friction coefficient. This can be associated to a greater resistance to slide due to the strong attractive forces between the surface and the ions in the ionic liquid and also between the surface and water.

6.2 Methods

6.2.1 Force Field Description

With the addition of water to the system, there are three extra contributions to the total potential energy (Eq. 4.1) that need to be taken into account. They are associated to the interaction between ionic liquid and water (IL–water), the interaction between water molecules (water–water) and the interaction between water and the metal surface (M–water).

The most common classical force field models for water are of the type Lennard-Jones plus point charges, therefore compatible with the force field used here for the ionic liquids. For water, a modified single point charge model extended with a polarization correction was used (MSPC/E)[126]. The SPC/E model is composed of one single LJ site centered on the O atom and three point charges, one negative placed on the O and two positive placed on the locations of the H atoms. The geometry is defined by the O−H distance and by the H−O−H angle. The parameters are given in Table 6.1.

A potential model for water-iron interactions was build following the same approach used in chapter 4. By calculating the energy between one water molecule and a cluster of iron at different distances and orientations between the fragment and the cluster, using the same DFT methods as described in chapter 4. As such, the density functional MO6-L was employed with a TZVP[101] basis set for the water molecule, and for iron an ECP10MHF basis set from the Stuttgart/Cologne group[102]. The basis

set superposition error was corrected through the counterpoise (CP) technique [109].

Table 6.1: Parameters of the MSPC/E water model model used in this work.

Parameter	**Value**
r_{OH} (Å)	0.9839
Angle HOH (deg)	109.47
q_{H} (e)	0.4108
q_{O} (e)	-0.8216
$\varepsilon_{\mathrm{OO}}$ (kJ·mol ^{1})	0.61943
σ_{OO} (Å)	3.116

Four orientations of a water molecule were studied at a series of distances from a (001) bcc cluster of iron, containing 17 atoms. The potential energy between the different water orientations and the metal cluster is shown in Figure 6.1, where the points represent DFT energy calculations and the lines represent a fitting with the site-site-potential function of Eq. 4.7.

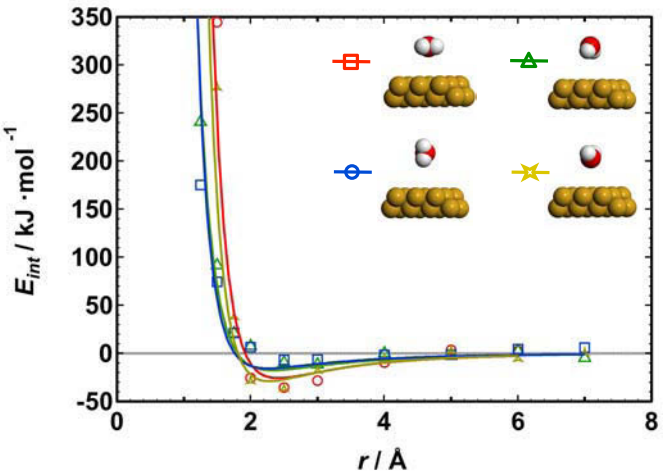

Figure 6.1: Interaction energy for a molecule of water at a series of distances and orientations from a 17-atom cluster of Fe(001).

As expected, the orientations where the oxygen atoms are directed towards the metal surface (yellow and red) are the ones having the larger binding energy. The orientations were the hydrogen atoms are directed towards the metal (blue and green) show weaker binding.

The parameters E_0, r_0, n and m from Eq. 4.7 obtained by the fitting are summarized in Table 6.2. All three atoms of the water molecule are considered as interaction sites with each atom of Fe.

Table 6.2: Parameters of interaction to be introduced into the MD simulation code, for system containing water in contact with a surface of Fe.

Fragment	**Site**	**E_0 (kJ mol^{-1})**	**r_0 (Å)**	**n**	**m**
H_2O	H	0.05	3.9	6	7
	O	6.98	2.5	6	5

6.2.2 Simulation Conditions

Two hundred pairs of ions of the ionic liquid 1-butyl-1,1,1-trimethylammonium metanesulfonate $[N_{1114}][C_1SO_3]$ were simulated between two surfaces of bcc iron composed of 1572 Fe atoms each. Water was added to the system in a 1:2 (water : ion pair) proportion, which corresponds to a mass fraction of water of 4%. The simulation box is a rectangular parallelepiped of dimensions $L_xL_yL_z$ ($L_x = L_y = 44$ Å, $L_z \approx 121$ Å) with periodic boundary conditions applied in the three dimensions.

The LAMMPS molecular dynamics package [118] was used to perform the simulations. The initial configuration was a low-density lattice containing the ionic liquid, the water molecules and the surfaces of iron that was equilibrated in the microcanonical ensemble (NVE) from 0 K to 500 K, by small temperature increments. Then, the surfaces of iron were brought together by applying a constant velocity to the upper surface, in the $-z$ direction, in order to obtain a correct density for the bulk liquid.

An equilibrium simulation was then performed over 2.0 ns with a time step of 1 fs, at constant NVT coupled with a Langevin thermostat. After, non-equilibrium simulations were executed over 1.5 ns,

by imposing a continuous shear velocity of 4 m·s^{-1} along the x direction, to the Fe rigid region of the upper surface, while keeping the Fe rigid region of the bottom surface fixed (more details on the geometry of the system under shear consult section 5.2). At the same time shear occurred, a constant force (F_z) was applied in the $-z$ direction to the sheared region. Four non-equilibrium simulations were performed, at 3, 6, 10 and 14 nN, which correspond to a nominal pressure of 166, 333, 555 and 776 MPa, respectively.

Long-range electrostatic interactions were handled through the particle-particle particle-mesh solver[119] (P3M) with a relative accuracy of 0.0001 in the calculation of the interaction energy and a real-space cut-off of 14 Å. In order to apply the three-dimensional P3M method in a slab geometry using the 3D periodic boundary condition, the dimension of the simulation box was increased along the z-axis by placing 30 Å of empty space on the external sides of each surfaces[69].

All C−H bonds of the ionic liquid; H−O bond and HOH angle in the water molecules and the Fe−q bonds between each atom of iron and the drude dipoles, were constrained using the SHAKE algorithm. Trajectories of all atoms were stored every 500 steps during the course of the simulation

6.3 Results and Discussion

In order to gain insights on the order and interactions occurring at the metal–ionic liquid–water interface, the number-density profiles for atoms of $[N_{1114}][C_1SO_3]$ and water were plotted in Figure 6.2. The oxygen atoms (O) and the sulfur atom (S) are representative of the head group of the alkyl-sulfonate anion, the nitrogen atom (N) is representative of the positive head-group of the alkyl-ammonium cation and the terminal carbon atoms (C_{3H}) represent the position of the longer alkyl chains in either anions or cations.

It can be seen that the water molecules form a well defined layer close to the surface. This is evidenced by the presence of the O_{water} and H_{water} atoms. In the same layer, O and S atoms of the anion head-group are also found. The cation head group forms a second layer at the surface, and this species

can establish electrostatic interactions with the oxygens of the anion and also ion-dipole interactions with the water molecules. The most probable distance between the first layers of anion and cation head-groups is of 2 Å, the same distance observed in the systems without water, discussed in chapter 4. A second layer of anions is found at 41 Å, a behavior also found in the systems with no water, for this ionic liquid.

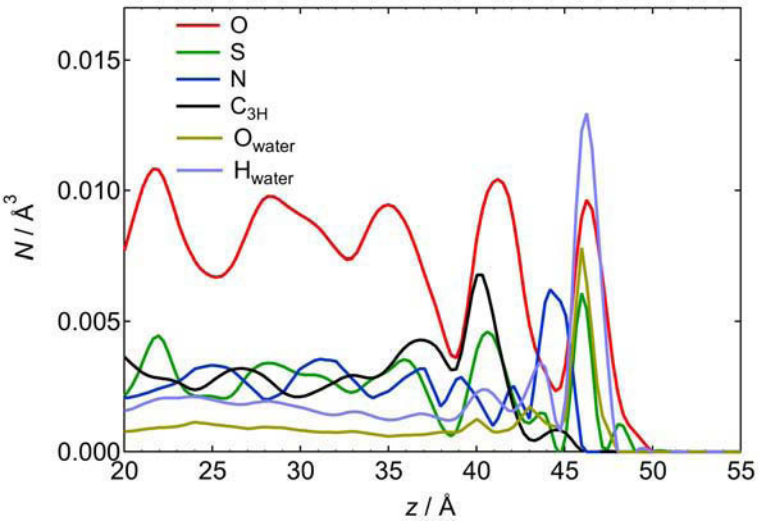

Figure 6.2: Atomic density profiles at the metallic surface for a mixture composed of ionic liquid and water.

Figure 6.3 presents a color-label snapshot of the interfacial layer, where it is clear that the water molecules are occupying the first layer close to the surface, together with the anion head groups.

Ion-dipole interactions can occur between the ions and the water molecules. Figure 6.4a) shows the site-site radial distribution functions (RDFs) for the N atom of the cation and the oxygens of both anion (N−O) and water (N−O_{water}). It can be seen that the probability of interaction between the cation and both oxygens is almost the same and occur at the same distance in the solvation shell. This correlation extends for a large distance.

Furthermore, hydrogen bonds (H-bonds) are established between atoms in the ionic liquid and wa-

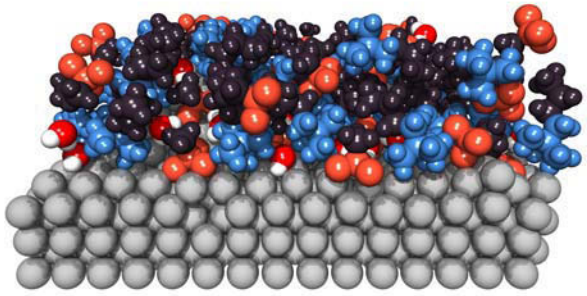

Figure 6.3: Snapshots of the metal–ionic liquid–water interface using color labeling. Orange, blue and black colors depict the sulfonyl head-groups of anions, ammonium head-groups of cations, and alkyl chains of both ions, respectively. The oxygen atoms of the water molecules are labeled in red and the hydrogen's in white.

ter. The ability of phase of an ionic liquid to form hydrogen bonds can influence the structure and properties of the liquid phase. Figure 6.4b) shows the site-site RDFs corresponding to the correlation between the N atoms of the cation and the hydrogens of water (N$-$H$_{\text{water}}$) and between the O atoms of the anion head-group and the hydrogen atoms in the water molecules (O$-$H$_{\text{water}}$). The graph shows the presence of hydrogen bonds between the signed sites, with the H-bonds between the anion and the hydrogens of water happening first.

The friction coefficient was determined using the method described in Chapter 5, section 5.2.3, which allows calculating the normal and tangential forces from a definition of pressure measured locally. Figure 6.5 presents the average values of P_{xz} and P_{zz}, where each point represents an isolated simulation at a given load, using a constant shear velocity of 4 m·s^{-1}. The values of P_{xz} correspond to frictional forces and the values of P_{zz} to forces applied in the normal direction.

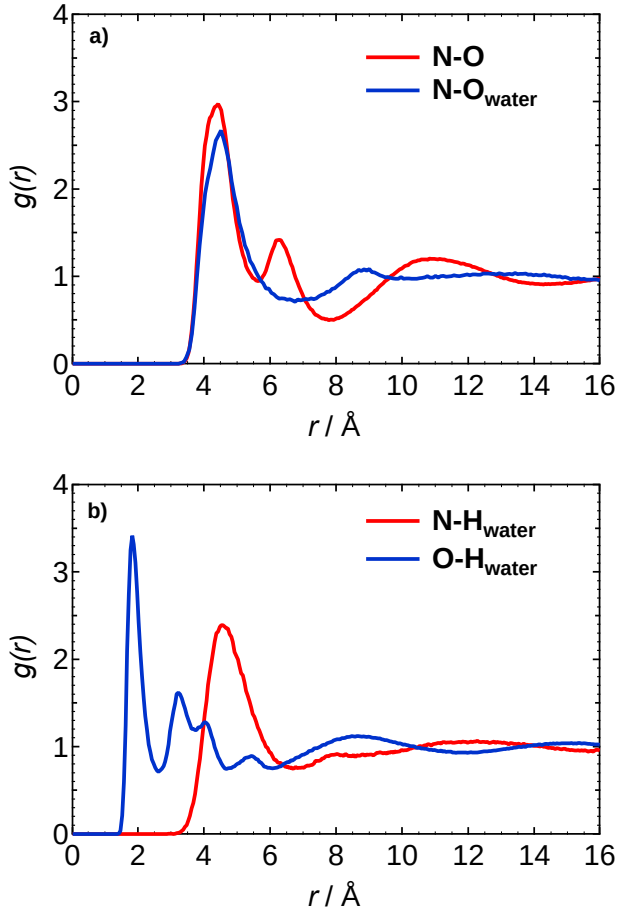

Figure 6.4: Site-site radial distribution functions for the: a) cation–oxygens of the anion (N−O) and cation-oxygens of water (N−O_{water}) interaction and b) H-bond formation between the cation and the hydrogens of water (N−H_{water}) and between the oxygens of the anion and the hydrogens of water (O−H_{water}).

In agreement with Eq. 5.15, the slope of this curve corresponds to the kinetic friction coefficient (μ). Results are presented in Table 6.3. For comparison, results corresponding to the ionic liquid alone are also present. This last ones were already presented in chapter 5.

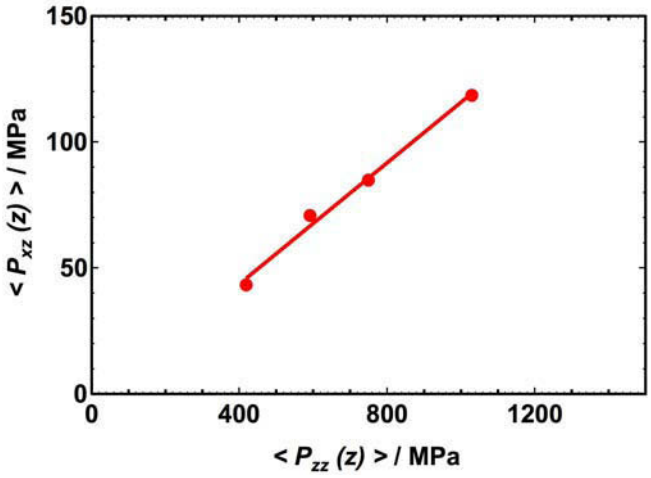

Figure 6.5: Frictional forces P_{xz} as a function of the normal forces P_{zz}

Table 6.3: Components of pressure tensor (Eq. 5.6), average friction coefficient (μ) and internal pressure (P_0) calculated using Eq. 5.15, for the ionic liquid $[N_{1114}][C_1SO_3]$ in the presence of water and without water.

Imposed load nN	$\langle P_{zz}(z)\rangle$ MPa	$\langle P_{xz}(z)\rangle$ MPa	P_0 MPa	μ
$[N_{1114}][C_1SO_3]$				
1.6	57	25		
3	141	35		
6	348	73	22	0.112
10	515	77		
14	723	101		
$[N_{1114}][C_1SO_3] + H_2O$				
3	418	43		
6	591	71	–4	0.120
10	750	85		
14	1030	118		

Fig. 6.2 showed that both anion and water molecules are adsorbed at the surface. An increase of the adhesive forces at the surface can be reproduced in a more difficulty to slide. Such behavior is most

probably associated with the higher friction coefficient found experimentally for these ionic liquids under humid conditions and also confirmed here by simulation. The negative value of P_0 for the system with water is an interesting result an it can be associated to the enhanced adsorption at the surface.

6.4 Summary

In the present chapter, a model was build from quantum chemical calculations for the water–iron interaction, including the polarization of the metal surface. Water molecules were introduced in a pure solution of the ionic liquid $[N_{1114}][C_1SO_3]$, in a 1:2 (water: ion pair) proportion. Results obtained from the MD simulations were analyzed.

The water molecules tend to occupy the layer adjacent to the metal surface, together with the anion head-groups. The great affinity between the oxygen atoms and iron is at the origin of such behavior. In the presence of water there is an increase of the adhesive forces at the surface, that can be at the origin of the rise in the friction coefficient with water content.

Further analysis will be made in systems composed of water and ionic liquid in contact with a metal surface and parameters such as the concentration of water in solution, the alkyl side chain length and the nature of the anion will be evaluated in the future.

CHAPTER 7

Conclusions

7.1 Summary of thesis achievements

As already known experimentally, the structure, interactions and molecular ordering of ionic liquids at the surface of metals or graphene are complex to describe. They depend on many factors including the surface charge, the chemical structure of both cation and anion species, the nature of the surface and its polarizability, the affinity between the liquid and the surface, the viscosity of the ionic liquid, among others.

Molecular dynamics simulations can assist in the description of the interfacial structure and help to gain molecular insights about the behavior of an ionic liquid in contact with a surface. However, the validity of such results are dependent on the accuracy of the force-field used in the description of the metal–ionic liquid interactions. In the present work, we have chosen to build an interaction model from first principles for the iron-ionic liquid interactions, which takes into account not only dispersion-repulsion forces but also electrostatic forces arising from the polarization of the metal by the ions. In fact, the correct representation of the metal charge fluctuations is dependent of the nearby liquid structure, and the representation of the liquid structure itself, is also dependent on the metal

polarizability.

The construction of this interaction model represents one of the main achievements of the present work and constitutes the starting point to the numerous molecular dynamics simulations of the ionic liquids confined between surfaces of iron. When combined with a molecular force field for the ionic liquid and a suitable potential for metals, our model allows the computer simulation of heterogeneous systems containing metal surfaces or nanoparticles in the presence of ionic liquids. Our specific treatment of the interactions between the sites of the ionic liquid and the metal surface, and including polarization of the conductor, produces a more reliable representation of the interactions than is possible using existing empirical and non-polarizable force field models. An article[127] was published in the main journal of the field.

Studies at equilibrium and non-equilibrium were performed, to evaluate the interfacial properties of a new class of ionic liquids and their lubricant performance when shear is applied to the system. The ionic liquids studied herein as potential lubricants are a new class of fluids composed of alkylammonium cations combined with different anions based in alkylsulfonate and bistriflamide. These structures were chosen due to their suitable ecotoxic and biodegradable properties and appropriate tribological characteristics. Different combinations of anions and cations were obtained by choosing the type of anions or by having different lengths in the alkyl side chains.

Results of the simulations at equilibrium conditions pointed towards a high affinity of the oxygen atoms of both alkylsulfonate and bistriflamide anions for the iron surface. For the ionic structures based in the alkylsulfonate anions with different alkyl side chain lengths, it was observed that the oxygens in the head-group of the anion occupy the layer adjacent to the metal walls, followed by the head-group of the alkylammonium cations. The interfacial layer was found to be essentially one ion thick (Helmholtz type) in result of the electrostatic screening of the ionic medium, in agreement with experimental results from the literature. The orientation of the nonpolar alkyl side chains on the cation and the anion are different: whereas butyl chains on the sulfonate anions tend to be directed away from the surface, those on ammonium cations lie more parallel to the surface.

The tribological behavior of the ionic liquids was evaluated in terms of the kinetic friction coefficient. For that, we have developed a procedure for a quantitative prediction of the frictional forces in terms of the local measurement of the components of the pressure tensor. Such technique has not been widely applied with atomistic models due to the difficulty of calculating the pressure tensor with electrostatics in a two-dimensional simulation cell, under shear. The results shown a linear dependence between the frictional force and the normal force for all the systems studied, and the friction coefficient was obtained as the slope of such regression. The obtained values of friction coefficient agree very well with the available experimental ones, establishing our methodology as a quantitative method for the prediction of friction. We have investigated the dependence of this quantity with load, temperature, shear velocity, surface topology and nature of the ionic liquid. The friction coefficient was found to be associated with the charge ordering at the surface. Therefore, a higher charge ordering in the interfacial layer seems to decrease the ability of the surface to slide and to promote higher friction coefficients. Besides, the orientation of the alkyl side chains in both cation and anion play an important role in the results of friction, since when the orientation of both species was parallel to the surface, the friction coefficient decreased. This is probably associated to the segregation of the alkyl side chains at the interface, which according to experimental results, facilitates the sliding and decreases the friction coefficient. An article was accepted reporting these results [128].

Finally, the interfacial layer of the ionic liquids at the metal surface was described in the presence of water molecules. Water is known to decrease the lubricating performance of the ionic liquids and to influence the corrosion of the metallic surface. Therefore the importance of characterizing the interactions occurring between water–ionic liquids, and water–iron. For that, a model was build from quantum chemical calculations to accurately describe the water–iron interactions, including the polarization of the metal surface, using the same approach used in the construction of the ionic liquid–iron interaction potential. MD results have shown that the water molecules tend to occupy the layer adjacent to the metal surface, together with the anion head-groups. Such behavior can be at the origin of a higher friction coefficient found experimentally and here by simulations, using the same procedure descried previously for the calculation of the friction coefficient.

In the present work we have shown that structure and dynamics of the ionic liquids at the interfa-

cial layers are different from the bulk phase. The complexity of the liquid–metal interactions and the relationship between structure and rheological properties is far from being completely understood. However, the methodologies developed here for the accurate description of the interactions occurring between ionic liquids and iron, together with the strategy built to predict the kinetic friction coefficients, represent a step toward a better understanding of the origin of the lubricant properties of ionic liquids.

The model developed here for the ionic liquid–iron interaction is of atom-atom type and therefore it is independent of the surface topology (it can be used to represent flat or rough surfaces) and conformation of the ions. It can be combined with existing force-field models for ionic liquids and for metallic materials in order to simulate different heterogeneous systems.

The elements of information obtained here, which concern the structure of the ionic liquids at metal surfaces, can contribute to improve the knowledge of tribological or electrochemical systems using these fluids.

The methodology developed for the rheological properties determination can be used in different heterogenous systems for the determination of the friction coefficient.

7.2 Future Work

Further developments on the systems composed by ionic liquid, iron and water will be performed at different water concentrations and using other ionic liquids structures. The reproduction of the Stribeck diagram is a future aim, together with the prediction of the shear viscosity for these ionic liquids. The origins of static friction for these systems has already started to be investigated and a technique for such determination is in the course of development. The study of other surfaces than iron, such as carbon-based structures, is being carried out using the same methodologies described here.

List of Figures

List of Tables

Bibliography

[1] B. N. J. Persson, *Sliding Friction: Physical Principles and Applications*. Berlin: Springer-Verlag, 1998.

[2] P. T. Anastas and J. C. Warner, *Green Chemistry: Theory and Practice*. New York: Oxford University Press, 1998.

[3] B. Bhushan, *Principles and Applications of Tribology*. New York: John Wiley and Sons, 1st edn ed., 1999.

[4] D. Downson, *History of Tribology*. London: Longmans, 1979.

[5] G. Amontons, "De la resistance causée dans les machines," *Memoires de l'Academie Royale A*, pp. 257–282, 1699.

[6] F. P. Bowden and D. Tabor, *Friction and Lubrication of Solids*. Oxford: Clarendon, 1950.

[7] H. Yoshizawa, Y. L. Chen, and J. N. Israelachvili, "Fundamental mechanisms of interfacial friction. 1. relation between adhesion and friction," *The Journal of Physical Chemistry*, vol. 97, no. 16, pp. 4128–4140, 1993.

[8] G. He, M. H. Müser, and M. O. Robbins, "Adsorbed layers and the origin of static friction," *Science*, vol. 284, no. 5420, pp. 1650–1652, 1999.

[9] M. O. Robbins and M. H. Müser, *Modern Tribology Handbook*, ch. Computer simulations of friction, lubrication, and wear, pp. 717–765. Boca Raton: CRC Press, 2001.

[10] B. Derjaguin, "Analysis of friction and adhesion IV The theory of the adhesion of small particles," *Kolloid-Zeitschrift*, vol. 69, no. 2, pp. 155–164, 1934.

[11] J. N. Israelachvili and A. D. Berman, *Handbook of Micro/Nanotribology*, ch. Surface Forces and Microrheology of Molecularly Thin Liquid Films, pp. 371–432. Boca Raton: CRC Press, 1999.

[12] Gao, Jianping and Luedtke, W. D. and Gourdon, D. and Ruths, M. and Israelachvili, J. N. and Landman, Uzi, "Frictional Forces and Amontons Law," *The Journal of Physical Chemistry B*, vol. 108, no. 11, pp. 3410–3425, 2004.

[13] B. J. Hamrock, S. R. Schmid, and B. O. Jacobson, *Fundamentals of Fluid Film Lubrication*. CRC Press, 2004.

[14] J. N. Israelachvili and P. M. Mcguiggan, "Forces between surfaces in liquids," *Science*, vol. 241, no. 4867, pp. 795–800, 1988.

[15] C. Drummond and J. N. Israelachvili, "Dynamic behavior of confined branched hydrocarbon lubricant fluids under shear," *Macromolecules*, vol. 33, no. 13, pp. 4910–4920, 2000.

[16] M. Gee, P. M. Mcguiggan, J. N. Israelachvili, and A. Homola, "Liquid to Solid-Like Transitions of Molecularly Thin-Films Under Shear," *Journal of Chemical Physics*, vol. 93, no. 3, pp. 1895–1906, 1990.

[17] K. Ueno, M. Kasuya, M. Watanabe, M. Mizukami, and K. Kurihara, "Resonance shear measurement of nanoconfined ionic liquids," *Physical Chemistry Chemical Physics*, vol. 12, pp. 4066–4071, 2010.

[18] S. Perkin, T. Albrecht, and J. Klein, "Layering and shear properties of an ionic liquid 1-ethyl-3-methylimidazolium ethylsulfate confined to nano-films between mica surfaces," *Physical Chemistry Chemical Physics*, vol. 12, pp. 1243–1247, 2010.

[19] S. Perkin, "Ionic liquids in confined geometries," *Physical Chemistry Chemical Physics*, vol. 14, pp. 5052–5062, 2012.

[20] P. Wasserscheid and T. Welton, *Ionic Liquids in Synthesis*. Wiley-VCH Verlag GmbH, 2002.

[21] J. D. Holbrey, W. M. Reichert, M. Nieuwenhuyzen, S. Johnson, K. R. Seddon, and R. D. Rogers, "Crystal polymorphism in 1-butyl-3-methylimidazolium halides: Supporting ionic liquid formation by inhibition of crystallization," *Chemical Communications*, pp. 1636–1637, 2003.

[22] M. J. Earle and K. R. Seddon, "Ionic liquids. Green solvents for the future," *Pure and Applied Chemistry*, vol. 72, no. 7, pp. 1391–1398, 2000.

[23] J. N. C. Lopes and A. H. Padua, "Nanostructural Organization in Ionic Liquids," *Journal of Physical Chemistry B*, vol. 110, no. 7, pp. 3330–3335, 2006.

[24] J. N. C. Lopes, M. F. C. Gomes, and A. H. Padua, "Nonpolar, Polar, and Associating Solutes in Ionic Liquids," *Journal of Physical Chemistry B*, vol. 110, no. 34, pp. 16816–16818, 2006.

[25] N. V. Plechkova and K. R. Seddon, "Applications of Ionic Liquids in the Chemical Industry," *Chemical Society Reviews*, vol. 37, no. 1, pp. 123–150, 2008.

[26] M. Armand, F. Endres, D. R. MacFarlane, H. Ohno, and B. Scrosati, "Ionic-liquid materials for the electrochemical challenges of the future," *Nature Materials*, vol. 8, no. 8, pp. 621–629, 2009.

[27] T. L. Greaves and C. J. Drummond, "Protic Ionic Liquids: Properties and Applications," *Chemical Reviews*, vol. 108, no. 1, pp. 206–237, 2008.

[28] N. Byrne, P. Howlett, D. MacFarlane, and M. Forsyth, "The zwitterion effect in ionic liquids: Towards practical rechargeable lithium-metal batteries," *Advanced Materials*, vol. 17, no. 20, pp. 2497–2501, 2005.

[29] R. Fortunato, C. A. M. Afonso, M. A. M. Reis, and J. G. Crespo, "Supported liquid membranes using ionic liquids: Study of stability and transport mechanisms," *Journal of Membrane Science*, vol. 242, no. 1–2, pp. 197 – 209, 2004.

[30] I. Minami, "Ionic Liquids in Tribology," *Molecules*, vol. 14, no. 6, pp. 2286–2305, 2009.

[31] F. Zhou, Y. Liang, and W. Liu, "Ionic Liquid Lubricants: Designed Chemistry for Engineering Applications," *Chemical Society Reviews*, vol. 38, no. 9, pp. 2590–2599, 2009.

[32] M. Palacio and B. Bhushan, "A Review of Ionic Liquids for Green Molecular Lubrication in Nanotechnology," *Tribology Letters*, vol. 40, no. 2, pp. 247–268, 2010.

[33] A. S. Pensado, M. J. P. Comunas, and J. Fernandez, "The pressure-viscosity coefficient of several ionic liquids," *Tribology Letters*, vol. 31, no. 2, pp. 107–118, 2008.

[34] H. Kamimura, T. Kubo, I. Minami, and S. Mori, "Effect and Mechanism of Additives for Ionic Liquids as New Lubricants," *Tribology International*, vol. 40, no. 4, pp. 620–625, 2007.

[35] A. E. Jimenez, M. D. Bermudez, F. J. Carrion, and G. Martinez-Nicolas, "Room Temperature Ionic Liquids as Lubricant Additives in Steel-Aluminium Contacts: Influence of Sliding Velocity, Normal Load and Temperature," *Wear*, vol. 261, no. 3-4, pp. 347–359, 2006.

[36] Z. Mu, W. Liu, and S. Zhang, "Functional Room-Temperature Ionic Liquids as Lubricants for an Aluminum-on-Steel System," *Chemistry Letters*, vol. 33, no. 5, pp. 524–525, 2004.

[37] Z. Mu, F. Zhou, S. Zhang, Y. Liang, and W. Liu, "Effect of the functional groups in ionic liquid molecules on the friction and wear behavior of aluminum alloy in lubricated aluminum-on-steel contact," *Tribology International*, vol. 38, no. 8, pp. 725 – 731, 2005.

[38] M. Cai, Y. Liang, M. Yao, Y. Xia, F. Zhou, and W. Liu, "Imidazolium Ionic Liquids as Antiwear and Antioxidant Additive in Poly(Ethylene Glycol) for Steel/Steel Contacts," *ACS Applied Materials and Interfaces*, vol. 2, no. 3, pp. 870–876, 2010.

[39] Cai, Meirong and Liang, Yongmin and Zhou, Feng and Liu, Weimin, "Tribological Properties of Novel Imidazolium Ionic Liquids Bearing Benzotriazole Group as the Antiwear/Anticorrosion Additive in Poly(ethylene glycol) and Polyurea Grease for Steel/Steel Contacts," *ACS Applied Materials and Interfaces*, vol. 3, no. 12, pp. 4580–4592, 2011.

[40] Cai, Meirong and Zhao, Zhu and Liang, Yongmin and Zhou, Feng and Liu, Weimin, "Alkyl Imidazolium Ionic Liquids as Friction Reduction and Anti-Wear Additive in Polyurea Grease for Steel/Steel Contacts," *Tribology Letters*, vol. 40, no. 2, pp. 215–224, 2010.

[41] H. Kamimura, T. Chiba, T. Kubo, H. Nanao, I. Minami, and S. Mori, "Relationship between Structure and Tribological Properties of Ionic Liquids Composed of Imidazolium Cations," *Journal of Japanese Society of Tribologists*, vol. 51, no. 11, pp. 826–834, 2006.

[42] Q. Lu, H. Wang, C. Ye, W. Liu, and Q. Xue, "Room temperature ionic liquid 1-ethyl-3-hexylimidazolium-bis(trifluoromethylsulfonyl)-imide as lubricant for steel–steel contact," *Tribology International*, vol. 37, no. 7, pp. 547 – 552, 2004.

[43] J. Qu, J. J. Truhan, S. Dai, H. Luo, and P. J. Blau, "Ionic Liquids with Ammonium Cations as Lubricants or Additives," *Tribology Letters*, vol. 22, no. 3, pp. 207–214, 2006.

[44] S. Stolte, S. Steudte, A. Igartua, and P. Stepnowski, "The Biodegradation of Ionic Liquids - the View from a Chemical Structure Perspective," *Current Organic Chemistry*, vol. 15, no. 12, pp. 1946–1973, 2011.

[45] S. Stolte, S. Steudte, O. Areitioaurtena, F. Pagano, J. Thöming, P. Stepnowski, and A. Igartua, "Ionic liquids as lubricants or lubrication additives: an ecotoxicity and biodegradability assessment," *Chemosphere*, vol. 89, no. 9, pp. 1135–1141, 2012.

[46] L. Pisarova, C. Gabler, N. Dörr, E. Pittenauer, and G. Allmaier, "Thermo-oxidative stability and corrosion properties of ammonium based ionic liquids," *Tribology International*, vol. 46, no. 1, pp. 73 – 83, 2012.

[47] Kronberger, Markus and Pejaković, Vladimir and Gabler, C. and Kalin, Mitjan, "How anion and cation species influence the tribology of a green lubricant based on ionic liquids," *Proceedings of the Institution of Mechanical Engineers, Part J: Journal of Engineering Tribology*, vol. 226, pp. 933–951, 2012.

[48] B. A. J. and F. L. R., *Electrochemical Methods*. New York: John Wiley and Sons, 2nd edn ed., 2001.

[49] M.-M. Huang, Y. Jiang, P. Sasisanker, G. W. Driver, and H. Weingärtner, "Static relative dielectric permittivities of ionic liquids at 25 °c," *Journal of Chemical & Engineering Data*, vol. 56, no. 4, pp. 1494–1499, 2011.

[50] C. Aliaga and S. Baldelli, "Sum frequency generation spectroscopy and double-layer capacitance studies of the 1-butyl-3-methylimidazolium dicyanamide,àíplatinum interface," *The Journal of Physical Chemistry B*, vol. 110, no. 37, pp. 18481–18491, 2006.

[51] C. Aliaga, C. S. Santos, and S. Baldelli, "Surface chemistry of room-temperature ionic liquids," *Physical Chemistry Chemical Physics*, vol. 9, pp. 3683–3700, 2007.

[52] S. Baldelli, "Surface structure at the ionic liquid,àíelectrified metal interface," *Accounts of Chemical Research*, vol. 41, no. 3, pp. 421–431, 2008.

[53] R. Atkin, S. Z. E. Abedin, R. Hayes, L. H. S. Gasparotto, N. Borisenko, and F. Endres, "Afm and stm studies on the surface interaction of [bmp]tfsa and [emim]tfsa ionic liquids with au(111)," *The Journal of Physical Chemistry C*, vol. 113, no. 30, pp. 13266–13272, 2009.

[54] R. Hayes, N. Borisenko, M. K. Tam, P. C. Howlett, F. Endres, and R. Atkin, "Double layer structure of ionic liquids at the au(111) electrode interface: An atomic force microscopy investigation," *The Journal of Physical Chemistry C*, vol. 115, no. 14, pp. 6855–6863, 2011.

[55] S. Tazi, M. Salanne, C. Simon, P. Tury, M. Pounds, and P. A. Madden, "Potential-Induced Ordering Transition of the Adsorbed Layer at the Ionic Liquid/Electrified Metal Interface," *Journal of Physical Chemistry B*, vol. 114, no. 25, pp. 8453–8459, 2010.

[56] A. S. Pensado and A. H. Padua, "Solvation and stabilization of metallic nanoparticles in ionic liquids," *Angewandte Chemie International Edition*, vol. 50, no. 37, pp. 8683–8687, 2011.

[57] M. V. Fedorov and R. M. Lynden-Bell, "Probing the neutral graphene-ionic liquid interface: Insights from molecular dynamics simulations," *Physical Chemistry Chemical Physics*, vol. 14, pp. 2552–2556, 2012.

[58] M. V. Fedorov, N. Georgi, and A. A. Kornyshev, "Double Layer in Ionic Liquids: the Nature of the Camel Shape of Capacitance," *Electrochemistry Communications*, vol. 12, no. 2, pp. 296–299, 2010.

[59] J. A. Harrison, S. J. Stuart, and D. W. Brenner, *Handbook of Micro/Nanotribology*, ch. Atomic-scale simulation of tribological and related phenomena, pp. 525–594. Boca Raton: CRC Press, 1999.

[60] G. He and M. O. Robbins, "Simulations of the kinetic friction due to adsorbed surface layers," *Tribology Letters*, vol. 10, pp. 7–14, 2001.

[61] G. He and M. O. Robbins, "Simulations of the Static Friction due to Adsorbed Molecules," *Physical Review B*, vol. 64, no. 3, 2001.

[62] M. R. Farrow, A. Chremos, P. J. Camp, S. G. Harris, and R. F. Watts, "Molecular Simulations of Kinetic-Friction Modification in Nanoscale Fluid Layers," *Tribology Letters*, vol. 42, no. 3, pp. 325–337, 2011.

[63] M. Chandross, C. D. Lorenz, M. J. Stevens, and G. S. Grest, "Simulations of nanotribology with realistic probe tip models," *Langmuir*, vol. 24, no. 4, pp. 1240–1246, 2008.

[64] I. Szlufarska, M. Chandross, and R. W. Carpick, "Recent Advances in Single-Asperity Nanotribology," *Journal of Physics D-Applied Physics*, vol. 41, no. 12, 2008.

[65] S. Eder, A. Vernes, G. Vorlaufer, and G. Betz, "Molecular dynamics simulations of mixed lubrication with smooth particle post-processing," *Journal of Physics: Condensed Matter*, vol. 23, no. 17, p. 175004, 2011.

[66] A. Vernes, S. Eder, G. Vorlaufer, and G. Betz, "On the three-term kinetic friction law in nanotribological systems," *Faraday Discussions*, vol. 156, pp. 173–196, 2012.

[67] S. G. Raju and S. Balasubramanian, "Intermolecular correlations in an ionic liquid under shear," *Journal of Physics: Condensed Matter*, vol. 21, no. 3, 2009.

[68] O. A. Mazyar, G. K. Jennings, and C. McCabe, "Frictional dynamics of alkylsilane monolayers on sio2: Effect of 1-n-butyl-3-methylimidazolium nitrate as a lubricant," *Langmuir*, vol. 25, no. 9, pp. 5103–5110, 2009.

[69] Allen, M. P. and Tildesley, D. J., *Computer Simulation of Liquids*. Oxford: Clarendon Press, 1989.

[70] L. de Broglie, "Recherches sur la théorie des quanta," *Annales de Physique*, vol. 10, no. 3, 1925.

[71] W. L. Jorgensen, D. S. Maxwell, and J. Tirado-Rives, "Development and testing of the opls all-atom force field on conformational energetics and properties of organic liquids," *Journal of the American Chemical Society*, vol. 118, no. 45, pp. 11225–11236, 1996.

[72] G. Kaminski and W. L. Jorgensen, "Performance of the amber94, mmff94, and opls-aa force fields for modeling organic liquids," *The Journal of Physical Chemistry*, vol. 100, no. 46, pp. 18010–18013, 1996.

[73] J. N. C. Lopes and A. H. Padua, "Molecular Force Field for Ionic Liquids Composed of Triflate or Bistriflylimide Anions," *Journal of Physical Chemistry B*, vol. 108, no. 43, pp. 16893–16898, 2004.

[74] J. N. C. Lopes, J. Deschamps, and A. H. Padua, "Modeling ionic liquids using a systematic all-atom force field," *The Journal of Physical Chemistry B*, vol. 108, no. 6, pp. 2038–2047, 2004.

[75] W. L. Jorgensen, D. S. Maxwell, and J. Tirado-Rives, "Development and testing of the opls all-atom force field on conformational energetics and properties of organic liquids," *Journal of the American Chemical Society*, vol. 118, no. 45, pp. 11225–11236, 1996.

[76] R. C. Rizzo and W. L. Jorgensen, "Opls all-atom model for amines," *Journal of the American Chemical Society*, vol. 121, no. 20, pp. 4827–4836, 1999.

[77] J. N. C. Lopes, A. A. H. Padua, and K. Shimizu, "Molecular Force Field for Ionic Liquids IV: Trialkylimidazolium and Alkoxycarbonyl-Imidazolium Cations; Alkylsulfonate and Alkylsulfate Anions," *Journal of Physical Chemistry B*, vol. 112, no. 16, pp. 5039–5046, 2008.

[78] Smith, W. and Forester, T. R., *DL_POLY* 2.20 *ed.* Daresbury Laboratory, UK, 2007.

[79] J. Qian, R. Hentschke, and A. Heuer, "Dynamic Heterogeneities of Translational and Rotational Motion of a Molecular Glass Former from Computer Simulations," *Journal Of Chemical Physics*, vol. 110, no. 9, pp. 4514–4522, 1999.

[80] M. Mahrova, M. Vilas, Á. Domínguez, E. Gómez, N. Calvar, and E. Tojo, "Physicochemical characterization of new sulfonate and sulfate ammonium ionic liquids," *Journal of Chemical and Engineering Data*, vol. 57, no. 2, pp. 241–248, 2012.

[81] B. González, E. Gómez, Á. Domínguez, M. Vilas, and E. Tojo, "Physicochemical characterization of new sulfate ionic liquids," *Journal of Chemical and Engineering Data*, vol. 56, no. 1, pp. 14–20, 2011.

[82] A. H. Padua, M. F. C. Gomes, and J. N. C. Lopes, "Molecular solutes in ionic liquids: A structural perspective," *Accounts of Chemical Research*, vol. 40, no. 11, pp. 1087–1096, 2007.

[83] K. Shimizu, A. H. Padua, and J. N. C. Lopes, "Nanostructure of trialkylmethylammonium bistriflamide ionic liquids studied by molecular dynamics," *The Journal of Physical Chemistry B*, vol. 114, no. 47, pp. 15635–15641, 2010.

[84] C. Cadena, Q. Zhao, R. Q. Snurr, and E. J. Maginn, "Molecular modeling and experimental studies of the thermodynamic and transport properties of pyridinium-based ionic liquids," *The Journal of Physical Chemistry B*, vol. 110, no. 6, pp. 2821–2832, 2006.

[85] S. Tsuzuki, W. Shinoda, H. Saito, M. Mikami, H. Tokuda, and M. Watanabe, "Molecular dynamics simulations of ionic liquids: Cation and anion dependence of self-diffusion coefficients of ions," *The Journal of Physical Chemistry B*, vol. 113, no. 31, pp. 10641–10649, 2009.

[86] H. Liu, E. Maginn, A. E. Visser, N. J. Bridges, and E. B. Fox, "Thermal and transport properties of six ionic liquids: An experimental and molecular dynamics study," *Industrial & Engineering Chemistry Research*, vol. 51, no. 21, pp. 7242–7254, 2012.

[87] H. Tokuda, S. Tsuzuki, M. A. B. H. Susan, K. Hayamizu, and M. Watanabe, "How ionic are room-temperature ionic liquids? an indicator of the physicochemical properties," *The Journal of Physical Chemistry B*, vol. 110, no. 39, pp. 19593–19600, 2006.

[88] H. Tokuda, K. Ishii, M. A. B. H. Susan, S. Tsuzuki, K. Hayamizu, and M. Watanabe, "Physicochemical properties and structures of room-temperature ionic liquids. 3. variation of cationic structures," *The Journal of Physical Chemistry B*, vol. 110, no. 6, pp. 2833–2839, 2006.

[89] M. S. Kelkar and E. J. Maginn, "Effect of temperature and water content on the shear viscosity of the ionic liquid 1-ethyl-3-methylimidazolium bis(trifluoromethanesulfonyl)imide as studied by atomistic simulations," *The Journal of Physical Chemistry B*, vol. 111, no. 18, pp. 4867–4876, 2007. PMID: 17408255.

[90] F. Dommert, K. Wendler, R. Berger, L. Delle Site, and C. Holm, "Force fields for studying the structure and dynamics of ionic liquids: a critical review of recent developments," *ChemPhysChem*, vol. 13, no. 7, pp. 1625–1637, 2012.

[91] A. Sirjoosingh, S. Alavi, and T. K. Woo, "Molecular dynamics simulations of equilibrium and transport properties of amino acid-based room temperature ionic liquids," *The Journal of Physical Chemistry B*, vol. 113, no. 23, pp. 8103–8113, 2009.

[92] M. W. Finnis and J. E. Sinclair, "A simple empirical n-body potential for transition metals," *Philosophical Magazine A*, vol. 50, no. 1, pp. 45–55, 1984.

[93] Y. Watanabe, Y. Shibuta, and T. Suzuki, "A Molecular Dynamics Study of Thermodynamic and Kinetic Properties of Solid-Liquid Interface for Bcc Iron," *ISIJ International*, vol. 50, no. 8, pp. 1158–1164, 2010.

[94] Y. Shim and H. J. Kim, "Solvation of Carbon Nanotubes in a Room-Temperature Ionic Liquid," *ACS Nano*, vol. 3, no. 7, pp. 1693–1702, 2009.

[95] Y. Shim, Y. Jung, and H. J. Kim, "Graphene-Based Supercapacitors: A Computer Simulation Study," *Journal of Physical Chemistry C*, vol. 115, no. 47, pp. 23574–23583, 2011.

[96] M. Salanne and P. A. Madden, "Polarization Effects in Ionic Solids and Melts," *Molecular Physics*, vol. 109, no. 19, pp. 2299–2315, 2011.

[97] J. Vatamanu, O. Borodin, and G. D. Smith, "Molecular insights into the potential and temperature dependences of the differential capacitance of a room-temperature ionic liquid at graphite electrodes," *Journal of the American Chemical Society*, vol. 132, no. 42, pp. 14825–14833, 2010.

[98] J. Vatamanu, O. Borodin, and G. D. Smith, "Molecular simulations of the electric double layer structure, differential capacitance, and charging kinetics for n-methyl-n-propylpyrrolidinium bis(fluorosulfonyl)imide at graphite electrodes," *The Journal of Physical Chemistry B*, vol. 115, no. 12, pp. 3073–3084, 2011.

[99] C. Merlet, B. Rotenberg, P. A. Madden, P.-L. Taberna, P. Simon, Y. Gogotsi, and M. Salanne, "On the Molecular Origin of Supercapacitance in Nanoporous Carbon Electrodes," *Nature Materials*, vol. 11, no. 4, pp. 306–310, 2012.

[100] Y. Zhao and D. G. Truhlar, "A New Local Density Functional for Main-Group Thermochemistry, Transition Metal Bonding, Thermochemical Kinetics, and Noncovalent Interactions," *Journal of Chemical Physics*, vol. 125, no. 19, 2006.

[101] A. Schafer, C. Huber, and R. Ahlrichs, "Fully Optimized Contracted Gaussian-Basis Sets Of Triple Zeta Valence Quality For Atoms Li To Kr," *Journal of Chemical Physics*, vol. 100, no. 8, pp. 5829–5835, 1994.

[102] M. Dolg, U. Wedig, H. Stoll, and H. Preuss, "abinitio Pseudopotential Study of the 1st Row Transition-Metal Monoxides and Iron Monohydride," *Journal of Chemical Physics*, vol. 86, no. 4, pp. 2123–2131, 1987.

[103] Walker, P. D. And Mezey, P.G., "Molecular Electron-Density Lego Approach To Molecule Building," *Journal of the American Chemical Society*, vol. 115, no. 26, pp. 12423–12430, 1993.

[104] M. J. Frisch and G. W. Trucks and H. B. Schlegel and G. E. Scuseria and M. A. Robb and J. R. Cheeseman and G. Scalmani and V. Barone and B. Mennucci and G. A. Petersson and H. Nakatsuji and M. Caricato and X. Li and H. P. Hratchian and A. F. Izmaylov and J. Bloino and G. Zheng and J. L. Sonnenberg and M. Hada and M. Ehara and K. Toyota and R. Fukuda and J. Hasegawa and M. Ishida and T. Nakajima and Y. Honda and O. Kitao and H. Nakai and T. Vreven and Montgomery, Jr., J. A. and J. E. Peralta and F. Ogliaro and M. Bearpark and J. J. Heyd and E. Brothers and K. N. Kudin and V. N. Staroverov and R. Kobayashi and J. Normand and K. Raghavachari and A. Rendell and J. C. Burant and S. S. Iyengar and J. Tomasi and M. Cossi and N. Rega and J. M. Millam and M. Klene and J. E. Knox and J. B. Cross and V. Bakken and C. Adamo and J. Jaramillo and R. Gomperts and R. E. Stratmann and O. Yazyev and A. J. Austin and R. Cammi and C. Pomelli and J. W. Ochterski and R. L. Martin and K. Morokuma and V. G. Zakrzewski and G. A. Voth and P. Salvador and J. J. Dannenberg and S. Dapprich and A. D. Daniels and Ö. Farkas and J. B. Foresman and J. V. Ortiz and J. Cioslowski and D. J. Fox, *Gaussian 03 Revision A.1*. Gaussian Inc. Wallingford CT 2009.

[105] S. H. Vosko, L. Wilk, and M. Nusair, "Accurate Spin-Dependent Electron Liquid Correlation Energies For Local Spin-Density Calculations - A Critical Analysis," *Canadian Journal of Physics*, vol. 58, no. 8, pp. 1200–1211, 1980.

[106] Hay, P. J. and Wadt, W. R., "abinitio Effective Core Potentials for Molecular Calculations - Potentials for K to Au Including the Outermost Core Orbitals," *Journal Of Chemical Physics*, vol. 82, no. 1, pp. 299–310, 1985.

[107] Hay, P. J. And Wadt, W. R., "abinitio Effective Core Potentials for Molecular Calculations - Potentials for the Transition-Metal Atoms Sc to Hg," *Journal Of Chemical Physics*, vol. 82, no. 1, pp. 270–283, 1985.

[108] C. Kohler, G. Seifert, and T. Frauenheim, "Density Functional based Calculations for Fe-n (n <= 32)," *Chemical Physics*, vol. 309, no. 1, SI, pp. 23–31, 2005.

[109] S. Boys and F. Bernardi, "The calculation of small molecular interactions by the differences of separate total energies. some procedures with reduced errors," *Molecular Physics*, vol. 19, no. 4, pp. 553–566, 1970.

[110] J. F. Weaver, A. F. Carlsson, and R. J. Madix, "The Adsorption and Reaction of Low Molecular Weight Alkanes on Metallic Single Crystal Surfaces," *Surface Science Reports*, vol. 50, no. 4-5, pp. 107–199, 2003.

[111] C. L. Kao and R. J. Madix, "The Adsorption Dynamics of Small Alkanes on (111) Surfaces of Platinum Group Metals," *Surface Science*, vol. 557, no. 1-3, pp. 215–230, 2004.

[112] K. Lee, Y. Morikawa, and D. C. Langreth, "Adsorption of n-butane on Cu(100), Cu(111), Au(111), and Pt(111): Van der Waals density-functional study," *Physical Review B*, vol. 82, no. 15, pp. 4853–4856, 2010.

[113] L. Wang, H. B. Wu., and S. R. Desai, "Sequential Oxygen Atom Chemisorption on Surfaces of Small Iron Clusters," *Physical Review Letters*, vol. 76, no. 25, pp. 4853–4856, 1996.

[114] J. H. R. Clarke, W. Smith, and L. V. Woodcock, "Short-Range Effective Potentials For Ionic Fluids," *Journal of Chemical Physics*, vol. 84, no. 4, pp. 2290–2294, 1986.

[115] F. Iori and S. Corni, "Including Image Charge Effects in the Molecular Dynamics Simulations of Molecules on Metal Surfaces," *Journal of Computational Chemistry*, vol. 29, no. 10, pp. 1656–1666, 2008.

[116] A. S. Pensado, P. Malfreyt, and A. H. Padua, "Molecular dynamics simulations of the liquid surface of the ionic liquid 1-hexyl-3-methylimidazolium bis(trifluoromethanesulfonyl)amide: Structure and surface tension," *The Journal of Physical Chemistry B*, vol. 113, no. 44, pp. 14708–14718, 2009.

[117] O. Braun, "Bridging the gap between the atomic-scale and macroscopic modeling of friction," *Tribology Letters*, vol. 39, pp. 283–293, 2010.

[118] S. Plimpton, "Fast parallel algorithms for short-range molecular dynamics," *Journal of Computational Physics*, vol. 117, pp. 1–19, 1995.

[119] R. Hockney and J. W. Eastwood, *Computer Simulation Using Particles*. New York: Taylor & Francis, 1989.

[120] J. Irving and J. Kirkwood, "The Statistical Mechanical Theory of Transport Processes. IV. The Equations of Hydrodynamics," *Journal of Chemical Physics*, vol. 18, no. 6, pp. 817–829, 1950.

[121] J. Walton, D. J. Tildesley, J. Rowlinson, and J. Henderson, "The Pressure Tensor At The Planar Surface Of A Liquid," *Molecular Physics*, vol. 48, no. 6, pp. 1357–1368, 1983.

[122] Pejaković, Vladimir and Kronberger, Markus and Kalin, Mitjan and Mahrova, Maria and Vilas, Miguel and Tojo, E, "Pyrrolidinium Sulfate and Ammonium Sulfate Ionic Liquid as Green Lubricant Additives for Steel/Steel Contact Lubrication," *Proceedings of the Institution of Mechanical Engineers, Part J: Journal of Engineering Tribology*, vol. 226, pp. 923–932, 2012.

[123] K. Falk, F. Sedlmeier, L. Joly, R. R. Netz, and L. Bocquet, "Molecular origin of fast water transport in carbon nanotube membranes: Superlubricity versus curvature dependent friction," *Nano Letters*, vol. 10, no. 10, pp. 4067–4073, 2010.

[124] G. Peters and D. Tildesley, "Computer Simulation of the Rheology of Grafted Chains under Shear .2. Depletion of Chains at the Wall," *Physical Review E*, vol. 54, no. 5, pp. 5493–5501, 1996.

[125] F. Goujon, P. Malfreyt, and D. J. Tildesley, "Mesoscopic Simulation of Entangled Polymer Brushes under Shear: Compression and Rheological Properties," *Macromolecules*, vol. 42, no. 12, pp. 4310–4318, 2009.

[126] G. C. Boulougouris, I. G. Economou, and D. N. Theodorou, "Engineering a molecular model for water phase equilibrium over a wide temperature range," *The Journal of Physical Chemistry B*, vol. 102, no. 6, pp. 1029–1035, 1998.

[127] A. C. F. Mendonca, P. Malfreyt, and A. H. Padua, "Interactions and Ordering of Ionic Liquids at a Metal Surface," *Journal of Chemical Theory and Computation*, vol. 8, no. 9, pp. 3348–3355, 2012.

[128] A. C. F. Mendonca, P. Malfreyt, and A. H. Padua, "Non-Equilibrium Molecular Simulations of New Ionic Lubricants at Metallic Surfaces: Prediction of the Friction," *accepted for publication*, 2013.